Thesis for the degree of Doctor of
Philosophy
in the Natural Sciences

Structural studies of ba_3-type cytochrome *c* oxidase using serial crystallography and X-ray absorption spectroscopy

---

Doris Zorić

UNIVERSITY OF GOTHENBURG

Department of Chemistry and Molecular Biology
Gothenburg, 2023

Thesis for the degree of Doctor of Philosophy
in the Natural Sciences

Structural studies of *ba*$_3$-type cytochrome *c* oxidase using serial crystallography and X-ray absorption spectroscopy

Doris Zorić

Cover: *ba*$_3$-type cytochrome *c* oxidase and its co-factors

ISBN 978-91-8069-395-0 (Print)
ISBN 978-91-8069-396-7 (PDF)
Available online at http://hdl.handle.net/2077/77578

Department of Chemistry and Molecular Biology
Division of Biochemistry and Structural Biology
University of Gothenburg
SE-405 30, Göteborg, Sweden
Printed by Stema Specialtryck AB
Borås, Sweden, 2023

SVANENMÄRKET
Trycksak
3041 0234

Abstract

Cytochrome *c* oxidase (C*c*O) catalyses the reduction of molecular oxygen to water while the energy released in this process is used transport protons "up-hill" across an energy transducing biological membrane, creating a proton-motive force for ATP synthesis. Given its key role in energy transduction in organisms, proton pumping has been extensively studied across species. Even though many members of the C*c*O superfamily have been structurally characterized in detail, time-resolved structural details of electron transfer coupled to proton pumping have not been entirely understood. A billion-fold jump in the peak X-ray brilliance delivered by X-ray free electron laser (XFEL) and the development of serial femtosecond crystallography (SFX) allowed the determination of protein structures at room temperature, opening up the opportunities to measure ultrafast reactions in proteins. Moving beyond the study of only light-sensitive systems, our long-term goal is to use time-resolved serial femtosecond crystallography at XFELs for a comprehensive structural study of cytochrome *c* oxidase activity. First, we employed a standard pump-probe SFX setup in a time-resolved (TR) study of structural events following the photodissociation of carbon monooxide (CO) from a reduced CO-bound ba_3-type C*c*O. In the following study, we performed TR-SFX to track structural changes at the active site of ba_3-type C*c*O upon photoinitiated release of oxygen molecule from cobal-based cage compound. Moreover, to utilize the potential of synchrotron radiation and lower the entry barrier for serial crystallography at synchrotron beamlines, we designed and experimentally validated a flow-cell device for serial synchrotron crystallography (SSX) at room-temperature. Finally, we used X-ray absorption spectroscopy (XAS) to access electronic configuration and coordination geometry of copper and iron co-factors of ba_3-type C*c*O in different redox states. Qualitative analysis of X-ray absorption near-edge structure (XANES) and theory-based model of extended X-ray absorption fine structure (EXAFS) highlighted differences between

analyzed samples, leaving room for additional computational input to obtain a detailed fingerprint of *ba*$_3$-type C*c*O redox states and better understanding of possible ligands in the heme *a*$_3$-Cu$_B$ active site. The work presented in this thesis highlights the importance of utilizing different methods for comprehensive understanding of enzyme reaction dynamics.

Acknowledgements

Gisela, thank you for taking a chance on me, and guiding me in this process. You have been such a warrior in these last days, giving it all in the finish line. You are a role model in the way how you just balance all of your activities, always finding time to deliver spotless results. Most importantly, thank you for keeping me calm and re-assured everything is going well, in the times I needed it the most. **Richard**, thank you for all of the inspiration and support throughout the years. The list of interests we share is long, but what is truly remarkable is our love for music. You believed in me, and were confident that one day I will be proud of what is achieved. Well, that day has come! I hope we get to do more of great research together, and that I always find a friend in you. **Gergely**, thanks for your valuable input during our ISP meetings, it was a pleasure to have you as an examiner.

Jonatan, thank you for working by my side, and balancing me well, even though I know it wasn't always easy. One of the most talented people I met, and one who always finds a way to deliver for the people who rely on him. Thank you for all the beamtime travels, all the sports activities, coffee breaks, beer after-works, and much more. And thanks for teaching me how to ice skate! **Arpitha**, you are very brave in taking up new tasks, and you master them in no time. I will always remember the concert of your orchestra, where you did so great. Thank you for all the hard work you put in for the experiments. You will keep on doing great things. **Adams**, I am eternally thankful for you bailing on the suspicious "tree-hugging" activities proposed by others, and hitting the Stanford campus with me during our last day in sunny California. On a more serious note: thank you for your ultimate dedication with computational work, nothing would have been possible without your help. **Emil**, you are the ultimate whiskey enthusiast, a great organic chemist, a talented

brewer, a fierce bureaucracy warrior, but most importantly – the co-inventor of the Beamtime Bingo and the best biceps of the Team Oxidase! **Swagatha**, you taught me a lot about crystallography, and even more about how to deal with some things in life. And, you made me cocktails on a Christmas eve! Wherever your brave spirit takes you, I am confident you will shine, and make a lot of friends.

Monika, the destiny has put us in different locations, and yet we built that bridge. I don't think a week has ever passed without talking to you, or that I could imagine pushing through all of this without you being somewhat of a lab soulmate. Thank you for all the times I slept on your couch in Malmö, and all the foodie experiences we shared. **Noor**, habibi, no one can match the hospitality you and your family provided in your beautiful home, and support in helping me move to my new home. I hope that we soon re-install our long fikas. **Analia** (aka "Shakira"), you bring out the Latina in me, and I love how we shared the passion for music, dancing, and nice food. **Lidija**, the stories that write themselves every time we meet up for a beer sound unbelievable to many people who get to hear about our quests. Your big heart, open to every human, simply attracts people to speak to you, and I never knew who I would end up meeting or where the adventure would take us. I miss all of it. P.S. Our VIP table by the window in Magazzino will always be ready for us. **Szabolcs**, I hope you will make some other office mates very happy. I miss our office pranks, lunch breaks, and consuming a lot of sugar. Hope to do more slacklining in the park some day! Heads up: I still do plan on maintaining our historical beef. **Božidar**, you made my Swedish midsommar a little bit more Balkan. Thank you for being such a good friend, who I shared many memories (and Instagram reels!) with in such a short time. Oh, and you make the best Turkish coffee! **Dimitra**, "the gas lady", you have this unique ability to bright up my day with your smile. I enjoyed our carefully planned lunch breaks. I can't wait to see you crowned with a Dr. title!

To the Brändéliers: **Owens**, we started at the same time, been through same BS, laughed it through, and now we are at the same finish line. Let's bring it home! **Andreas**, I guess whatever I write would not convince you to drop the zucchini farming as a legitimate plan B. So I just wish that plan A (crystallography) pays out in the end. **Gabrielle**, I hope our paths cross at some acoustic concert. I wish I get to hear more about all of your cool interests sometime soon. **Johan**, you have been a great asset to the group. Take care of Brändéliers, and the centrifuges, of course!

Lucija, since I laughed with you the most, to the point of stomach cramps, there is only one thing left to ask: ko brani za rižoto? **Andrea**, we agree that Swedish summer sucks big time. I hope the future has warmer summers installed for Dr. Cellini! **Giorgia**, you give your heart to everything you do, and I hope you get to follow your heart for more beautiful opportunities. **Per** and **Greger**, you have really contributed to the great experience of my first beamtime in Japan. **Laras** – by far the best dark humor and the most skilled piano enthusiast one can find in those hallways on 2nd floor. **Leona**, drink one in Folket for me! **Daniel**, we miss you over here, but I have to admit that letter briefcase suits you. Keep on charming them! **Damasus**, I think I lost the photo of you in the suit from that day I said you look like a football manager. **Jens** and **Ylber**, no one brings their A game in suiting up for defence dinners like you do! Two classiest gentlemen, by far. **Hannah**, you are doing great putting up with these two, and you are killing it as a toast master! Also, seeing you play football blew my mind. **Fillipo**, thank you for being such a friendly presence in the lab. **Irena** and **Björn**, I will always cherish that Christmas day in the winter of 2020. The warmth of your home and a family atmosphere made it easier to be separated from home. **Emelie**, you have always had some kind words stored in for me. Thank you for that. **Charles**, thank you for always being the one up for a beer, or a hangout in the nature. I hope for more of spontaneous afterworks. **Taru**, easily the most stylish addition to the Lundberg lab. I hope Uppsala will treat you well. **Jessica**, I still want to do that run together, and fika too! **Florian**, I just love that refreshing entrepreneurial spirit, and I am so curios to see where it will take you. **Kristina**, I enjoyed hearing about your love for rock music, that makes two of us! **Julia**, your drive is truly remarkable, and refreshing. I am excited to see all the success that future brings for you. **Ulrika**, I think of you whenever I listen to Swedish pop. **Majo**, I am so glad you had time to meet me for an open-door salsa last summer. **Amke**, your outdoor activities are a huge inspiration. **Ann**, thank you for all resolving all of my confusions when teaching fell in my lap. **Lars** and **Bruno**, thank you for all the assistance I received over the years. **Peter**, you are an outstanding engineer, and a great addition to every beamtime trip! **Magnus**, thank you for insightful talks during the LEAPS conference last May, and I hope that your group keeps on growing and delivering great research.

To **everyone** in Lundberg lab, it was a pleasure meeting you, and thank you for all of your help.

To MAX IV girls a.k.a."The Bridesmaids": **Kajsa**, I will always be proud of what we have achieved together, after so much trial and error, often confusion, but as well those "Heureka!" moments that always resulted in a whiteboard covered in scribbles. Thank you for being such a wonderful collaborator, who I learned so much from. **Susan**, my night owl, who sat in front of those bright screens alone during night-shifts: I am so glad we found time for that fish & chips during my last visit in Lund. **Yang**, you are my favorite gossip girl, and a great conference companion. Thank you for all the support and fun hours at Balder. Three of you really made my XAS experiments memorable.

To the "fight club": I could have never dreamed of hanging an international gold as my office decoration. I thank everyone standing in my corner. You gave me the unique opportunity to see what I am able to achieve. Most importantly, nothing has ever given me more discipline, which has benefited me greatly in completing this piece of work.

To all my girls: **Veronica** and **Bojana**, there is no one I'd rather share a brunch with. You stood by my side in good and bad, for years now, and look at us now - almost Swedes! You helped in making this place feel like home. **Nina**, the one who always understood what it means to space out and work hard - she is a double World Champion, everyone! Your family became like my second family, and I can no longer imagine Swedish holidays without you. **Miray**, for all of your kindness despite all the rough moments you found yourself in – I thank you. **Conny**, I hope that now I will finally have some more time to return to our crazy training slots, and all the healthy snacks that come afterwards. **Irina**, no one brings out a dancing party girl in me like you do. **Natalia**, I hope that with your help, I get to run the half-marathon one day. **Wim**, you really showed me Gothenburg, and together we ruled this city on our Voi scooters. I can't wait to see you on the big screen taking part as an actor. **Riki**, can't wait for your next metal gig! **Berak** and **Patrik**, you are a great addition to my friend group. I hope to spend more Sunday hours at Havana with you.

To all of my friends back in Croatia, thank you for maintaining this long-distance relationship, and making my days with your messages or videos sent to me. **Krle, Tvrdi, Trenja, Čvugo, Juda, Rodica, Baja, Beta** – I could be spending every day with you, and still wanting to see you the next day. I hope we have a lifetime of fun summer and Christmas holidays ahead of us. **Lea**, you are the best roommate I ever had, and the one giving meaning to cold winter afternoons in Zagreb. **Iva**, ever since we were kids, we did everything together. You are like a sister to me, and everything I am, I owe to you as well.

To my family, who was prepared, since my early age, to be separated from me while I explore the wonders of the world and science, far away from home. Thank you for the sacrifices you made to put me through the education you thought I deserved. Thank you for never second-guessing any of my choices, especially when it felt like everything was against me. Together we made it, and we are stronger than ever. **Eugen**, you are my best friend in the world. Watching grow up and succeed, every day, in everything you set your mind on, has been inspiring.

And finally, I dedicate this to you, **Thorsten**, the best thing that happened in this challenging period. Your kindness, endless patience, and the best support, especially in the last few weeks, are what made this thesis happen. I am excited to take on new challenges and adventures with you by my side, as I truly found a partner in you.

This work received funding from the European Research Council (ERC) under the European Union's Horizon 2020 research and innovation programme (grant agreement No 789030).

Publications

This thesis consists of the following research papers:

PAPER I: C. Safari, S. Ghosh, R. Andersson, J. Johannesson, P. Båth, O. Uwangue, P. Dahl, D. Zorić, E. Sandelin, A. Vallejos, E. Nango, R. Tanaka, R. Bosman, P. Börjesson, E. Dunevall, G. Hammarin, G. Ortolani, M. Panman, T. Tanaka, A. Yamashita, T. Arima, M. Sugahara, M. Suzuki, T. Masuda, H. Takeda, R. Yamagiwa, K. Oda, M. Fukuda, T. Tosha, H. Naitow, S. Owada, K. Tono, O. Nureki, S. Iwata, R. Neutze and G. Brändén. "Time-resolved serial crystallography to track the dynamics of carbon monoxide in the active site of cytochrome *c* oxidase" *Manuscript; under second revision in Science Advances(2023)*

PAPER II: D. Zorić*, J. Johannesson*, A. Vallejos, E. Sandelin, A. Kabbinale, S. Ghosh, A. Flink, M. Bjelčić, J. Rönnholm, P. Dahl, E. V. Beale, C. Bostedt, C. Cirelli, C. Bacellar Cases da Silveira, P. Johnson, D. Ozerov, A. Batyuk, S. Boutet, C. Kupitz, A.Peck, F. Poitevin, R. Sierra, S. Lisova, C. J. Wallentin, G. Brändén and R. Neutze. "Structural changes in cytochrome *c* oxidase following the reduction of dioxygen to water" *Manuscript (2023)*
Authors labeled with "" contributed equally to this publication.*

PAPER III: S. Ghosh, D. Zorić, P. Dahl, M. Bjelčić, J. Johannesson, E. Sandelin, P. Borjesson, A. Björling, A. Banacore, P. Edlund, O. Aurelius, M. Milas, J. Nan, A. Shilova, A. Gonzalez, U. Mueller, G. Brändén and R. Neutze. "A simple goniometer-compatible flow cell for serial synchrotron X-ray crystallography" *J. Appl. Cryst. (2023). 56, 449–460 doi.org/10.1107/S1600576723001036*

PAPER IV: D. Zorić, S. Ghosh, M. Bjelčić, J. Johannesson, A. Kabbinale, E. Sandelin, Y. Chen, S. Nehzati, R. Neutze, K. Sigfridsson Clauss and G. Brändén. "X-ray absorption spectroscopy as a tool to investigate details of the cytochrome *c* oxidase metal co-factors" *Manuscript (2023)*

Contribution report

PAPER I: My contributions were credited with being listed as a co-author on the publication, and include: microbiological cell culture of *Thermus thermophilus*, protein purification, protein crystallization trials and screening of favorable conditions, help with production of microcystals in preparation for the TR-SFX experiment at SACLA (2019), beamtime support on sample preparation, as well as injector loading and transportation.

PAPER II: My contributions were credited with the shared first authorship, and include: microbiological cell culture of *T. thermophilus*, protein purification , protein crystallization trials and screening of favorable conditions, production of microcystals in preparation for SFX and TR-SFX at European XFEL, SwissFEL and LCLS in time period from May 2019 till May 2022, strategic planing of the experiments and execution of the experiments, mainly in charge of sample station, data processing and map refinement, and contributions to the writing of the manuscript.

PAPER III: My contributions were credited with the second authorship, and include: microbiological cell culture of *T. thermophilus*, protein purification, protein crystallization trials and screening of favorable conditions, production of microcystals in preparation for experiments at Biomax (MAX IV), flow device testing and optimization of carrier phase, experimental sample preparation and data collection, data processing and map refinement, figures for the manuscript, and contributions to the writing of the method section in the manuscript.

PAPER IV: My contributions to this publication were credited with first authorship, and include: microbiological cell culture of *T. thermophilus*, protein production and characterization in preparation for experiments at Balder (MAX IV), strategic planing of the experiments and execution of the experiments, mainly in charge of experimental sample preparation and data collection, data processing, model calculation, theoretical qualitative analysis, as well as the figures for the manuscript, and contributions to writing of the manuscript.

Abbreviations

Here follows a list and short explanation of the different abbreviations used in this thesis.

ATP	Adenosine triphosphate
BNC	Binuclear Center
C*c*O	Cytochrome *c* Oxidase
CCP4	Collaborative Computational Project Number 4
DED	Difference Electron Density
DFT	Density Functional Theory
DTBA	Dithiobutylamine
DTT	Dithiothreitol
EED	Extrapolated Electron Density
EPR	Electron Paramagnetic Resonance
EXAFS	Extended X-ray Absorption Fine Structure
FT	Fourier Transform
FWHM	Full Width at Half Maximum
GDVN	Gas-Dynamic Virtual Nozzles
HCOs	Heme-Copper Oxidases
HVE	High Viscosity Extrusion
LCP	Lipid Cubic Phase
LUMO	Lowest Unoccupied Molecular Orbital
MO	Monoolein
MX	Macromolecular Crystallography
NaDt	Sodium dithionite
NMR	Nuclear Magnetic Resonance
PDB	Protein Data Bank
PEG	Polyethylene glycol
PLS	Proton-Loading Site
SFX	Serial Femtosecond Crystallography
SSD	Solid State Detector
SSX	Serial Synchrotron Crystallography
SX	Serial Crystallography

TLS	Translation-Libration-Screw
TMH	Transmembrane Helix
TR-SFX	Time-Resolved Serial Femtosecond Crystallography
UV-Vis	Ultraviolet-Visible
XANES	X-Ray Absorption Near-Edge Structure
XAS	X-Ray Absorption Spectroscopy
XES	X-Ray Emission Spectroscopy
XFEL	X-Ray Free Electron Laser
XRF	X-Ray Fluorescence

Contents

Chapter 1

Introduction

1.1 Oxygen, cellular respiration, energy, and life on Earth

The Earth was formed 4.6 billion years ago as a hot globe with iron and silicium core, molten surface, and no atmosphere. To become habitable for the living world that we know today, the Earth had to go through a radical chemical evolution, which was enabled by a number of geological, and later on, biological phenomena.

The release of volcano fumes containing hydrogen sulfide (H_2S), methane (CH_4), and carbon dioxide (CO_2), led to formation of the Earth's first atmosphere [1]. With the gradual cool-down of the Earth surface, and the first rains, first oceans were formed. Shallow aqueous environments, where a pool of small molecules was in contact with mineral surfaces, containing elements of variable redox states, such as iron, manganese, and copper, were the sites of first organic catalysis. First unicellular organisms date to 3.7 billion years ago [2], and were formed in hydrothermal environment of prebiotic seas as anaerobs, retrieving energy from the process of chemiosmosis.

Due to the strong reducing conditions that existed on the primordial Earth's surface, and relative absence of O_2, these organisms were sustained on metabolic pahtways that predominantly used CO_2 and SO_4 as electron acceptors. Interestingly, proton gradients formed by alkaline hydrothermal vents [3] are suspected to be central to the origin of life, as they provide the energy force for synthesis of energy-conserving molecules.

Biological and geological processes led to a notable increase in O_2 production relative to its consumption [4]. Most notably, the emergence of cyanobacteria as the only prokaryotic organisms that perform oxygenic photosynthesis [5], led to significant rise of oxygen concentration in the atmosphere and oceans around 2.2 - 2.4 billion years ago, often referred to as the Great Oxidation Event (GOE) [6].

Presence of molecular oxygen has allowed for the use of O_2 as an electron acceptor with one of the largest free energy release per electron transfer. Consequently, energy-efficient metabolic pathways enabled the diversification of complex life forms. For example, aerobic metabolism yields at least 4-fold more energy per molecule of glucose oxidized than the most efficient anaerobic pathways [7]. This process is called aerobic respiration, and it consists of glycolysis, the citric acid (Krebbs) cycle, and oxidative phosphorylation. Per one molecule of glucose, up to 38 molecules of adenosine-3-phosphate (ATP), a high-energy conserving molecule, are produced during aerobic respiration, out of which 32 are produced solely in oxidative phosphorylation.

1.1.1 Oxidative phosphorylation and electron transport chain

Oxidative phosphorylation is a process consisted of, as name indicates, series of redox reactions with purpose of generating the electrochemical proton gradient often referred to as "proton motive force" [8], which drives the energy-demanding phosphorylation of ADP to store the energy in ATP, a molecule with high-energy chemical bonds that are cleaved in biological processes that require energy, such as growth, reproduction etc.

Electron transfer and oxidative phosphorylation 1.1 take place in four large protein complexes embedded in the membrane, particularly the inner membrane of mitochondria in eukaryotic organisms, or the inner (cytoplasmic) membrane of bacteria and archaea. Respiratory electron transport chains can vary greatly among organisms in terms of electron donor substrates, electron carriers, and number of proteins involved in this function.

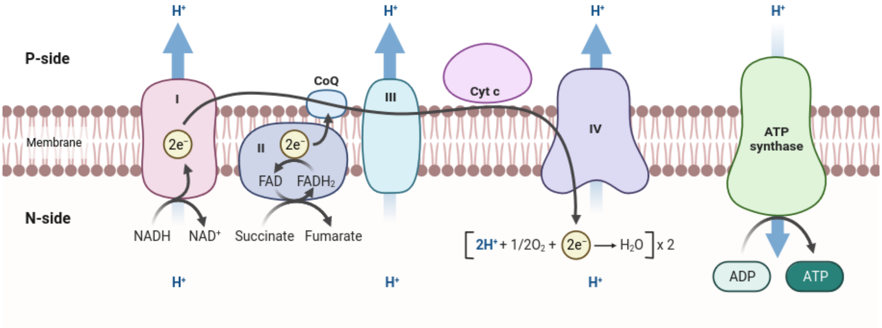

Figure 1.1: A schematic overview of electron transport chain and oxidative phosphorylation. Oxydative phosphorylation begins with NADH, a reduced form of nicotinamide adenine dinucleotide (NAD^+), that takes up an electron pair and H^+ during the glycolysis. Electrons from NADH are transferred to flavin mononucleotide and then, through an iron-sulfur carrier, to coenzyme Q (ubiquinone) by complex I, NADH:ubiquinone oxidoreductase. Coenzyme Q facilitates the movement of electron along the membrane to the complex III. Complex II receives electrons from succinate, an intermediate from citric acid cycle, and transfers them down the same path. Electrons first bind complex II to form $FADH_2$, after which they are transferred to coenzyme Q. In complex III, electrons are transferred from cytochrome *b* to cytochrome *c* in an energy-yielding reaction ($\Delta G^{\circ\prime} = -10.1$ kcal/mol). Cytochrome *c*, a peripheral membrane protein bound to the outer face of the inner membrane, carries electrons to complex IV (cytochrome *c* oxidase), where they are finally transferred to oxygen molecule, yielding two water molecules and free energy of $\Delta G^{\circ\prime} = -25.8$ kcal/mol. The proton gradient created by complexes I, III, and IV, is harvested by ATP synthase in the energy-demanding phosphorylation of ADP to ATP. *Created with BioRender.com*

Overall, the electron transport can be summarized in reaction:

$$\mathrm{NADH} + \frac{1}{2}\,\mathrm{O_2} + \mathrm{H^+} \longrightarrow \mathrm{H_2O} + \mathrm{NAD^+} \qquad (1.1)$$

with the standard Gibbs free energy of –220.1 kJ·mol^{-1}. It is important to note that this reaction is exergonic. Electron transfer from a low redox potential donor to a higher redox potential acceptor in three complexes (I, III, and IV) is coupled to proton transfer from the matrix to the intermembrane space [9].

Resulting unequal distribution of protons creates a pH-gradient and a transmembrane electrical potential. Therefore, the proton motive force can be defined as a sum of chemical gradient (ΔpH) and charge gradient ($\Delta\psi$):

$$\Delta p = \Delta\psi - 2.3RTF\Delta\mathrm{pH} \qquad (1.2)$$

where Δp is the membrane potential and ΔpH is the pH difference across the membrane, both expressed as the matrix values subtracted from the cytoplasmic values.

This mechanism, commonly known as "chemiosmotic hypothesis" [8], was first proposed by Peter Mitchell in 1961 as a quite radical explanation of the oxidation of NADH being coupled to phosphorylation of ATP. Today, his hypothesis is supported by a number of great evidence. For example, the membrane potential is measured to be 0.14 V, with the outside being positive and 1.4 units lower pH, corresponding to a free energy of 21.8 kJ per mol of protons. A very elegant demonstration of chemiosmothic hypothesis was carried out using bacteriorhodopsin, a membrane protein from halobacteria that pumps protons upon illumination, as a respiratory chain model [10]. When synthetic vesicles containing bacteriorhodopsin and mitochondrial ATP synthase were exposed to light, ATP was formed, proving that the respiratory chain and ATP synthase are biochemically independent systems linked only by a proton-motive force.

1.1.2 Heme-copper oxidases

C*c*Os, along with the bacterial quinol oxidases, belong to terminal heme-copper oxidases (HCOs) [11], a superfamily of enzymes found in the aerobic respiratory chain of mitochondria and bacteria that convert oxygen to water and transfer protons across membranes to form an electrochemical gradient. Based on differences in subunit composition, heme groups, and electron donors, HCOs can be divided in three sub-families: A, B, and C, each of them displaying the unique proton-pumping fingerprint [12]. Despite the evolutionary divergence between HCO families, the key functional elements for the process of oxidative phosphorylation are highly conserved across species. C*c*Os typically contain a low spin six-coordinate heme (heme *a* or *b*) ligated by two axial histidyl ligands, and a binulear center (BNC), consisted of characteristic five-coordinate, single axial ligand high-spin heme a_3, and a copper ion, conventionally referred to as $\mathrm{Cu_B}$. Heme *a*(*b*) and heme a_3 have different redox potentials due to the difference in the surrounding environment and the localization within the protein, resulting in unidirectional electron flow from heme *a* to binuclear center, the active site where the reduction of oxygen takes place.

***aa_3*-type** The largest and the most studied group of C*c*Os are aa_3-type oxidases. In particular, a mitochondrial cytochrome *c* oxidase, being one of the most important proteins in the powerhouse of the cell, is an aa_3-type oxidase. The first crystal structure to be completely solved was the aa_3-type C*c*O from *Paracoccus denitrificans* at 2.8 Å resolution [13], followed by the bovine heart C*c*O in 1996 [14], and *Rhodobacter sphaeroides* C*c*O [15].

All aa_3-oxidases consist of highly conserved subunit I, II, and III. aa_3-oxidase of *R.sphaeroides* and *P. denitrificans* contains one additional subunit. In eukaryotic organisms, however, mitochondrial C*c*O forms a large 220 kDa complex in which, in addition to three conserved subunits coded in mitochondrial DNA, 10 additional subunits are coded in the eukaryotic genome.

Subunit I harbors the catalytic heme a_3-Cu$_B$ binuclear centre, and its immediate electron donor, the low-spin heme, and therefore is common to all heme–copper oxidases. It consists of 12 transmembrane helices with hydrophilic loops localized on the P- and N- side of the membrane. Fe- and Cu- metal centres are well embedded in the protein, located at approximately 13 Å from the positive (outer or periplasmic) side, and 30 Å from the negative (inner or cytoplasmic) side of the membrane [12–14]. Interestingly, mitochondrial aa_3 -type C*c*O contains a zinc ion in proximity to heme *a*, but its function is yet unknown.

Given their critical role in oxygen diffusion, proton pumping, and electron transfer, several aminoacid residues of subunit I are considered to be strictly conserved in all C*c*Os. Notable examples include: six histidine residues in the heme coordination environment (HisI-61, HisI-378, HisI-376, HisI-291, HisI-290 and HisI-240, *Bos taurus* numbering); ValI-279 as a part of an O_2 diffusion channel; TrpI-280, proposed to be important for the so-called "histidine cycle mechanism" [16]; and an arginine pair (ArgI-438 and ArgI-439), which is connected to the δ-propionate of the low-spin heme via hydrogen bond, facing the positive side of the membrane, playing role in the proton exit mechanism.

Subunit II consists of large cluster of ten beta sheets on the P-side of the membrane. Most importantly, this subunit contains Cu$_A$, a copper site consisted two copper ions, which accept electrons from cytochrome *c*, therefore being a starting point of the electron transfer in C*c*Os. Subunit II associated with subunit I via two alpha helices [17]. Moreover, a magnesium ion is burried between subunit I and subunit II of aa_3-type C*c*O, taking part in re-localizing waters produced at the BNC in the reaction of oxygen reduction [18]. Along with the subunit I, subunit II is present in all C*c*Os.

Subunit III, however, is unique for the aa_3-type C*c*Os. Even though it has no direct role in redox processes, it increases the catalytic lifetime of C*c*O. In particular, by increasing the proton uptake, it shortens the life-span of reactive oxygen species which could affect the activity of the enzyme [19].

ba*$_3$-type oxidase from *T. thermophilus B-type oxidases are a diverse subfamily of C*c*Os spread among bacteria and archaea [17]. The first crystal structure of a B-type C*c*O to be determined to a resolution at 2.4 Å [17] was *ba*$_3$-type C*c*O from *Thermus thermophilus*.

ba$_3$-type C*c*O consists of three subunits (Figure 1.2) encoded by three separate structural genes [20]. Interestingly, *ba*$_3$-oxidase shows very little sequence homology (<20% identity [20]) with *aa*$_3$-oxidase, lacking most of the highly conserved amino acid residues that form the proton pathways. Still, it displays the similarity of structure with respect to its main subunits I and II.

The 61.7 kDa subunit I contains one helix in addition to 12 TMH described for A type C*c*Os [21]. An interesting difference is the reduced length of the P- and N-side hydrophilic loops, which decreases the entropy of unfolding [22,23], and might be one of the key contributors to increased thermostability of *ba*$_3$-C*c*O.

Important difference between the *ba*$_3$- and *aa*$_3$-type C*c*Os sprouts from the difference in heme groups.

In contrast with the typical heme *a* structure of *aa*$_3$-C*c*O, where hydroxyethylfarnesyl (HEF) is present on C2, a formyl group at C8 and a hydrophobic hydroxyethylgeranylgeranyl (HEGG) moiety are present on the heme *b* of *ba*$_3$-C*c*O. Rigid straight structure that reaches to the cytoplasmic side [24] and the increased hydrophobicity of HEGG compared to HEF are proposed as stabilizing at high growth temperatures [24, 25] in organisms such as *T. thermophilus* and other thermophilic bacteria, as well as phylogenetically-related archaea.

Heme *b* is axially ligated by two histidine ligands (His72 and His386) whereas His233, His282, His283, His384 and Tyr237 form the coordination sphere of the heterodinuclear center.

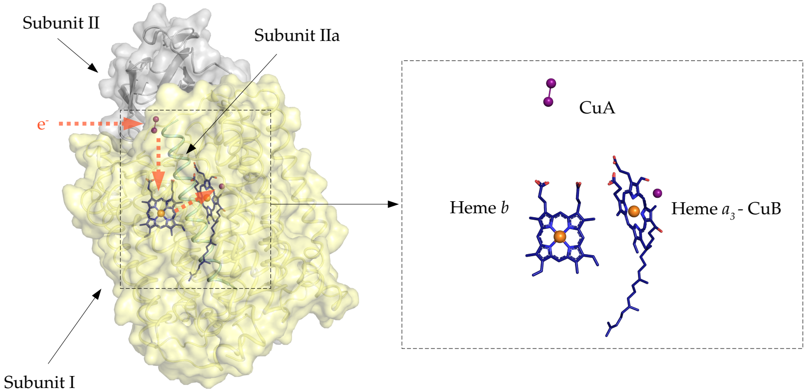

Figure 1.2: *ba*$_3$-type CcO of *T. thermophilus*. *ba*$_3$-C*c*O is consisted of three subunits. Subunit I harbors a low spin six-coordinate heme *b*, and a binuclear center (BNC) consisted of five-coordinate high-spin heme *a*$_3$ and a copper ion Cu$_B$. Cu$_A$ site, consisted of two Cu atoms, is located in subunit II, where it accepts electrons from cytochrome *c*. Electronic configuration and relative placement of redox centers (zoomed view) determines the electric potential and allows for a directed flow of electrons (orange arrows) from the protein surface through the protein matrix.

Subunit II (18.5 kDa) consists of β-sheet cluster and one single TMH, making up a the only predominantly polar domain, localized at the P-side of the membrane. It contains the binuclear copper redox center Cu$_A$, accepting electrons from the heat stable protein cytochrome c_{552} [21]. The first copper atom (CU1) is coordinated by CysII-149, CysII-153, HisII-157 and GlnII-151 while the second copper atom (CU2) is co-ordinated by CysII-149, CysII-153, HisII-114 and MetII-160. Conserved aromatic residues PheII-88 and TyrII-90 mediate the electron transfer via hydrophobic substrate–enzyme interaction [26], which could be an adaptation to compensate for weakened electrostatic interactions at elevated temperatures.

The third subunit, IIa, was first discovered and identified during determination of the first X-ray crystallography structure of *ba*$_3$-C*c*O. It is a 3.8 kDa polypeptide consisted of 34 residues, which form a single TMH [17]. The role of subunit II in stabilization of *ba*$_3$-C*c*O was accessed by overexpression studies [27]. Interestingly, it is speculated to be the 'missing' helix of *Thermus* subunit II, and therefore its functional complement. Moreover, superposition of subunit IIa helix shows structural similarity with the TMH of subunit II in all of the known C*c*Os.

1.1.3 Catalytic reaction of C*c*O

C*c*O contains four distinct and spatially separated redox centres. Electronic configuration and relative placement of these redox centers determines the electric potential and allows for a directed flow of electrons from the protein surface through the protein matrix, ultimately reaching its end point in the active site where reduction of oxygen takes place.

Long-distance transfer of electrons in protein matrices occur by a quantum mechanical phenomenon called electron tunneling. The carrier medium, i.e. the protein matrix, lowers the tunneling energy between redox-active metal clusters, allowing the electrons to travel up to 30 Å within only 10 fs [28].

The reaction mechanism of C*c*O is hereby described using the example of *aa*$_3$-type C*c*O, featured in a number of studies [29].

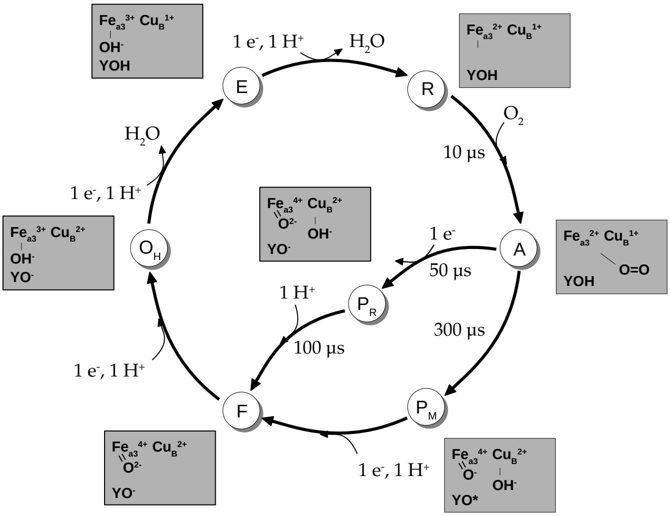

Figure 1.3: Reaction cycle of C*c*O. Events and timescales correspond to intrepretation of catalytic cycle in mitochondrial *aa*3-type C*c*O [30,31].

The redox cycle is initiated by the transfer of two electrons from cytochrome *c*, which docks onto the surface of subunit II, to $\mathrm{Cu_A}$ site, consisted of two Cu atoms at 2.5 Å distance located in subunit II. From $\mathrm{Cu_A}$, electron is transferred via low spin heme *a* to the binuclear center (BNC) [32,33]. BNC is consisted of a high-spin heme a_3, antiferromagnetically coupled to a single copper atom, $\mathrm{Cu_B}$. $\mathrm{Cu_B}$ is the first one to accept electrons in BNC, after which they are transferred to heme a_3. BNC reduced with two electron is denoted as the R-state (Figure 1.3). Fe(II) of a reduced heme a_3 can bind oxygen with a high affinity. A single oxygen molecule is the terminal electron acceptor in the process, taking up the two electrons donated by heme a_3. Original proposal suggests that two electrons are transferred onto the bound dioxygen creating a peroxide in the BNC, and therefore this state is termed as the P-state [34,35]. Results of resonance Raman spectroscopy and magnetic circular dichroism spectroscopy [36,37] have challenged the peroxide hypothesis, indicating that the dioxygen bond is already broken in the P-state. However, for the splitting of the dioxygen bond four electrons are required. In the P-state, the third electron is provided by Cu_B, which in turn oxidizes the ferrous iron Fe(III) into Fe(IV) and Cu_B(I) to Cu_B(II). Different donors of the fourth electron are proposed, and depending on the redox state of the heme *a*, the donation of the last electron needed for the reduction of oxygen can proceed via different mechanisms [38]. If an electron is available on heme *a*, the A state decays to the so-called P_R intermediate, characterized by the oxidation of heme *a*. This is available when the reduction of the BNC is assisted by external reducing agents (i.e. sodium dithionite, DTT, ascorbate etc.). Alternatively, if further electrons are not available on the protein metals beyond, the A state will transition to P_M intermediate. In this scenario, the most favored proposition considers the last electron being donated by a hydroxyl-group from the redox active conserved tyrosine in the catalytic site [39,40].

A rapid four-electron reduction of O_2 bypasses the formation of toxic reactive oxygen species (superoxide, peroxide, hydroxyl radical) [41], as the Fe(IV) double-bond O_2- state and Tyr radical formed at the catalytic site remain bound to the C*c*O. It is important to note that the formation of P_M does not require any additional input of electrons or protons, but instead is formed by rearrangement electrons and protons already present at the catalytic site.

Interestingly, P_M intermediate can be obtained in a relatively stable form just a few minutes upon oxygenation of the so-called "mixed valence CO" (MVCO) enzyme [42].

The conversion from P-state to F-state, in which one of the oxygen atoms has been bound to the heme a_3 Fe via a double bond, forming an oxoferryl moiety, is followed by translocation of two more protons from the intracellular to periplasmic side, for a total of four protons in the whole cycle, and the release second oxygen atom as water.

The enzyme returns to the “active-ready” oxidized state (O_H), which contains a bound hydroxide molecule and can accept new electrons, is not equivalent to the enzyme in the oxidized “resting” state (O). O_H state relaxes into O-state, a form that does not pump proton upon the first electron injection. The proton pumping activity is restored if the electron injection follows at least one oxidation cycle [43].

1.1.4 Proton transfer

All C*c*Os transfer protons during some steps of catalytic reaction. Even though all protons are taken up from the negatively charged N-side of the membrane, they can be differentiated into chemical protons, which are transferred to the active site and consumed in the reaction of reduction of O_2 to H_2O, and pumped protons, which are pumped across the membrane to the positively charged P-side, where they create a gradient which drives the synthesis of ATP by ATP synthase.

For the energy to remain conserved, C*c*O needs to take up the proton for pumping prior to the transfer of substrate proton to the catalytic site, where it will be used to form water [44]. This is enabled by the concept of a proton loading site (PLS), which represents a "storage" unit for the proton designated for pumping accross the membrane. The access of the PLS to either the N-side (proton-loading) or to the P-side (proton-pumping) is regulated by the change in proton affinity, as a result of different protonation states or conformational changes. Nevertheless, PLS represents an important gatekeeper in preventing the spontaneous flux of protons from the P- to the N-side [45].

As the reaction site is well embedded in the protein, intra-protein channels for proton conduction must be always present in subunit I.

A-type A-type C*c*Os (Figure 1.4 A) transport protons via two different pathways: D-pathway, named after entry point at aspartate (D), and K-pathway, starting with lysine (K). K-pathway is much more conserved across the C*c*O family than the D-pathway, which is relevant given the fact this pathway leads directly to the binuclear center.

Additional putative proton pathways such as bovine H-pathway [33] or the *P. denitrificans* E-pathway [46] have been proposed but no experimental evidences supporting the functionality of these pathways have been obtained.

In A-type C*c*O, all pumped protons and two chemical protons are taken up via the D-pathway, while the other two chemical protons enter via the K-pathway.

B-type In contrast, B- and C-type C*c*Os have solely one proton conducting channel to transport all chemical and pumped protons [47].

This channel (Figure 1.4 B) is identified within subunit I at the same position as the K-pathway of A-type C*c*O, so it is often referred to as the K-pathway analogue, even though it does not share significant sequence homology with the K-pathway of A-type C*c*O.

Efficiency of proton pumping In addition to four chemical protons, approximately 2 H^+ per O_2 molecule, or 0.5 H^+ per one electron, are pumped via K-pathway analogue. This number is doubled in A-type C*c*O (1 H^+ per electron). Overall reaction scheme in aa_3-type C*c*O can be summed as:

$$O_2 + 4\,e^- + 4\,{H^+}_{N_{\text{substrate}}} + 4\,{H^+}_{N_{\text{pumped}}} \longrightarrow 2\,H_2O + 4\,{H^+}_{P_{\text{pumped}}}$$

Findings by Wikströms group [8,87] suggest that the proton pumping yield of C*c*O depends on the "age" of the oxidized enzyme, i.e. the number of H $^+$ translocated across the membrane upon reduction of O is greater immediately after oxidation of the reduced enzyme R. This observation can be correlated to discovery of pulsed C*c*O, reported by Antonini et al. [49], who demonstrate that the functional and spectroscopic properties of oxidized C*c*O produced by reaction of R with O_2 (O_H state) are different from those of the resting (O) enzyme. Moreover, characterization of the "fast" and the "slow" form of C*c*O (assigned based on the reaction rates with cyanide [50]), which are different than O and O_H, adds onto the complexity of the structural and functional differences. A general two-state transition model between pulsed and resting state was proposed by Wilson et al. [51], and its implication is discussed in detail in work of Bloch et

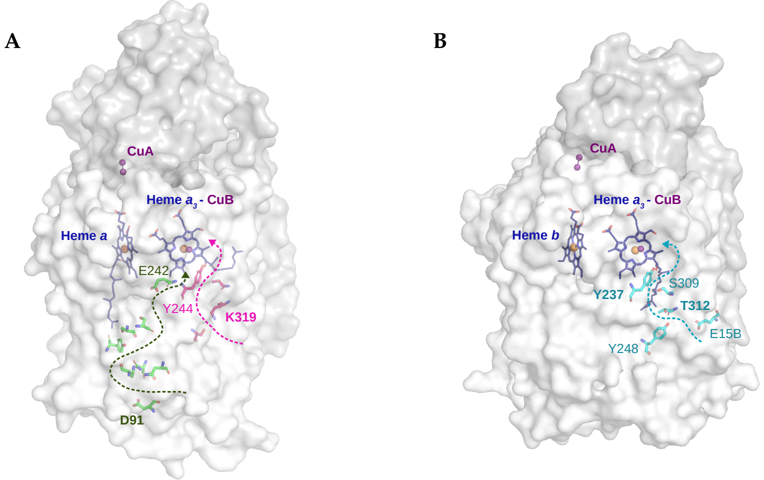

Figure 1.4: Proton transfer in aa_3- and ba_3-type CcO.A. D-pathway (green) begins at AspI-91 (D), and extends over AsnI-98, AsnI-163, AsnI-80, TyrI-19, SerI-156, SerI-157 to GluI-242 K-pathway (magenta) is spatialy separated from the D-pathway, and leads from LysI-319 (K), over ThrI-316, Ser255 all the way to active site TyrI-244, which is covalenty bound to one of the histidine ligands of Cu$_B$ (HisI-240). The numbering corresponds to *B. taurus* [48]. **B.** In K-pathway analogue (blue), LysI-319, ThrI-316 and SerI-255, are replaced by a hydrogen bond chain of ThrI-312, a SerI-309 and TyrI-248. GluII-15 at the entry point and TyrI-237 at the terminus are conserved for K-pathways across C*c*Os. The numbering corresponds to *T. thermophilus*.

al. [43] who argue that the efficiency of proton pumping, and therefore, the efficiency of ATP synthesis might be regulated by switching between two distinct catalytic pathways. In particular, when the reductive phase is not immediately preceded by oxidation, it follows a different reaction pathway no longer coupled to proton pumping.

1.1.5 Oxygen transfer pathway

Oxygen routes to the BNC were extensively studied in both A- and B-type C*c*Os.

In work by Oliveira et al. [52], after employing MD simulations supported by crystallography findings [13–15] and mutagenesis experiments [53], it was observed that O_2 does not diffuse unspecifically inside this protein but instead, uses three well-defined channels running from the interior of the membrane (where the solubility of O_2 is higher than in the aqueous phase) towards the C*c*O core.

The first proposed oxygen pathway of A-type C*c*O corresponds to the putative pathway identified by Iwata and co-workers after pressurizing *R. spheroides* C*c*O crystals with xenon [15]. This continuous, hydrophobic channel has two entrance points, located between helices 5 and 8 and helices 11 and 13 of subunit I, that merge together in a region close to the proton-gating residue, GluI-286(the residues are numbered according to the *R. sphaeroides*). This represents a constriction point which prevents the diffusion of O_2 to the BNC. In contrast, the second pathway has only one entry located between the transmembrane helices 13 and 16 of subunit I, with its terminus close to TyrI-288. Finally, the third proposed channel has its entry point in subunit II, runs parallel to hydroxylethylfarnesyl tail of heme a_3, and terminates just below TyrI-288.

Interestingly, the O_2-pathway in B-type C*c*O is considered to be structurally well established and understood. Xenon pressurization studies performed in ba_3-C*c*O from *T. thermophilus* [54, 55] revealed a "Y-shaped" hydrophobic channel, extending from the membrane region to the BNC. In contrast to A-type C*c*O, no constriction point was observed close to BNC. The constriction point of aa_3-C*c*O is defined by two large bulky residues of aa_3-C*c*O (TrpI-126 and PheI-63 in *B. taurus* [48]) narrowing the space for diffusion of oxygen. In *ba*$_3$-C*c*O, smaller residues (TyrI-133 and ThrI-231) are found in these positions, allowing for better access of O_2 to BNC. In addition, a highly conserved valine residue (ValI-236) of *ba*$_3$-C*c*O is proposed to be important for oxygen to access the BNC [56]. Mutagenesis studies of *T. thermophilus ba*$_3$-C*c*O revealed that as the mutant side chain is increased and protrudes more into the ligand cavity, the rates of ligand binding decreases correspondingly.

Nevertheless, structural differences of O_2 diffusion channels between *aa*$_3$- and *ba*$_3$- type reflect different functional environments and possible adaptation to conditions with limited oxygen supply.

1.2 Scope of the thesis

In this thesis, I present the two different approaches used to study *ba*$_3$-type C*c*O : serial crystallography, which utilizes synchrotron radiation and X-ray free electron laser (XFEL) pulses for microcrystal diffraction at room temperature to obtain details of protein structure and reaction dynamics, and X-ray absorption spectroscopy, which relies on principle of core electron transitions upon X-ray absorption to specifically characterize co-factors containing copper and iron in different redox states of *ba*$_3$-C*c*O .

Chapter 2

Methodology

2.1 X-rays and X-ray sources

2.1.1 The discovery and application of X-rays

X-rays were first observed and documented by William Röntgen in his article entitled "The X-rays" in 1895, as the mysterious (hence "X") light originating from the Crooks tube after high voltage is passed through it, selectively interacting with matter, and projecting on the nearby fluorescent screen:

> *If the hand is held between the vacuum tube and the screen, the dark shadow of the bones is seen upon the much lighter shadow outline of the hand.*

Further experimentation revealed that this mysterious light passes through most substances, like the soft tissues of the body, but leaves bones and metals visible, which is perfectly illustrated by one of the first X-ray images ever captured on film – a hand of his wife Bertha, with her wedding ring and hand bones clearly visible in contrast to the soft tissue of the hand.

Today, the high penetration depth and selective absorption of X-rays is well-understood and utilized in medical imaging, i.e. body parts with the highest electron density, such as bones, absorb X-rays and are visible in its clear shape. In addition, the advancements in X-ray radiography and the use of contrasting agents allow for imaging of the soft tissues [57], revealing fine anatomic details of examined tissues or whole organisms.

The discovery of X-rays was followed by extensive research, and a number of proposed applications. In 1912 Max von Laue proposed the use of X-rays to identify the structure of very small matter, like atoms, based on their crystal structure. In 1913, William Henry and Lawrence Bragg took this idea further, by solving the formula for determining structure from the characteristic pattern observed upon the interaction with X-rays. This mathematical relation, up to date known as "Bragg's Law", set grounds for the field of crystallography and studying matter at atomic resolutions.

Interestingly, many years after the X-ray phenomenon was observed, the occurrence of X-rays on a much higher scale was observed during the particle collision experiments, as a by-product of electron acceleration. The first experiments using "synchrotron light" from a particle collider were performed in 1956 at Cornell in the USA. Nowadays, there is around 40 large synchrotron sources dedicated solely to producing synchrotron light, supporting a vast range of scientific experiments with applications in engineering, energetics, material science, life sciences, environmental sciences, cultural herritage etc.

2.1.2 X-ray sources

The quality of the beam originating from X-ray source and fine-tuned by X-ray optics is typically quantified by metrics that account for number of photons, beam size, and beam divergence: *flux*, *flux density*, *brightness*, and *brilliance*.

Brilliance is source-dependent, hence different X-ray sources can differ greatly in brilliance. For example, X-ray free electron lasers provide 10 orders of magnitude greater brilliance compared to third-generation synchrotron light sources.

Synchrotron light sources A synchrotron is a circular accelerator in which accelerated charged particles, typically electrons and positrons, orbit around a circular, closed path. The circular orbit is obtained using magnetic fields - by placing bending magnets along the particle beam path, the orbit is bent, giving rise to strong emission of electromagnetic waves in a tangential direction referred to as "synchrotron radiation". Synchrotron radiation contains a continuous spectra of energies, ranging from infrared to X-rays, thereby supporting a range of experiments, particularly in diffraction studies, i.e. protein crystallography.

In protein crystallography, synchrotrons have been largely used for diffraction studies of large, rotating single crystals, mainly in cryogenic conditions. Collection of diffraction data using this method is still most common approach in resolving protein structures.

Still, technical limitations of synchrotron do not provide spatial or the time resolution required to execute delicate time-resolved crystallography experiments. Moreover, cryogenic conditions significantly limit the experimental setup and understanding of physiological phenomena. The development of X-ray free-electron lasers (XFELs) overcomes these limitations, providing coherent, high-intensity laser-like X-ray pulses of femtosecond duration, allowing to probe biological reactions at fast timescales.

X-ray free electron laser (XFEL) In XFELs, the X-rays are produced in pulses across tens to hundreds of meter long undulator sections. Initially, electrons emit incoherent radiation, which interacts with the oscillating electrons, and induces drifting into electron microbunches, thus becoming coherent. When the waves of emitted radiation are optimally superimposed, the emitted radiation power increases exponentially, resulting in high beam intensities and laser-like properties. This principle is known as self-amplified spontaneous emission (SASE), and it is the core operating principle the world's largest XFEL facilities.

The brilliance of XFEL sources is 10 orders of magnitude higher than the brilliance of third-generation synchrotron sources. XFELs are able to deliver sub-femtosecond X-ray pulses with photon energies up to 25 keV, wide range of pulse energies (few µJ to few mJ) and repetition rates reaching the megaherz levels. Ultrashort femtosecond high-intensity X-ray pulses can generate diffraction signals before destruction [58], and are therefore crucial in serial crystallography data collection, allowing for obtaining information on the protein structure before the onset of the radiation damage. High brilliance and ultrashort pulse duration allowed for high spatial and temporal resolution that was previously unattainable but required for time-resolved measurements of molecular dynamics. Furthermore, the ultrashort pulse mode allows for proteins to be studied at room temperature, eliminating the need for low temperature conditions used at synchrotrons to minimize the radiation damage. Therefore, XFELs provide an important opportunity to study time-resolved protein dynamics at room temperature.

2.2 Principles of serial crystallography

2.2.1 Crystal structure

Protein crystals can be viewed as highly-ordered arrangement of protein molecules in a periodic motif, which makes it fundamentally different from protein in solution or amorphous solid, and gives rise to unique ability of crystals to diffract X-rays. This motif, or a three-dimensional array of points, is called crystal lattice. Lattice points are separated by a translation vector a in one-dimensional space. Consequently, in three dimensional space, the points of lattice can be generated by applying vectors $\vec{a}$, $\vec{b}$, and $\vec{c}$. These three vectors, together with the inter-axial angles α, β, and γ, define a unit cell, the smallest repeating unit having the full symmetry of the crystal structure. Depending on the length and orientation of the vectors, unit cells exhibit various shapes. For example, if the vectors $\vec{a}$, $\vec{b}$, and $\vec{c}$, are of equal length and at right angles to one another, or $a = b = c$ and $\alpha = \beta = \gamma = 90°$, the unit cell is cubic.

Positions of crystal atoms in space, and their relationship to each other, was first summarized by a French crystallographer Auguste

Bravais, who classified seven crystal systems, where a group of atoms repeats indefinitely in three dimensions with respect to one of the 14 lattices, today known as Bravais lattices. Bravais lattice, or a space lattice, describes the translational symmetry of the crystal through geometric arrangement of lattice points. In addition to Bravais lattice, the symmetry operations can be defined by point group (32 possible) and space group (230 possible).

In general, proteins do not crystallize under normal physiological conditions in a living cell. To make them suitable for crystallography studies, isolated proteins are submerged to carefully selected chemical and physical conditions that induce crystallization. Crystallization methods are described in detail in 2.5.

2.2.2 Concepts of X-ray crystallography

Essentially, diffraction can be understood as coherent scattering, in which, due to the periodic repetition of highly ordered pattern of atoms, ions, or molecules, waves of incident and scattered electromagnetic radiation, gives rise to constructive interference in some directions, and cancels the signal in others.

When protein crystals are exposed to X-rays, diffracted X-rays are measured on a detector as spots of different intensities, forming a characteristic diffraction pattern (Figure 2.1). The spots are a result of crystal diffraction at a certain angle (commonly noted as 2θ) relative to the incident X-ray beam according to the laws of constructive interference in crystals, first described by Bragg and summarized by equation:

$$n\lambda = 2d\sin\theta \tag{2.1}$$

where d is the distance between parallel planes and θ is the angle of approach between the incoming X-rays and the crystal plane.

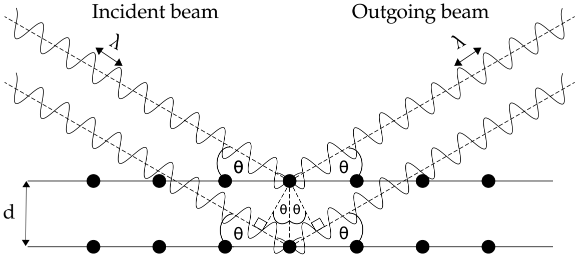

Figure 2.1: Bragg's law. When the incident X-ray beam of characteristic wavelength λ hits the crystal, it will scatter off the electrons found on a particular set of imaginary parallel planes. If the scattered wave and the outgoing X-ray beam are in phase for a given θ, constructive interference will occur, giving rise to a Bragg reflection.

The intensity of each spot in a diffraction pattern is determined by the number of electrons found on a particular set of imaginary parallel planes, called Bragg planes, that cross through the crystal. Spacing and direction of these planes in three-dimensional space is defined by three vectors commonly noted as $\vec{h}$, $\vec{k}$, and $\vec{l}$. To establish the connection between diffraction pattern and crystal configuration, the observed diffraction can be viewed as diffraction in reciprocal space, where a diffraction spot corresponds to reciprocal lattice point, defined by co-ordinates of $\vec{h}$, $\vec{k}$, and $\vec{l}$, called Miller indices. In other words, a single point in reciprocal space represents the infinite series of physical direct space planes.

A construction known as the Ewald sphere (Figure 2.2) can be applied to illustrate the relationship between the reciprocal lattice of the crystal, the wavevector of the incident and diffracted beam, and the diffraction angle 2θ. In two-dimensional reciprocal space, the Ewald circle represents all the possible points where planes (reflections) could meet Bragg's law.

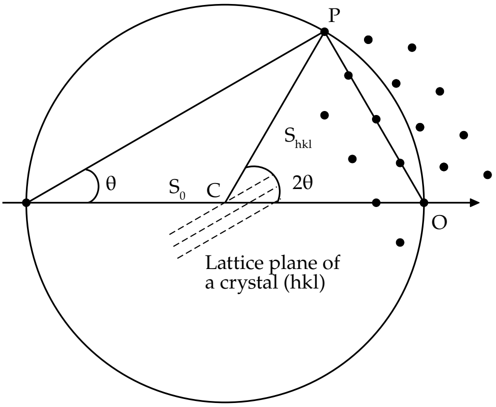

Figure 2.2: Construction of Ewald sphere. To fulfill Bragg's law and produce a reflection, the reciprocal lattice point must intersect with the Ewald sphere. Crystal lattice planes through reciprocal lattice points can be defined by Miller'indices (hkl). The distance $|OP|$ is equal to distance between planes in reciprocal space d^{-1}, and proportional to diffraction angle θ. To sample full reciprocal space, all reciprocal lattice points need to meet a diffraction condition, which is achieved by rotation of the crystal as a function of θ.

Essentially, for the reflection to occur, the reciprocal lattice space must intersect with the Ewald sphere. To maximize the amount of reflection data attainable from a crystal, the reciprocal space has to be extensively sampled by rotating the Ewald sphere around the origin O, thus bringing as many reciprocal lattice points in condition where Bragg's law is satisfied. In practice, this is achieved by rotating the crystal to cover a full diffraction space.

2.2.3 X-ray diffraction data analysis

Information about electron density can be successfully extracted from a diffraction pattern by applying Fourier transform. The Fourier mathematical operation sums the contributions of several simple functions (i.e. describing electron positions) with different frequencies, amplitudes and phases to generate a complex function which will return a complete electron density map.

Diffraction of a single reciprocal lattice point hkl can be described with structure factor F_{hkl} and expressed by equation:

$$F_{hkl} = |F_{hkl}|e^{i\phi hkl} = \sum_{j=1}^{n} f_j e^{2\pi i}(hx_j + ky_j + lz_j) \tag{2.2}$$

where $|F_{hkl}|$ is the amplitude, ϕ_{hkl} is the phase, and x, y, z are real space co-ordinates. The individual contribution of every atom to structure factor is denoted as f_j.

To convert a set of reflections into an electron density map, the knowledge of amplitudes of each reflection, as well as the phase, is required. While the amplitude can be derived from the spot intensity, it is not possible to measure the phase of the reflection, meaning the mathematical description of function is not sufficient to apply the Fourier transform and obtain the electron density map. This is known as "the phase problem". One of the most commonly used strategies to overcome the phase problem is molecular replacement, an iterative process of comparing the measured diffraction pattern ("observed") against a pattern predicted ("calculated") from a model protein structure for every possible position and orientation of the model, assuming the model protein structure exhibits high similarity with the unknown protein structure. Once the match has been found, it is assumed the unknown protein crystallized in a proposed orientation, and the phase values are therefore "borrowed" to replace the unknown phases.

With generated phases input and the experimentally observed amplitudes, it is possible to employ Fourier transform and retrieve the initial electron density map of the unknown structure. By fitting the known polypeptide chain sequence into the density features of the initial map, the initial model is generated, and used to calculate theoretical reflections and a new set of phases. Applying Fourier transform onto this theoretical input, combined with the experimental intensities, results in a new, improved electron density map, with improved phases. Moving from the protein backbone, the model can be further improved by adding solvent molecules and bound ligands into density features, or selectively modifying the fit of the side chains, and running a new Fourier transform. This step-wise process is called "structure refinement", and it continues until no further improvements can be made. The progress and the plausibility of refinement is validated by R-factor, also known as R_{work}, which gives an estimate of how well the refined model matches the observed data. R_{work} is defined as:

$$R_{\text{work}} = \frac{\sum ||F_{\text{obs}}| - |F_{\text{calc}}||}{\sum |F_{\text{obs}}|} \tag{2.3}$$

Where $|F_{obs}|$ are experimentally observed, and $|F_{calc}|$ calculated structure factor amplitudes. The values of R_{work} range from 0 to 1, where 0 is ideal, and practically not obtainable. A good rule of thumb is to aim for the value that is approximately 10 times lower than the proposed resolution cutoff. Bad fitting practice and including more information than supported by experimental data will result in "false low" values of R_{work}, commonly known as "over-fitting". To avoid over-fitting, a small portion of the total dataset (5 %) is selected before the refinement to generate R_{free}, while the rest of the data (95 %) will enter refinement cycles. For a valid model, the values of R_{work} should be close to those of R_{free} after refinement cycle. Nevertheless, a valid model should respect chemical constraints, such as bond lengths, bond angles, torsion angles, etc.

Electron density map calculations, model predictions, and structure refinement are executed using software suits for crystallography data analysis, such as *CCP4* [59], *Phenix* [60], etc. which contain a set of programs to conduct a whole analysis pipeline. Once fully refined, the structure is written out as a co-ordinate file, containing x,

y, z coordinates of each atom in the model. Most commonly used format is PDB, which stands for *Protein Data Bank*, an open-source, free database containing protein structures obtained by various structural biology methods (X-ray crystallography, NMR, etc).

2.2.4 Serial crystallography (SX)

The development of XFELs and the ability to study protein structures, and structural dynamics, at fast timescales and independent of cryogenic conditions gave rise to a different method of obtaining diffraction data. In serial crystallography (SX) [58], the crystal sample is consisted of slurry of randomly oriented microcrystals, and is constantly replenished throughout the diffraction experiment. This method relies on the concept of "diffraction before destruction", where a high-resolution diffraction image is recorded before the onset of the radiation damage caused by high-intensity X-ray pulse. Therefore, theoretically, one microcrystal equals one diffraction image, and the final dataset is the result of merging series of diffraction images.

Sample injectors To achieve the constant, uninterrupted sample flow, a suitable sample injector is required. The preferred flow rates are achieved by tuning the pressure (typically created with the use of a pump), which translates to mechanical components of the injector, and in turn moves the sample in downstream direction throughout the nozzle, creating the jet.

Depending on the phase of the sample, several injector types are defined. The first injector to deliver crystals in a flowing liquid suspension across an XFEL beam was gas-focused dynamic virtual nozzle (GDVN) [61], which is up to date one of the most commonly used injectors, particularly significant in "mix-and-inject" experiments for time-resolved studies. High sample consumption rates, typically at a speed of $10 - 20\ \mathrm{m/s}$, and incompatibility of liquid phase with insoluble, large proteins, like membrane proteins, drove the development of high-viscosity extrusion (HVE) injector [62] and [63] lipid cubic phase (LCP) extrusion injector. Due to the lower sample consumption and good flow rate control, use of HVE injector was extended to soluble, hydrophilic proteins, and a wide range of carrier media, such as grease matrix, agarose, hydroxyethyl cellulose (HEC) etc.

Detectors X-ray detector captures a diffraction pattern upon interaction of the crystal with X-ray. To be suitable for serial crystallography, a detector needs to meet the requirements of sensitivity, speed, dynamic range, resolution, and detector size.

2.2.5 Challenges of SX data analysis

Along with the advantages of this approach in comparison to traditional, single-crystal crystallography, serial crystallography comes with a few challenges in data treatment and retrieving the complete structural information.

Multiple crystals and partial reflections In SX data collection, the diffraction dataset is a result of diffraction of multiple microcrystals, randomly oriented in a sample slurry, moving across the beam of a defined size, with a certain velocity. As a result, not every crystal will be probed by and X-ray pulse, and crystals that are probed can give only partial reflections, as the full rotation angle is not accessed. Moreover, if the crystal density of the sample is too high, more than one crystal can be probed by a single X-ray pulse, generating a multihit. Since the SX data typically contains hundreds of thousands of images, differentiating between images in which diffraction is recorded (i.e. "hits") and images with no diffraction ("empty") significantly reduced the dataset size and computational resources required in the following steps. Data reduction is commonly performed during the SX experiment on-site ("online" processing) using programs for hit-finding, such as *Cheetah* [64].

Indexing and merging of partial intensities All images containing diffraction patterns are to be indexed independently, which is facilitated by programs specially designed for data treatment of SX data. One of the most commonly used software tools is *CrystFEL* [65], a suite comprising programs for indexing, merging, and statistical analysis of SX diffraction data. *Indexamajig* performs peak finding based on diffraction signal level thresholds and signal-to-noise ratio, accounting for physical parameters of the detector and the X-ray beam, provided by geometry file and mask file. Indexing is performed by one or the combination of the several fast Fourier transform (FFT)-based indexing algorithms, such as *MOSFLM* [66], *DirAx* [67], *XDS* [68], and *XGandalf* [69]. Additionally, other parameters, such as crystal orientation and unit cell parameters, are determined and accessible within the software package.

All intensities from indexed reflections are scaled and merged together to create a full list of reflection intensities in 3D reciprocal space. Merging in *CrystFEL* can be performed by either averaging and merging (*process_hkl*), or by scaling and post-refinement (*partialator*) of partial intensities.

Statistical analysis Figures of merits of the full dataset, as well as of individual resolution shells, are obtained from both the full reflection list (*.hkl*), and randomly split dataset files (denoted as)*.hkl1* and *.hkl2*). To compensate for crystal-to-crystal variation, the redundancy of data in SX experiment needs to be very high. Completeness is a measure of how well the experiment covered all the possible unique reflections, and it is usually 100% in SFX experiments, where a large number of diffraction images is collected. Completeness and average signal strength I/σ are calculated from the full reflection list (*.hkl*) using *check_hkl* [65]. The comparison of the split reflection lists (*.hkl1* and *.hkl2*) is accessed by *compare_hkl* [65], which calculates R_{split} and Pearson's correlation coefficients ($CC_{1/2}$, CC^{*}). R_{split} is a measure of the probability that the similarity between two split datasets is stochastic, and is expressed as a percentage. $CC_{1/2}$ indicates how well one split dataset can predict the other based on correlation between intensity values of the datasets.

Electron density map and structure model Finally, a full list of reflection intensities is converted to *.mtz* file and further processed. For example, programs from the *Collaborative Computational Project 4* (*CCP4*) [59] can be used to execute a full map refinement pipeline. Structure factor amplitudes are calculated from the intensities using *Truncate*. Simultaneously, a *freeR* dataset is created, containing 5% of the total dataset, required for the statistical assessment of the plausibility of the following rounds of map refinement. Molecular replacement in *Phaser* and structure refinement in *Refmac*, as well as the model building in *Coot*, resemble the procedures in conventional crystallography, described previously in 2.2.3.

2.2.6 Time-resolved serial femtosecond crystallography (TR-SFX) at XFELs

Time-resolved X-ray crystallography aims to obtain X-ray diffraction data of time-dependent conformational changes, and thereby to provide insight into the chemical pathways underpinning biological reactions [70] To execute a time-resolved diffraction experiment, a reaction needs to be initiated within the well-diffracting crystals of the target enzyme in a rapid, uniform, and non-destructive manner. Moreover, the data collection setup has to enable for each diffraction frame to be collected faster than the reaction of interest.

Laue diffraction Pioneering time-resolved studies, the Laue diffraction [71] approach explored the possibility of exposing the crystal to a polychromatic X-ray beam, where in return more diffraction spots are sampled, allowing for data to be collected using much shorter X-ray exposures. Due to several limitations, time-resolved Laue diffraction has not found a more broad application. In contrast, serial crystallography successfully worked around shortcomings of Laue diffraction. By constant replacement of the sample, cyclic data-collection protocols, where protein returns to its resting state, are no longer required. Nevertheless, time-resolved Laue diffraction established the possibility to measure and visualize structural changes in real time.

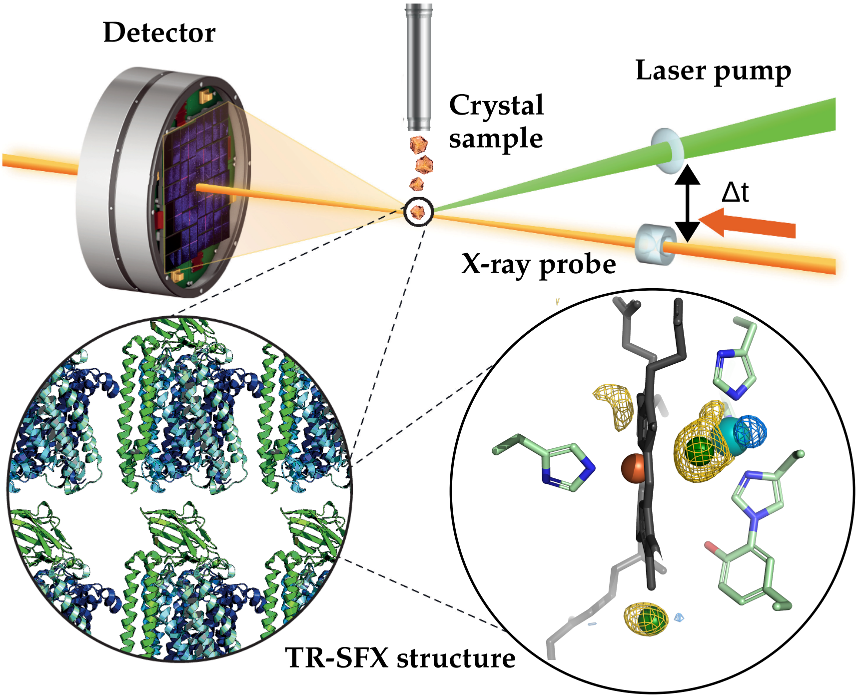

Figure 2.3: Pump-probe setup for time-resolved serial femtosecond crystallography (TR-SFX). Adapted from Brändén & Neutze, 2021. [70]

Pump-probe setup Nowadays, one of the most popular setups available at XFELs is a pump-probe setup [72], where microcrystals are injected across a focused XFEL beam, and excited by the laser ("pump") and probed by high-energy ultrafast X-ray pulses with the time-delay (Δt) (Figure 2.3). Data collection at room temperature allows for the reaction to be initiated and observed within the crystal. To successfully capture reaction intermediates, the duration of both the pump and probe pulses needs to be significantly faster than the lifetime of the respective intermediates. In addition, the readout frequency of X-ray detector needs to match the frequency of generated X-ray pulses.

TR-SFX of light-sensitive proteins An obvious target for TR-SFX are light-sensitive proteins, in which the conformational changes can be triggered in crystals by applying short laser pulses. In 2014, proof-of-principle time-resolved SFX experiment was executed at LCLS [73], where nanosecond laser was employed to excite the microcrystals of PYP at time delays of 10 ns and 1 µs . The experiment was repeated in 2016 using femtosecond laser. Due to their role in important biological functions and optogenetics applications, time-resolved studies of many other light-sensitive proteins followed, and soon became the focus of the field [73], [74], [75]. Still, light-sensitive proteins make up only a small portion of total proteins, which creates a gap and a need to tackle different forms of reaction initiation.

TR-SFX with different strategies of reaction initiation Significant efforts have been made to extend the application of TR-SFX to proteins that are not naturally light-sensitive. One of the successful strategies was the use of flow cell to initiate enzymatic reactions in crystals by reagent exchange, first time employed to study elastase [76] and glycogen phosphorylase [77]. Even though the theoretically predicted time for small molecules to diffuse into crystals might be plausible for rapid initiation of enzymatic reaction, mixing experiments can be very challenging in practice, especially when working in the viscous medium, like LCP. One strategy to ensure the proper diffusion of substrate into the crystals is to mix the reagents with the sample in advance.

The use of photocages builds on this concept, as it allows the infusion of the caged compound into the sample prior to the data collection. Moreover, it enables the application of the standardized pump-probe setup, as it involves a photosensitive component, which is readily decomposed upon light illumination, releasing the substrate in a time-controlled manner. The use of cage oxygen compound and the pump-probe setup for time-resolved SFX studies of ba_3-type C*c*O is described in 3.2.

Other notable examples of triggering reactions in a pump-probe setup include photopharmacological switches [78], electric fields [79], and temperature jumps [80].

Difference electron density (DED) maps To track time-resolved conformational changes, the observed structure factors from the reference dataset need to be subtracted from the time-dependent dataset, and visualized in a difference electron density (DED) map. Calculation of difference density maps can be readily performed by programs such as *Phenix* [81]. To be able to calculate a map, structure amplitudes and phases are required. Structural amplitudes are obtained by subtracting the observed structure factor amplitudes of the reference state $F_{obs}(\text{ref})$ from that of the activated state $F_{obs}(t)$ i.e., $\Delta F = F_{obs}(t) - F_{obs}(\text{ref})$. The phases are retrieved from the reference structure, so it is therefore important that the reference structure is completely and well refined, with the maximal possible accuracy of calculated phases. Calculation of DED maps is possible only for isomorphous datasets.

Once calculated, an isomorphous DED map displays the differences in atomic positions before and after the initiation of the reaction, in a form of complementary negative (by consensus: red) and positive (green) peaks of electron density. DED maps can sometimes detect even small displacements. Still, in a realistic TRX experiment, the occupancy of the triggered state can vary, and in some cases, it makes up a very small fraction.

Extrapolated electron density (EED) map Extrapolated electron density (EED) map can be calculated by extrapolating structure factors to 100% occupancy, thereby assuming a 100% of activated population . Recently published program called *Xtrapol8* [82] incorporates an automatized pipeline to extract structural information of the low-occupancy states.

2.2.7 Towards time-resolved serial synchrotron crystallography (TR-SSX)

Recent upgrades in X-ray optics at third-generation synchrotrons [83], as well as new high-throughput sample delivery methods and modern pixel array X-ray detectors, opened up possibilities to use serial synchrotron crystallography (SSX) to collect high-resolution diffraction data at room-temperature.

Historically explored in Laue diffraction experiments on single crystals [71,77,84], the means of conducting time-resolved studies at synchrotrons using serial crystallography have been out of particular interest. As most of the enzyme turnover happens on timescales from milliseconds up to seconds, the frequency and duration of X-ray pulses delivered at synchrotrons is well suited for time-resolved SSX.

Moreover, advancements in sample delivery strategies allow for rapid sample exchange and rapid diffusion of reagents into the sample, as well as the possibility for an adjusted pump-probe setup and photoactivation of the sample components. Classic injector systems [85], as well as capillary-based custom flow cells [86,87], have been successfully used in SSX data collection. Some of the notable recently developed flow-based delivery methods for SSX include the use of tape drive [88]. For example, an interesting setup developed at DESY allows to crystallize the protein in a drop-on-tape device directly before it being probed with the X-rays, i.e. *Just in time crystallization for easy structure determination* (JINXED) [89].

As an alternative to the injection systems, fixed-target systems were developed to reduce sample consumption and improve sample hit-rate. In addition, the ability to soak the sample with the reagent of interest, such as protein ligands, has made fixed-target a feasible approach in pharmacology studies, where high-throughput screening of chemical compounds or target proteins is a merit.

Radiation damage One of the biggest concerns in translating serial crystallography experiments from XFELs to synchrotrons is the radiation damage. Ultrashort X-ray pulses of XFEL sources allow the crystals to "escape" the secondary effects of the radiation damage, which is not the case at synchrotrons, where, due to the longer times of exposure to X-rays, the absorbed radiation dose is higher and the diffusion of radicals is facilitated.

In room-temperature SSX study on lyzozyme [90], dose limits indicate a half-diffraction dose of 0.38 MGy, with the site-specific damage occurring at approximately 80 kGy. Site-specific radiation damage is a particular concern in time-resolved studies, where it can obscure or even initiate a catalytic processes. One of the best example are metalloenzymes, in which the activity is dependent on the redox state of the radiation-sensitive metal co-factors. In those cases, the recommended dose limit can deviate from 0.38 MGy. Nevertheless, surpassing the recommended dose can compromise the dynamic range of TR-SSX difference maps, and therefore the interpretation of structural changes.

2.3 X-ray absorption spectroscopy (XAS)

2.3.1 Principles of X-ray absorption spectroscopy (XAS)

X-ray absorption spectroscopy (XAS) is a technique that measures X-ray absorption coefficient $\mu(E)$ as a function of the incident X-ray energy. The method utilizes X-rays from a tuneable source (such as synchrotron), covering typically medium and hard X-ray regime (2.4-40 keV at Balder, MAX IV, for example). Since every element absorbs a different wavelength of X-ray radiation, each measurement can be "tuned" to selectively probe element of interest, simply by adjusting the wavelength of the X-ray source.

X-ray absorption spectra (Figure 2.4) of any atomic or molecular material are characterized by sharp increases in absorption at specific X-ray photon energies, called absorption edges, which correspond to the energy required to eject a core electron into the lowest unoccupied molecular orbital (LUMO). When the absorption occurs at energies greater than the threshold for electron release, the core electron is excited to the so called "continuum", thus producing a photoelectron. Based on these two distinct phenomena, the X-ray absorption spectrum can be divided in two regions that provide complementary structural information: X-ray absorption near-edge structure (XANES), which contains the fingerprint of the electronic structure and symmetry of the absorbing element, and extended X-ray absorption fine structure (EXAFS), consisted of oscillation patterns as result of photoelectron scattering, carrying information on numbers, types, and distances to ligands and neighbouring atoms.

2.3.2 Application of XAS in structural studies

As one of the most powerful and widespread synchrotron-based methods, XAS is used in wide range of areas in both science (nuclear and coordination chemistry, materials science, environmental science, geology, life science) and industry (catalysts, photovoltaic devices, batteries, waste products), as well as conservation of cultural heritage objects.

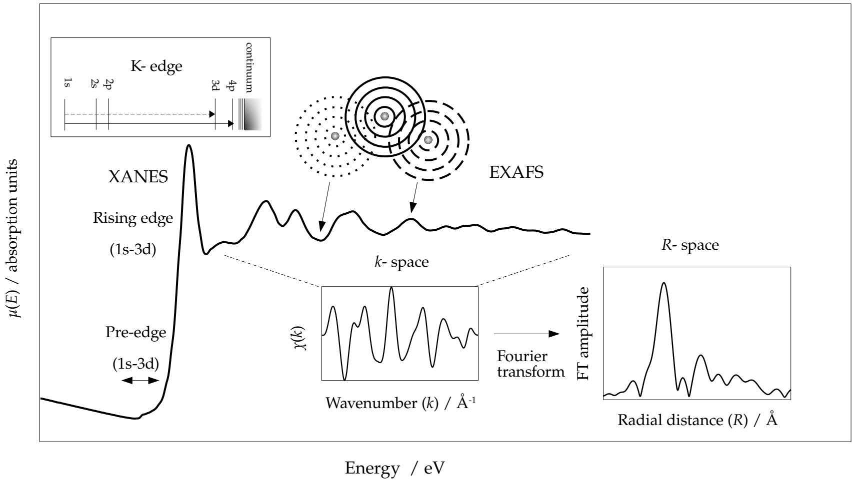

Figure 2.4: X-ray absorption spectroscopy (XAS). When X-ray is absorbed by the matter, an X-ray photon is absorbed by an electron in a tightly bound quantum core level (such as the 1s or 2p level) of an atom. When the photoelectron originates from a 1s core level, the absorption discontinuity is known as the K-edge. At energies higher than the energy of LUMO level, the absorption of an X-ray provides sufficient energy for ionization, where the absorbing atom releases the electron outside of the valence shell into the so called "continuum". Any excess energy provided to the system is carried off as transnational kinetic energy. A moving photoelectron scatters off the neighboring atoms. The backscattered electron interferes with the outgoing photolectron constructively (dashed line) or destructively (dotted), resulting in a jump or a drop of the wave amplitude. The oscillating part of the spectrum (EXAFS) can be expressed as $\chi(k)$, composed of sine waves in as a function of wavenumber k. By applying Fourier transform (FT), the EXAFS can be plotted as amplitudes $|\chi(R)|$ a function of radial distance R.

XAS is element- and orbital-specific, so it has found widespread application in bioinorganic chemistry, such as 3d-transition metal systems and metalloproteins.

Because it is sensitive only to the local metal site structure, XAS is not dependent on the phase or the medium of the sample. This means that biological samples can be measured in amorphous, crystalline or solution states, without interference from other elements from absorption by the protein matrix, water or air. Another important advantage of XAS is that the metal of interest is never 'silent' with respect to X-ray absorption spectra. This feature often makes XAS the only spectroscopic technique applicable to systems containing elements such as Zn(II), Cu(I), and Fe(II), which are commonly characterized as "spectroscopicaly quiet" in EPR, optical, or other spectroscopic methods. Finally, XAS experiments require a lower X-ray dose compared to crystallography experiments. Precise monitoring and control of radiation damage allow for the metal cluster to remain intact throughout the data collection [91,92].

Potential disadvantages of XAS when studying enzymes containing multiple metal atoms of the same element is the lack of selectivity, meaning that all the absorbing atoms of the same element will be probed simultaneously by the element-specific X-ray energy, giving the bulk total signal. With regards to signal being propotional to number (concentration) of the absorber atoms, biological samples (such as proteins in solution) produce low-intensity spectra, compared to well-ordered solids of anorganic materials. Depending on the phase and the concentration of the absorbing element, different measurement strategies are applied.

2.3.3 XAS data collection

The energy dependence of the absorption coefficient $\mu(E)$ is commonly measured either in transmission as:

$$\mu(E) = \log(\frac{I_0}{I}) \tag{2.4}$$

or in X-ray fluorescence (or, in some cases, Auger emission) as:

$$\mu(E) \propto \frac{I_f}{I_0} \tag{2.5}$$

where I_f is the monitored intensity of a fluorescence line (or Auger electron emission).

Fluorescence mode The incident transmitted I is directly connected to sample thickness. To measure very thin samples, or biological samples where high concentration of the absorber is not attainable, fluorescence mode is preferred strategy of measurement. In particular, if the probed element is diluted in its matrix, the total fluorescence yield is considered to be proportional to $\mu(E)$ [93]. In contrast, due to self-absorption of fluorescence, EXAFS can be completely wiped out in very concentrated samples.

If the ionization chamber is used to measure the fluorescent signal, the selectivity can be achieved by physically placing a filter made of $Z-1$ element that will absorb most of the the elastic and Compton scattering, and pass the K-fluorescence.

Alternatively, the energy discrimination can be performed electronically, for which it requires a high-resolution fluorescence detector. Fluorescence detectors used in XAS are predominantly Si- or Ge-solid state detectors (SSD) with the ability to achieve energy resolutions approximately 200 eV.

2.3.4 Data processing

Measured intensities are converted to $\mu(E)$ and corrected for eventual self-absorption effects and detector dead time. Scans containing damages (i.e. ice glitches) are selectively removed from individual channels. Single scans are commonly analyzed and merged for each sample condition to allow for comparison between samples, and the extraction of EXAFS signal. Baseline correction is done by subtracting a smooth pre-edge linear function fitted to a user defined range. The threshold energy (E_0) is identified as the energy of the maximum derivative of $\mu(E)$. In practice, the jump in the edge is approximated, and can differ from the tabulated edge value of the X-ray absorbing element. The spectrum is then normalized to this value by dividing the original data with the polynomial user-defined fit to the EXAFS range. To successfully isolate the EXAFS signal, the post-edge background is removed by subtracting a spline, a smooth function fitted to approximate the absorption from an isolated atom ($\mu_0(E)$) that cannot be experimentally measured. Fitting a spline imposes a certain risk, as a flexible spline can match not only the low frequency components of $\mu(E)$, but also high frequency components that contain EXAFS oscillation patterns, and result in loss of data signal. Finally, EXAFS is isolated as a function of wavenumber k, $\chi(k)$.

To emphasise fine EXAFS oscillations, $\chi(k)$ is k- weighted by multiplying to the potention of 2 (k2- weighted) or 3 (k3- weighted). $\chi(k)$ can be further transformed from so called "k-space" into R-space via Fourier transform (FT). FT is commonly used to analyse amplitude peaks $|\chi(R)|$ as a function of radial distance R from the absorbing atom, typically spanning from 1 to a few Å.

2.3.5 Interpretation of XANES

The qualitative interpretation of XANES typically relies on good literature knowledge of spectral features and their corresponding energy marks/values. Most of these "standards" are derived from XAS of various model compounds, and often sufficient for a simple qualitative XANES analysis. In practice, XANES analysis mainly considers the spectral features of the rising edge, and the pre-edge, but in some cases includes the region at the onset and above the edge (~30 eV) is dominated by multiple scattering events [94].

Pre-edge The pre-edge structures prior to K edges of first-row transition metals correspond to 1s→3d transitions, which are forbidden according to dipole selection rules ($\Delta l \pm 2$) but nevertheless observed due to 3d to 4p orbital mixing and as well as direct quadrupolar coupling. These transitions are possible only if the 3d orbital has an empty space (often referred to as "3d hole") to accommodate the 1s excited electron, and therefore not observed in d10 metals, such as Cu(I) and Zn(II).

In addition to electronic configuration, the pre-edge is particularly sensitive to metal co-ordination number and symmetry. For example, in two ions with unfilled 3d bands, Cr^{6+} and Cr^{3+}, the pd hybridization is much stronger for tetrahedral coordination (Cr^{3+}) than for octahedral coordination (Cr^{6+}), and the pre-edge will therefore gain intensity from 3d-4p mixing.

In summary, the pre-edge XANES contains electronic structure information on spin states, ligand-field strength and related energy splitting, covalency, and metal symmetry related 4p-mixing.

Rising edge The dominant contribution in K-edge corresponds to $1s \rightarrow np$ transitions, where np is the lowest unoccupied p orbital of the absorbing atom. Even though these transitions are dipole-allowed ($\Delta l \pm 1$) and significantly more intense than pre-edge transitions, in case of most transition metals, 1s to 4p transitions are often masked by intense onset of the rising edge. Still, there are some exceptions where 1s to 4p transition is observed as very intense feature of the rising edge, and is largely affected by the ligation environment of the metal.

For example, in Cu(I), the number of ligands affect the degeneracy of the unoccupied 4p orbitals, where different co-ordination geometries give rise to different intensities of 1s→4p transition. This region can therefore be a signature of a co-ordination geometry of Cu(I).

Oxidation state sensitivity The energy position of the rising edge derives from the effective nuclear charge (Z_{eff}) of the absorbing metal center, and is often used as an indicator of the oxidation state. Traditionally, this is explained via electrostatic model, which suggests that atoms of a higher oxidation state have a higher effective charge of nucleus, and therefore require more energy to excite a core electron. Conversely, the increase in negative charge shifts the edge to a lower energy.

Computational approaches The advancements in XANES theory have led to several *ab initio* codes for quantitative interpretation and modeling of XANES spectra. Examples of the most widely used codes are *FEFFF9* [95], *MXAN* [96], and *ORCA* [97]. In recent years, there has been a lot of focus on retrieving electronic structure of the low lying pre-edge region. For example, *ORCA* has been used to perform time-dependent density functional theory (TD-DFT) calculations for quantitative treatment of the pre-edge 1s→3d transition.

2.3.6 Interpretation of EXAFS using theory-based calculated model

The EXAFS equation At the energies high above the absorption edge, EXAFS is defined as a function of the X-ray energy, $\chi(E)$:

$$\chi(E) = [\mu(E) - \mu_0(E)]\Delta\mu_0(E) \tag{2.6}$$

where $\mu(E)$ is the measured absorption coefficient, $\mu_0(E)$ is a smooth background function which models the absorption of an isolated atom, and $\Delta\mu_0$ is the measured jump in the absorption $\mu(E)$ at the given threshold energy E_0.

X-ray energy is often converted to k, the wave number of the photoelectron, expressed in dimensions of $1/\text{distance}$, Å^{-1}, and defined as:

$$k = \sqrt{\frac{2m_{\text{e}}(E - E_0)}{\hbar^2}} \tag{2.7}$$

where E_0 is the absorption edge energy, m_e is the electron mass, and $\hbar$ is Planck's constant.

Consequently, EXAFS is commonly expressed as a function of k, $\chi(k)$. $\chi(k)$ is the oscillatory portion of the absorption coefficient, in which different frequencies apparent in the oscillations arise from different near-neighbor coordination shells. A "shell" is a group of elements with identical atomic number and similar distances from the absorber. Therefore, EXAFS spectrum $\chi(k)$ can simply be defined as a sum of the contributions of j atomic shells.

However, with increasing energy, a decay of EXAFS is observed, along with the increasing disorder. In real systems, there is an inherent static disorder due to a distribution of distances, and dynamic disorder due to thermal vibrations of the absorbing and scattering atoms. This is described by Debye–Waller factor, σ. Moreover, the loss of photoelectrons occurs due to inelastic scattering processes.

Therefore, the EXAFS data is mathematically treated as a damped sine wave and modeled by the following EXAFS equation:

$$\chi(k) = \sum_j \frac{N_j f_j(k) \exp[-2k^2\sigma^2] \exp[-2R_j/\lambda]}{k{R_j}^2} \sin[2kR_j + \delta_j(k)] \quad (2.8)$$

where scattering amplitude $f_j(k)$ and phase-shift $\delta_j(k)$ are scattering properties of the atom j neighboring the excited atom, N_j is the coordination number of neighboring atom, R_j is the distance to the neighboring atom, and σ^2 is the mean-square disorder of the neighbor distance.

Scattering amplitude and phase shift are directly dependent on the atomic number Z of the scattering (neighboring) atom and therefore crucial in modeling EXAFS spectra.

The EXAFS amplitude falls off as $1/R^2$. This reflects the decrease in photoelectron amplitude per unit area as one moves further from the photoelectron source (i.e. from the absorbing atom). As a consequence of the damping terms in Equation 2.8, EXAFS oscillations are typically only observed for atoms within approximately 5 Å of the absorbing atom.

EXAFS fitting using computational approaches EXAFS analysis entails fitting the experimental data output to the theory-based calculated model, and model interpretation to determine the radial distribution of atoms surrounding the absorbing atom.

The function is fit by making an initial guess of the atoms surrounding the absorbing atoms, and their corresponding parameters, given by the EXAFS equation 2.8. The total number of independent points (N_{idp}), i.e. the parameters that can be fitted is limited by the "reach" of experimental data:

$$N_{\text{idp}} = \Delta k \Delta R / \pi \tag{2.9}$$

where Δk and ΔR are the k- and R-ranges of the potentially "usable" data.

Assuming the phase shift $\phi(k)$ and amplitude reduction factor ${S_0}^2$ are known, one can determine:

R - distance to neighboring atom.

N - coordination number of neighboring atom.

σ^2 - mean-square disorder of neighbor distance.

Typically, the amplitude reduction factor ${S_0}^2$ is taken as a constant: $0.7 < {S_0}^2 < 1.0$ for a given central atom, and simply multiplies the EXAFS .

Phase shifts are routinely computed using Green's function formalism [98] with localized "muffin tin" potentials, the standard tool for calculating the potential surface of a cluster of atoms, based on input set of Cartesian coordinates, typically retrieved from experimentally obtained structures. Some of the first, and up to date, the most commonly used programs are *EXCURVE* [99], *GNXAS* [100], and *FEFF* [95], whether as a stand-alone, or incorporated into softwares for EXAFS analysis.

N_{j} , R_{j} , and σ_{j} are allowed to float until the best fit is reached. However, some treatments require these parameters to be constrained, i.e. for different paths or even different data sets. The value of each parameter included in the fit is reported in the log table, and often used as a "diagnostic tool" to determine the plausibility of the fit by comparing the reported value with the conventional values.

Finally, the overall "goodness of fit" is expressed by two key statistical metrics: reduced ${\chi_\nu}^2$ and R-factor.

${\chi_\nu}^2$ scales number of variables (N_{varys}) by the "degrees of freedom"

$${\chi_\nu}^2 = \chi^2 / (N_{\text{idp}} - N_{\text{varys}}) \tag{2.10}$$

where χ^2 is expressed as:

$$\chi^2 = \frac{N_{\text{idp}}}{\epsilon^2 N_{\text{fit}}} \sum_{i}^{N_{\text{fit}}} \left[{\chi_i}^{\text{measured}} - {\chi_i}^{\text{model}}(x)\right]^2 \tag{2.11}$$

Ideally, $\chi^2 \approx 1$ would imply that the experimental data is consistent with the mathematical fitting model. In EXAFS, however, χ^2 is rarely near 1, but as a rule of thumb, lower positive values of χ^2 are favored compared to higher.

R-factor for EXAFS can be defined as:

$$R = \frac{\sum_i^{N_{\text{fit}}} \left[{\chi_i}^{\text{measured}} - {\chi_i}^{\text{model}}(x)\right]^2}{\sum_i^{N_{\text{fit}}} \left[{\chi_i}^{\text{measured}}\right]^2} \tag{2.12}$$

Often interpreted as a percentage misfit or, conversely, an "overfit", R-factor is a useful metric of how closely the fitted function overplots the data. Still, using solely R-factor to evaluate the fit can be misleading, as good values can be obtained with physically unrealistic values of individual fitting parameters.

In conclusion, a good fitting practice relies on examining and fine-tuning the values of each parameter of the EXAFS equation to obtain the minimal values of ${\chi_\nu}^2$ and R-factor, with respect to physical constraints.

2.4 Protein production of ba_3-C*c*O

2.4.1 *Thermus thermophilus* as a host

Thermus thermophilus is a extremophilic gram-negative bacterium inhabiting hot springs, where temperatures can reach up to 70 °C. At these temperatures, the solubility of oxygen in water is about 60 % lower compared to its solubility at 25 °C.

As a facultative anaerob, *T. thermophilus* expresses two terminal oxidases: caa_3 type, which is continuously expressed, and ba_3-type, expressed in anaerobic or hypoxic conditions due to its higher affinity for oxygen compared to caa_3-type.

ba_3-C*c*O is expressed as a recombinant protein containing 6xHis poly-histidine tag on N-terminus of subunit I, and a kanamycine resistance marker in the transferred vector. The protein production in the host vector is optimized to maximize the cell yields according to protocol [27] and described as follows.

In the lab, *T. thermophilus* strain is grown as a cell suspension in 3 liter non-baffled flasks, filled with 2.2 L of growth medium (73 % of the volume), mildly stirring for 3 to 4 days at 60 °C in hypoxic conditions. Even though these conditions are optimal to induce ba_3-C*c*O expression, they result in a low cell mass yield. Still, using the native host for protein expression instead of optimized heterologous strain has multiple advantages, such as higher accuracy of post-translational modifications (i.e. glycosilation) and folding, reduced risk of inclusion body formation, etc.

2.4.2 Protein purification

Based on the protein physical and chemical properties, such as size, solubility, and reactivity, and importantly, localization in the cell, different strategies are applied to extract and purify proteins from the cell. To access the content of the cell, a cell can be disrupted chemically (e.g. high salt content or detergents), enzymatically (e.g. deoxyribonuclease (DNAse)), mechanically (e.g. sonication or homogenization under high pressure), or by the combination of these methods. Cell components, such as individual organelles, cell walls, membranes, and cytoplasm, are separated via centrifugation according to their characteristic sedimentation coefficient. Extraction of membrane proteins require not only disruption of the cell, but as well a membrane disintegration and release of the protein into the solution, where it can be easily separated from membrane components by ultracentrifugation.

Once extracted, the protein is purified using chromatography, a set of techniques based on the adsorption and/or partition of the molecules to be separated between a mobile and a stationary phase. Commonly used high-performance liquid chromatography (HPLC) employs standardized, automatized system in a controlled environment and the ability to carefully monitor parameters such as pressure, ionic strength, time, absorbance etc.

2.4.3 Quantification and characterization of *ba*$_3$-C*c*O

UV-Vis absorption spectroscopy of ba$_3$-type C*c*O *ba*$_3$-C*c*O, as a member of heme-copper oxidase protein family, contains two hemes, heme *b* and heme *a*$_3$, playing an important role in electron transfer. Moreover, heme *a*$_3$ harbors the oxygen in the active site of the enzyme, where reduction of oxygen takes place.

Generally, a heme group consists of a di- or trivalent iron, and a porphyrin, an aromatic macrocyclic structure composed of heterocyclic organic compounds, with one or more side chains attached. It contains a system of conjugated double bonds, which are especially sensitive to light, and as such give rise to absorbtion in UV-Vis range. The difference in porphyrin architecture defines the structural difference between heme *a* and heme *b* (else refered to as "protoheme IX"), where heme *a* contains a hydroxyethylfarnesyl group instead of a vinyl side group at the C_2 position, and a formyl group instead of a methyl side group at position C_8.

Heme *a* of *aa*$_3$-type C*c*O is replaced by heme *b* in *ba*$_3$-type C*c*O, while heme *a*$_3$ of the binuclear active site is conserved across the protein family. In a resting state of the enzyme, heme *b* is in low spin, and heme *a*$_3$ in high spin state.

Hemes typically absorb in the blue wavelength region around 400 nm of the visible spectrum, giving rise to a Soret peak, a spectral feature resulting from an electron dipole transition that allows $\pi - \pi^*$ transitions. In case of *ba*$_3$-C*c*O, a Soret peak arises due to the absorption of a low-spin heme *b*. The spectral shift of Soret peak indicates a change of redox state of heme *b* Fe, where the shift towards higher wavelengths indicates the reduced Fe(II) state. In addition, a Soret peak of reduced *ba*$_3$-C*c*O contains a characteristic "shoulder", which is a contribution of the reduced heme *a*$_3$, and emerges at around 445 nm. The reduced state of *ba*$_3$-C*c*O is further characterized by two absorbance peaks at wavelengths of around 500 to 600 nm, called the Q-bands, including the small peak contribution from heme *a*$_3$ at around 600 nm. It is important to note that the absorbance fingerprint of C*c*O is influenced by physical and chemical conditions, such as temperature, phase, pH, and ligation events [36].

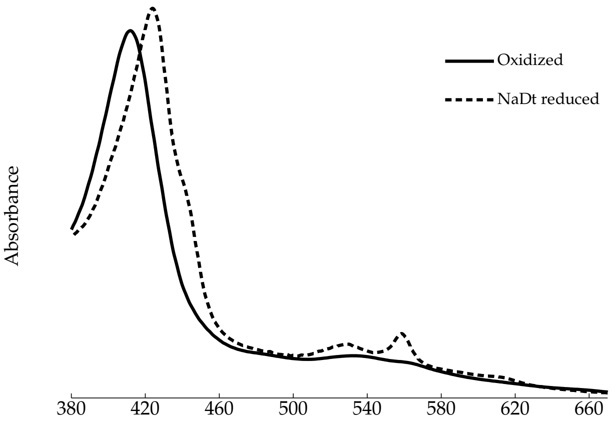

Figure 2.5: UV-Vis spectra of the oxidized and the reduced state of *ba*$_3$-type C*c*O. Shift in the dominant Soret peak (around 420 nm), as well as emerging Q-bands (around 500 to 600 nm), are a signature of the reduced enzyme.

Protein quantification using UV-Vis absorption The quantity of the purified protein can be calculated from the absorbance according to the linear correlation given by Beer-Lambert law, which defines absorbance, A, as:

$$A = \varepsilon c l \tag{2.13}$$

Where ε is characteristic extinction coefficient, l the path of light (i.e. the width of the measuring cuvette), and c the concentration of the measured sample in M.

Protein concentration of *ba*$_3$-C*c*O is determined by reducing the enzyme with excess sodium dithionite, and measuring the absorbance at 560 and 590 nm, and using the relationship that the absorbance difference $\Delta\varepsilon_{560-590}$ = 26 000 M^{-1}cm^{-1} [27].

2.5 Crystallization of *ba*$_3$-C*c*O

Protein crystals tend to be delicate and very sensitive to change of conditions, prone to radiation damage, and generally diffract weakly, retrieving diffraction patterns of much lower resolution. The high solvent content represents a trade-off between lowering the resolution of diffracted image, and native-like structure maintenance, where the protein remains surrounded by layers of water, retaining most of its enzymatic, ligand-binding, and spectroscopic characteristics compared to the fully solvated molecule. In most cases, crystalline enzymes are accessible for experimentation, as this arrangement allows for diffusion of chemical compounds, such as ions, ligands, substrates etc.

2.5.1 Principles of crystallization

For the crystallization to be successful, it is important to start with a sample of high purity and homogenity. Moreover, one has to achieve a crystallization condition where protein molecules "self-organize "in an orderly array via directional interactions which allow for a three-dimensional lattice formation.

Crystallization occurs in two steps: nucleation and growth. Once a crystal nucleus is formed, the crystal will continue to grow in given conditions. To induce the crystallization, a supersaturated state is required. In supersaturated state, the quantity of a macromolecule exceeds the solubility limit, yet remains present in the solution. This non-equilibrium, energetically in-favorable state, which is achieved in very defined, specific chemical and physical conditions, can move towards lower energy through formation and progression of a solid state. Crystallization is finished as the protein molecules from the solution are depleted, or an impurity occurs and the precipitate is formed, re-establishing the saturation limit. Still, if the solid phase does occur, the precipitation of protein is still energetically more favorable, and a stable nucleus of crystal is only formed within a narrow window of metastable conditions.

To find a favorable metastable condition, an extensive screening procedure is often required, and it consists rounds of crystallization trials exploring the range of protein and reagents' concentrations, volumes, pH, temperature etc. Nowadays, the performance of crystallization is further enhanced by employing easy-to-use screening kits and laboratory robotics, allowing for extensive exploration of crystallization condition landscape.

Nevertheless, to establish a good screening landscape, it is essential to understand the role of precipitation agents and their mechanism of promoting crystallization.

The role of precipitation agents The precipitation solution may contain one or more precipitation agents, such as salts, organic solvents or nonvolatile compounds, low-molecular weight polymers, and long-chain polymers, and therefore promote protein crystallization via different mechanisms.

For instance, salts induce crystallization by competitively binding the water molecules, thus dehydrating the protein and increasing its concentration. Salts which contain multivalent ions (especially anions) have a higher ionic strength in the solution, and therefore are the most efficient precipitants. Common examples include sulfates, phosphates and citrates. Additionally, the presence of salts modulates the pH of the solution, which alters the ionization state of surface amino-acid residues, and therefore affects the interaction with the solvent and the interaction with other protein molecules.

On the other hand, components like the long-chain polymers, i.e. polyethylene glycols, enforce the separation of the protein macromolecules from the solution by a volume exclusion effect. Due to their random orientation in solution, polymeric precipitants significantly restrict the available solvent space, which in turn desolvates the protein, pushing it towards the solid state.

2.5.2 Crystallization of membrane proteins

A variety of crystallization and screening methods have been developed and optimized predominantly for soluble cytoplasmic proteins.

Crystallizing membrane proteins is often percieved as more challenging, as their surface duality determines the strong preference for lipidic, predominantly hydrophobic medium [101]. Yet, significant efforts are made to allow for membrane protein crystallization, which can be performed *in surfo*, or via bilayer formation methods.

Lipid cubic phase (LCP) Lipidic cubic phase (LCP) is a membrane-mimetic matrix suitable for stabilization and crystallization of membrane proteins in lipidic environment [102].

LCP crystallization was introduced in 1996 by Landau and Rosenbusch [103], who obtained the first high-resolution structure of bacteriorhodopsin (bR). Other notable examples include a Nobel prize-awarded structure determination of $\beta 2$-adrenergic receptor–Gs protein complex [104], and channelrhodopsin, famous for its optogenetic properties [105].

Upon purification, the protein is preserved in a solution as a protein–detergent complex, in the form of a mixed micelle. The coupled-syringe mixing device [106] is employed to combine combining microlitre volumes of lipid with membrane-protein solution. The first and the most standard lipid to be used in protein crystallography is monoolein (MO) [107]. Its name indicates an 18-carbon (oleic) structure with one unsaturated (double) bond between C9 and C10. Nine carbons make up the so called "neck", and the other nine the "tail", thus it is also commonly denoted as 9.9 MAG.

Homogenization is achieved via repetitive, careful mixing until the protein solution is fully mixed into the lipid, and the phase becomes clear.

Once homogenized, a bicontinuous structure of aqueous phase and the lipid bilayer, is formed. This three-dimensional array is known as lipid cubic phase, and it is denoted as "*Pn3m*". Lipid cubic phase typically consists of 60 – 70 % (wt/wt) monoolein and 30 - 40 % water. The bilayer comprises approximately 32 Å in width, and the incident temperature-dependent water channel spans 40 Å in diameter at 40 °C (50 Å Ø at RT) [108]. Proteins, which are predominantly hydrophobic, diffuse laterally in the bilayer, while the hydrophilic, water-soluble components diffuse freely through the aqueous channels.

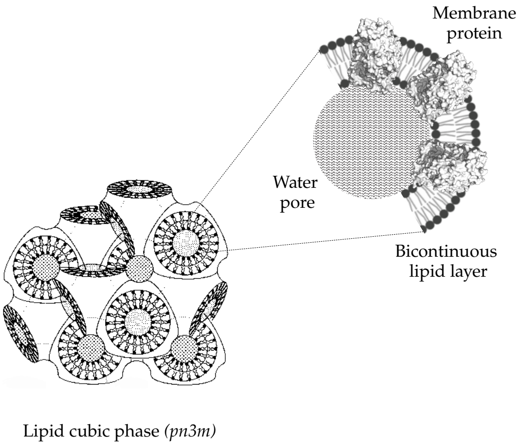

Figure 2.6: Membrane proteins in lipid cubic phase (LCP). *Pn3m* is shown as characteristic for crystallization of *ba*3-C*c*O.

To crystallize large membrane proteins or their complexes with soluble partners, the lipid membrane architecture can be altered by using specific precipitants, such as some non-volatile alcohols, low molecular weight PEGs, or some other polymers (for example, jeffamine M600, or 2-methyl-2,4-pentanediol (MPD)). This is commonly known as "swelling", and it results in transition from the cubic phase to sponge phase, often described as melted bicontinuous cubic phase. Sponge phase, or L3 phase, is characterized by the formation of larger water pores, allowing them to accommodate membrane proteins with large extra- and/or intracellular domains [109].

Chapter 3

Results and Discussion

3.1 Paper I: Time-resolved serial crystallography to track the dynamics of carbon monoxide in the active site of cytochrome *c* oxidase

Among the large number of structures of C*c*O obtained using crystallography, structures of bovine *aa*$_3$-type C*c*O with carbon monoxide (CO) bound and dissociated from the active site [110,111], as well as the structure of time-resolved reaction intermediate of C*c*O [112], have been available. The interest in binding and dissociation of CO molecule originates from the similarity of these mechanisms to those of its native ligand, O_2. It is, therefore, assumed that CO initiates the same conformational changes upon binding. Intrestingly, previous study of CO photo-dissociation in bovine *aa*$_3$-type C*c*O showed that binding of CO to Cu_B occurs on a femtosecond timescale, and its release on microsecond time scale, followed by re-initiation of CO-heme *a*$_3$ co-ordination within approximately 10 ms.

The work reported in this paper is a TR-SFX study of structural events following the photodissociation of carbon monoxide (CO) from a reduced CO-bound *ba*$_3$-type C*c*O. In a reduced CO-bound enzyme, the CO molecule is co-ordinated by the iron (Fe(II)) of the heme *a*$_3$ in the binuclear Cu_B-heme *a*$_3$ active site. Diffraction data collected in this experiment revealed the change in CO coordination in the active site 2 ms after flash-photolysis, where the co-ordination bond of CO to Cu_B is established, accompanied by the transient appearance of a water molecule within the active site. The presence of additional water in *ba*$_3$-C*c*O is likely stabilizing and prolonging the lifetime of the Cu$_B$-CO bound state, thus highlighting the difference in structural response upon CO photo-dissociation between *ba*$_3$- and *aa*$_3$-type enzyme.

3.1.1 TR-SFX experiment at SACLA

TR-SFX experiment was performed at BL3 beamline at SACLA, Riken, Japan. The reduced-CO bound *ba*$_3$-C*c*O crystal sample was prepared at University of Gothenburg according to the protocol described in [113], where the anaerobically grown microcrystals were reduced by 1 mM sodium dithionite after crystal formation, with no change in crystal morphology or anomaly detected. The reduction and CO-binding to heme *a*$_3$ was validated by UV-Vis spectrophotometry using a CaF_2 glass cell, which allows for anaerobic conditions to be maintained. Sample modulation procedures, such as CO gas top-up, sample homogenization, and the addition of monoolein, as well as loading and assembly of the LCP sample injector, were performed in temperature-controled oxygen-free conditions provided by anaerobic glove box on-site, before the experiment. The maintenence of anaerobic condition was accessed via oxygen indicator tablet and monitored during packing and transportation of a grease-sealed injector in a gas-tight, heat-sealed plastic bag. Gas-tight injector was mounted in a helium chamber that is part of the Diverse Application Platform for Hard X-ray diffraction In SACLA (DAPHNIS).

Diffraction data were collected at 7.5 keV with an X-ray repetition rate of 30 Hz and a pulse duration of <10 fs and the energy of 95 µJ was estimated the sample position, amounting to the average radiation dose of 7 MGy per crystal, calculated using the program *RADDOSE-XFEL* [114]. CO dissociation from the reduced CO-bound enzyme was induced by 5 ns laser (λ = 532 nm) pulse illumination of 200 µJ per pulse, focussed on 80 µm spot, with a 2 ms (Δt) time-delay between the laser pulse and the X-ray probe. Diffraction images were collected using an eight-sensor module CCD detector. The number of hits for each dataset (*dark1*, *dark2*, and *light*) was accessed during online processing using *Cheetah*. Data containing diffraction spots were indexed and merged without partiality corrections in *CrystFEL*.

3.1.2 Map calculation and refinement

The dark state and the laser-on structure were solved by molecular replacement in *Phaser*, using the room-temperature SFX structure of oxidized *ba*3-type C*c*O (PDB ID: 5NDC) as a search model. Maps are further refined to a resolution of 2.0 Å in *Refmac*, where the final $R_{\text{work}}/R_{\text{free}}$ values were 20.1 % / 22.5 % for the CO-bound dark state structure. Model building and visualization of refined maps was performed in *Coot*.

Isomorphous $\mathbf{F_o}$(2 ms)−$\mathbf{F_o}$ difference electron density map An isomorphous F_o(2 ms)−F_o(dark) difference Fourier electron density map was calculated at 2.0 Å resolution using the observed structure factor amplitudes and phases from the CO-bound dark state model (Figure 3.1). The observed differences indicated there was a shift present downwards of both Cu_B and Fe. In addition, a small negative feature close to the CO was observed.

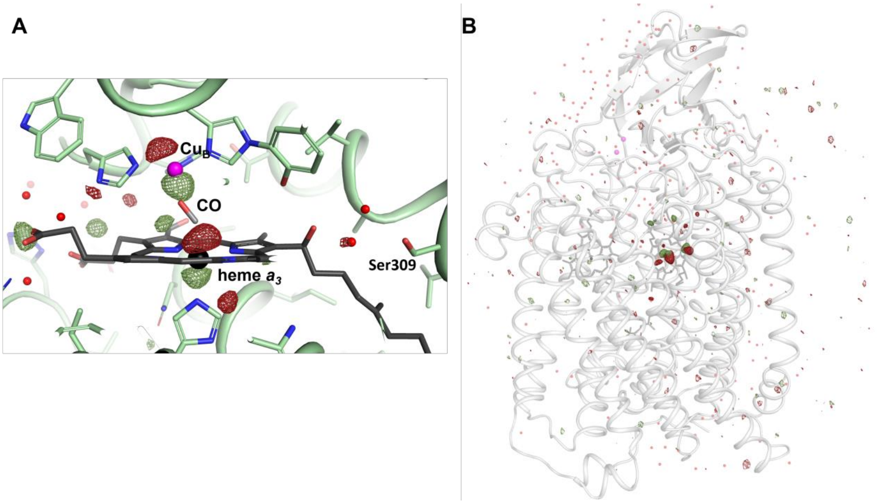

Figure 3.1: Photoinduced disociation of CO from CO-bound active site of *ba*$_3$-type C*c*O. F_{obs}(2 ms)$-F_{obs}$(dark) isomorphous difference Fourier electron density map displaying differences (positive: dark red, negative: dark green; 3.5σ) between the dark (reduced CO-bound) state and the activated (light) state in the the heme a_3–Cu$_b$ active site (A) and protein backbone (B).

Initial structural model of the 2 ms photoactivated state using partial occupancy refinment A structural model of the 2 ms photoactivated state using extrapolated structure factor amplitudes estimated an occupancy of 30 % for the photoactivated state and displayed an approximate orientation of the CO molecule in the active site. A partial-occupancy refinement with additional restraints was performed in *Phenix*, confirming the estimate of a photoactivated state fraction of 30 %. and retrieving the R_{work}/R_{free} values of 18.7 % / 21.3 %.

Most importantly, partial occupancy refined model displays the new conformation of CO, where it is ligated to Cu$_B$. Moreover, the model reveals ordering of Wat188 and the electron density of the new water molecule (Wat197) emerging in the active site, where it creates a link between the CO and Tyr133A.

Updated model of the 2 ms photoactivated state using extrapolated structure factors As an alternative approach to determine the structural response upon light activation, the extrapolated structure factors were calculated through the program package *Xtrapol8* with the Fgenick method [82]. Using *Xtrapol8*, the occupancy was determined to 31 % compared to the previously determined occupancy of 30 % . The structure factors extrapolated to 100 % occupancy were used to refine the structure corresponding to the photoactivated state with *Refmac5*, retrieving a good quality electron density map validated by stable R-factors.

The resulting structure confirms the movement of CO towards $\mathrm{Cu_B}$ and the appearance of the new water molecule. However, the refined position of the CO molecule is slightly shifted away from the two water molecules and does not overlap completely with that from partial occupancy refinement, although the exact orientation of the CO molecule was difficult to determine in either of the refined maps. Interestingly, the distance between Fe and $\mathrm{Cu_B}$ appears to be longer (5.1 Å) than the distance observed in the initial model (4.9 Å).

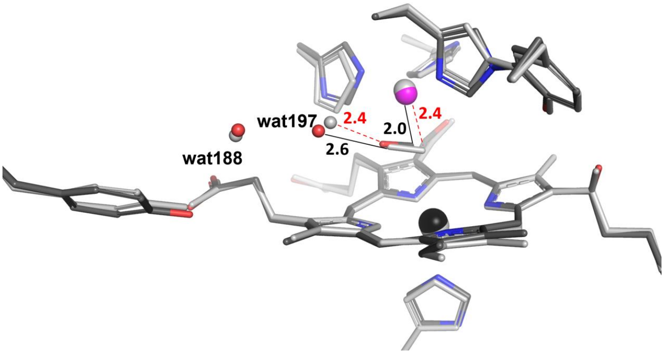

Figure 3.2: Activated-state structure of *ba*$_3$-type C*c*O. Comparison between activated-state structure from partial occupancy refinement (dark grey) with structure refined using extrapolated structure factors (light grey) reveals changed distances between the CO molecule (red stick) and Cu$_B$ (magenta) as the changed distance to wat197 (red sphere).

3.1.3 Conclusions and outlook

Results of this study reveal the transient Cu$_B$–CO state of *ba*$_3$-type C*c*O, stabilized by the ordering of a new water molecule in the active site. This observation could, therefore, explain the longer lifetime of Cu$_B$– CO state in *ba*$_3$-type compared to *aa*$_3$-type C*c*Os.

This experiment represents a milestone in developing a pump-probe SFX setup of oxygen reaction of C*c*O. High-affinity binding of CO to the active site and its dissociation of upon the laser illumination, followed by the return to the active site, can be used as a mimic of oxygen binding dynamics. The time recorded for the re-binding of CO is a useful indication of the time required for oxygen binding to the reduced active site within a crystal in a lipid medium. In addition, sample preparation protocol allows for a successful chemical (i.e. protein reduction) and physical (crystal packing, sample mixing, injector loading) manipulation of the crystal sample, as well as a UV-Vis spectroscopic validation of the CcO redox states in LCP.

3.2 Paper II: Structural changes in cytochrome *c* oxidase following the reduction of dioxygen to water

A ubiquitous mechanism of energy transduction in living cells is that energy harvested from light or from chemical energy is used to transport protons “up-hill” across an energy transducing biological membrane. The resulting proton gradient is primarily harvested by ATP-synthase in order to regenerate ATP, which is used as a universal energy-preserving molecule throughout living cells. As such, proton pumping is the pillar of energy transduction in organisms.

Time-resolved serial femtosecond crystallography (TR-SFX) was used [115] to study light-driven structural changes on a femtosecond to millisecond scale in bacteriorhodopsin, a light sensitive membrane protein and one of the best understood proton pumps. We hereby employ TR-SFX to study how the electron transfer in cytochrome *c* oxidase is coupled to proton pumping. Because C*c*O is a redox-sensitive integral membrane protein, it is essential to collect serial crystallography data using XFEL radiation in order to avoids the effects of X-ray induced reduction of microcrystals [58], and deliver high X-ray fluence through microcrystals.

Several XFEL based studies of cytochrome *c* oxidase have been published previously [110, 116], including a serial crystallography structure of the oxidized state of a *T. thermophilus* *ba*$_3$-type C*c*O published by our group [113]. Apart from providing the damage-free room temperature reference structure, this work set some of the standards in sample preparation in order to obtain sucessfully diffracting batches of microcrystals for SFX experiments. What followed was a TR-SFX study of the structural response of *ba*$_3$-C*c*O upon flash-photolysis of carbon monoxide from the reduced active site (Paper I), which provided a structural explanation to the oxygen binding dynamics and exceptionally high oxygen affinity of the enzyme. Moreover, a time-resolved SFX structure revealed the movement of CO closer to the Cu$_B$ and further from the heme *a*$_3$ Fe, demonstrating that the data quality is sufficient to resolve fine structural details using TR-SFX.

In this experiment, we tracked structural changes at the active site of *ba*3-type cytochrome *c* oxidase upon photoinitiated release of oxygen molecule from cobalt-based cage compound. The release of dioxygen upon UV laser illumination was validated by in-house time-resolved UV-Vis spectroscopy set-up, in both solution and microcrystalline form, where activation of the caged compound by a single 355 nm UV-laser flash resulted with the release of oxygen.

The most challenging aspect of this experiment was to ensure the compatibility of the caged oxygen compound with the chemical environment of the C*c*O microcrystal precipitation solution and the reducing agent. In preparations for the previous TR-SFX experiment, it was observed that the contribution from sodium dithionite (NaDt) results in premature disintegration of caged compound and the uncontrolled release of oxygen. Therefore, reducing C*c*O using milder reducing agents, namely DTT and DTBA, was explored for the purpose of this study.

Events at 10 ms upon UV illumination, as well as was recurring structural changes upon enzyme reduction are featured in this work. In addition, a a high-resolution structure of the resting oxidized state of *ba*3-C*c*O is reported, revealing a chloride ligand bound in the active site, confirmed by anomalous X-ray diffraction map.

This research contributes towards our long-term goal to use time-resolved serial femtosecond crystallography at XFELs for a comprehensive structural study of cytochrome *c* oxidase activity.

3.2.1 Preparation of microcrystal sample

Protein production and crystallization Protein was produced and purified via standard protocols described in 2.4. Crystallization in LCP was conducted in rounds, with screening for optimal protein concentration and v/v PEG400. Crystals of 20 - 25 µm averge size were attained from 12 - 15 mg/µl *ba*3-C*c*O solution mixed with the liquid monoolein in 2 : 3 ratio, extruded as 10 - 15 µl LCP threads into the precipitation solution containing 36.5 - 38.5 % PEG400.

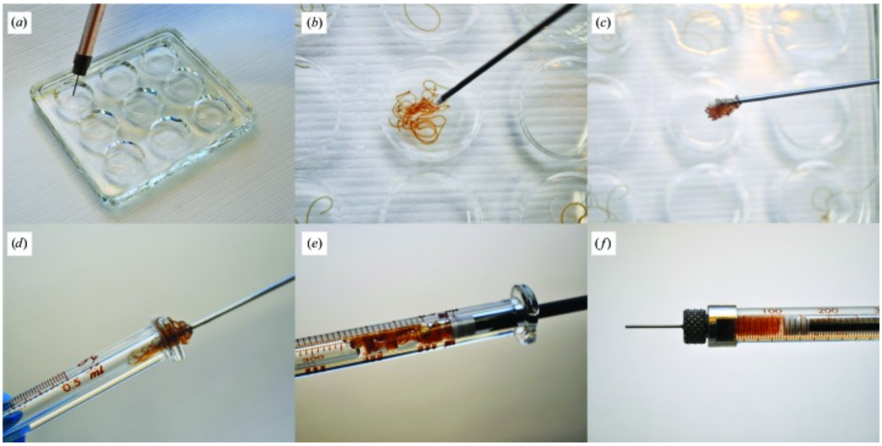

Figure 3.3: Well-based crystallization protocol. 10-15 µl LCP threads are extruded into the precipitation solution containing 36.5 - 38.5 % PEG400. Microcrystals are collected by pooling several LCP strings into one well with the help of a plunger. Using this method, LCP from the wells of several glass plates can be transferred into the same syringe. *Taken from Andersson et al.(2019)* [117]

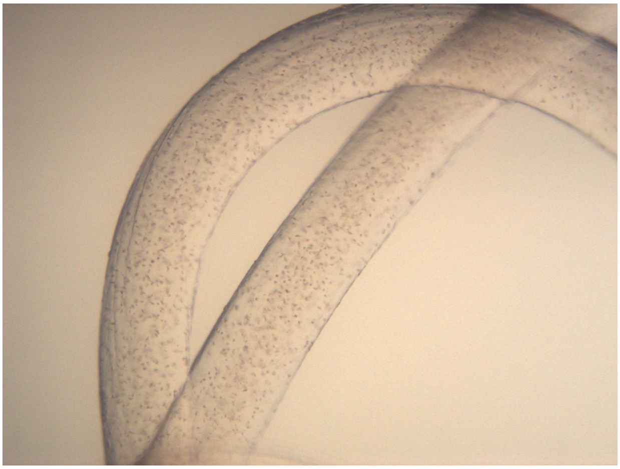

Figure 3.4: LCP microcystals of *ba*$_3$-C*c*O.

Re-constitution of chemicals in LCP To ensure the compatibility of phases and the homogenous mixing, all of the components were reconstituted in lipid cubic phase (LCP).

To reconstitute each sample component in LCP, the aqueous solution was mixed with 9.9 MAG in 2 : 3 ratio in Hamilton syringe coupled mixer, until the phase appeared no longer turbid.

Chemical reduction treatment with DTT and mixing with caged oxygen compound A larger volume of crystal sample (e.g. 200 µl) was treated with "oxygen scrub" (consisted of a solution of glucose, glucose oxidase, and catalase, reconstituted in LCP) to remove the residual oxygen before reducing the sample. Oxygen-free sample was then treated with 170 mM DTT to reduce the C*c*O crystals before mixing with cage compound.

Solid oxygen cage powder was disolved to maximum solubility (30 mM). The stock cage solution was reconstituted in LCP (12 mM) as described above. During the preparation, the cage compound solution and LCP were covered with aluminum foil to minimize the light exposure.

The final sample was prepared by mixing 70 µl of DTT-reduced crystal sample with 20 µl of oxygen cage LCP (2.4 mM), and adding 10 µl of monoolein to optimize the consistency. Arizona sample injector [63] was loaded with: oxygen-scrub LCP, followed by 100 µl of sample, and then additional 5 µl of oxygen-scrub LCP, to ensure the oxygen-free conditions in case of oxygen leak during the injector transportation.

Chemical reduction treatment with DTBA A new reducing agent was explored and used for chemical reduction of ba_3-C*c*O microcrystals for SFX data collection at LCLS.

Whereas DTT and DTBA have very similar mid-point potentials, due to the lower pK_a, DTBA reduces ba_3-C*c*O more rapidly than DTT at acidic pH.

The preparation of the sample resambles the one described for DTT. Protocols differ in the step of reconstitution of the reducing agent, where DTBA is dissolved in 3 M NaOH.

3.2.2 SFX and TR-SFX at SwissFEL

SFX and TR-SFX data collection SFX diffraction data of resting oxidized *ba*$_3$-C*c*O crystals, crystals treated with DTT, and crystals treated with DTT with cage compound added, were collected at Alvra beamline at SwissFEL facility. The microcrystals in LCP were jetted using Arizona LCP injector [63], and probed by 70 fs X-ray pulses of 12 keV (about 700 µJ) at the front end, attenuated to 20 % at the sample position, focused to 6x6 µm^2 FWHM.

Sample of DTT-treated crystals mixed with caged oxygen compound was used to perform time-resolved (TR)-SFX, where the running LCP jet was illuminated by laser diod of λ = 355 nm focused to 40 x 36 µm^2 FWHM in time delays $\Delta(t)$ of 100 s, 1 ms, 10 ms and 30 ms. Initial energy was set to 24 µJ per pulse but it was tuned down to 12, 6, and 5 µJ/pulse since the loss of diffraction was observed. Diffraction data collection for 100 s and 1 ms timepoint was recorded as alternating dark and light images, where "light" is the image collected upon laser excitation, and "dark1" and "dark2" as a first and second image with no laser excitation, respectively. With it being further separated from the preceeding light image, "dark2" is often taken as the "real" dark used to track time-dependent changes. Data collection protocol for 10 ms and 30 ms timepoint did not include "dark1" or "dark2" but a continuous collection of "light" images instead.

All diffraction images were recorded on Jungfrau 4Mpix detector.

Data processing Peak finding, indexing, and merging of diffraction data were performed in *CrystFEL* [65]. Indexing of diffraction data was performed on full dataset with no prior data reduction, with geometry optimization for detector shift per each sample acquisition run.

Indexing of SFX data collected at SwissFEL was performed by *indexamajig* using the input cell parameters with several indexing programs (*xgandalf-latt-cell, asdf-latt-cell, dirax-latt-cell, mosflm-latt-cell*) in a consecutive manner (*-no-multi*).

Data scaling and merging was performed using *partilator* with 3 iterations and a *unity* model, with $2/m_{uab}$ as a chosen point group.

The final resolution of resting oxidized *ba*3-C*c*O, DTT-reduced *ba*3-C*c*O, and DTT-reduced *ba*3-C*c*O microcrystals mixed with caged oxygen compoud was determined based on figures of merits (R_{split}, $CC_{1/2}$) retrieved by *check_hkl* and *compare_hkl*. Resolution cutoff of aforementioned structures was made at 1.7, 1.8, and 1.9 Å, respectively.

3.2.3 SFX and TR-SFX at LCLS

SFX data collection In a separate, follow up experiment, SFX diffraction data of *ba*3-C*c*O microcrystals treated with DTBA were collected at MFX beamline at LCLS in SASE operating mode, using 9.5 keV X-ray pulses of 30 fs duration at the 120 Hz repetition rate, focused to 4 x 4 µm FWHM spot size. Diffraction data was recorded on Rayonix detector.

TR-SFX Time-resolved collection attempted to capture structural changes at $\Delta(t)$ = 3.3 and 8.9 ms upon light illumination. However, due to the number of difficulties with the TR-SFX setup, the data is not presented in the scope of this work.

Data processing SFX data collected at LCLS was processed in BTX (stands for "*BeamTime with X-rays*"), a user environment containing miscellaneous functions for aiding analysis during LCLS experiment. Peak finding, indexing, and merging of diffraction data, as well as geometry optimization, were performed via standardized pipeline. Indexing was performed by programs *mosflm* and *xds*, simultaneously (*multi=True*), with standard input cell parameters for *ba*3-C*c*O. Data scaling and merging was performed using *partilator* with 1 iteration and a *unity* model, with *2/m$_{uab}$* as a chosen point group, and was followed up by statistical analysis as described above. For DTBA reduced *ba*$_3$-C*c*O, the resolution cutoff based on values of R_{split} and CC^* was determined as 2.35 Å.

3.2.4 Electron density map calculation and refinement

Full reflection lists of each dataset was converted to .mtz file format, and processed further using programs of *CCP4* ([59]) software suit. Structural amplitude factors were calculated from intensities using *Truncate*. Molecular replacement was carried out in *Phaser* using previously published resting oxidized room-temperature SFX structure of *ba*$_3$-C*c*O (PDB ID: 5NDC). Map refinment was performed in *Refmac5*, with pipeline consisted of one-time rigid body refinment procedure, consisted 20 cycles of maximum likelihood rigid body refinment, followed by rounds of restrained refinement (10 cycles of TLS refinment [118] with 10 cycles maximum likelihood restrained refinement per round) and model building in *Coot* [119]. The plausability of the fits was validated by $\mathrm{R_{work}/R_{free}}$ ratio.

Difference electron density maps TR-SFX results of *ba*$_3$-C*c*O reaction upon photoinduced oxygen release were accessed by difference density maps. Difference electron density maps were calculated in *Phenix* [120] by subtracting structure factor amplitudes of absolute dark data ("*DTT + cage*") collected with no laser exposure from intensities of diffraction data upon laser illumination with time delays $\Delta(t)$ of 100 s, 1 ms, 10 ms and 30 ms, respectively, using phases of the fully refined dark state structure.

3.2.5 Statistical computational approaches in SFX data analysis

Quantification of Polder residual electron density features with time To quantify the evolution of electron density changes with time under various experimental conditions, a bootstrapping algorithm [121, 122] was employed to extract 100 resampled serial crystallography datasets, where each dataset contained 20 000 integrated diffraction images. Resampling of crystallographic structures was performed for each experimental condition. For every 100 resampled structures, Polder omit maps were calculated.

Internal distance matrix analysis To extract both the mean internal displacements and their standard deviation, internal distance matrix analysis [123] is performed for each set of 100 refined crystallographic structures. Using the internal distance matrix to analyse protein structures allows for an easy, unbiased comparisons of large number of structures.

3.2.6 Novel structural phenomena in SFX structures of resting oxidized and chemically reduced *ba*$_3$-C*c*O

SFX structure of resting oxidized *ba*$_3$-C*c*O Electron density map of resting oxidized state displayed two striking spherical density features ligating Cu_B and the farnesyl oxygen of heme *a*$_3$, which were notably stronger than the electron density associated with ordered water molecules, suggesting a different type of ligand than previously modeled water (hydroxide) molecule. Given the crystallization condition of high sodium chloride concentration (1.4 M) and supporting spectroscopical evidence previously obtained for *ba*$_3$-C*c*O in solution [124], a chloride ion is proposed and modeled as a ligating species, resulting in an improved fit compared to modeling water. These findings are in agreement with X-ray spectroscopy, EPR spectroscopy, and other biophysical studies, which have suggested that Cl - may be a ligand to Cu_B [36, 124–127].

Anomalous X-ray diffraction structure of the resting oxidized state To strengthen this hypothesis, anomalous X-ray diffraction experiment was performed at Biomax beamline at MAX IV. Anomalous diffraction signal of a single crystal cooled to cryogenic temperature recorded at 6.2 keV revealed Bijvoet difference electron density features on all Cu and Fe atoms of the cofactors, peaks on the sulphur atoms of the protein's methionine and cystine residues, and similar strength anomalous difference electron density peaks on the Cu_B and farnesyl oxygen ligands. Given the high concentration of NaCl (1.4 M) in crystallization condition and the reach of the method at the proposed energy of the beam, the signal of the active site ligand close to Cu_B, as well as the density near the farnesyl oxygen, are prescribed to chloride ions.

SFX structure of DTT-reduced *ba*$_3$-C*c*O The strong residual positive density indicating a Cu_B co-ordinating ligand in the active site of the reduced enzyme was observed. The feasible most fit was obtained by modelling a chloride ion.

The residual density indicating a bound ligand is contrast with previous findings and proposed mechanism of catalyitic reaction, where cytochrome *c* oxidase in its reduced state displays an empty acitve site. Moreover, UV-Vis absorption spectra obtained prior to the SFX experiment suggested that both heme *b* and heme a_3 in microcrystal ba_3-C*c*O sample obtained at ph 5.3 and 1.4 M HCL can be reduced by more than 50 % but less than 100 %, once enzyme turnover within microcrystals has entirely consumed any residual oxygen. However, difficulties in obtaining feasible UV-Vis spectra of DTT-reduced microcrystals on-site led to inability to fully validate the reduced state across samples.

SFX structure of DTBA-reduced *ba*$_3$-C*c*O To solve the structure of reduced enzyme where a spectral evidence of the reduced state is available, DTBA was explored as a reducing agent. With similar midpoint potential but lower pK_a than DTT, it was observed deprotonated form of DTBA reduces detergent solubilized C*c*O samples two to three times faster. Diffraction data collected at LCLS upon 60 to 90 min incubation with DTBA revealed no significant electron density in the active site, demonstrating that theoretically predicted empty active site is correct.

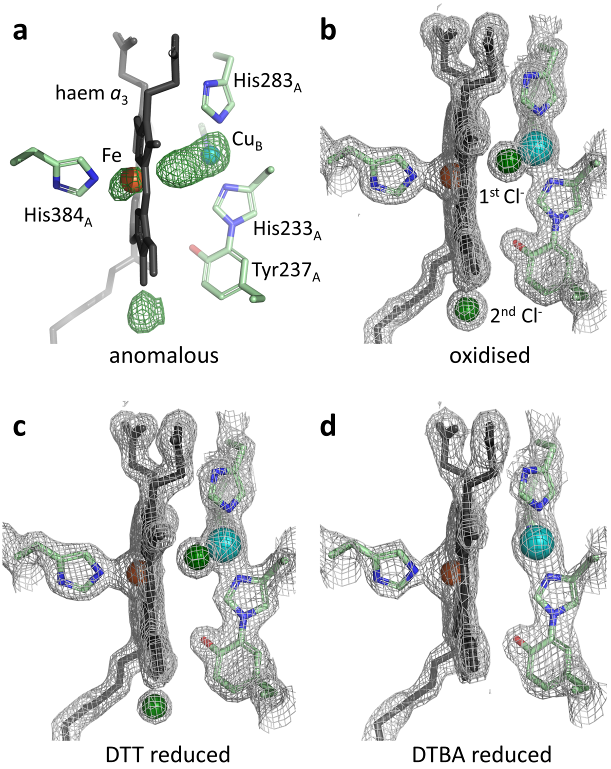

Figure 3.5: Electron density at the binuclear centre of *ba*$_3$-C*c*O under different redox conditions. 1.7 Å room-temperature SFX structure of resting oxidized state (b), supported by anomalous X-ray diffraction data (a) reveals a chloride ion in the active site bound to Cu$_b$, as well as near heme a_3 at the 2nd Cl$^-$ position. Structural differences upon the reduction of the C*c*O were observed when DTT (c) and DTBA (d) were used, where DTBA treatment produces an empty active site.

Changes upon DTT treatment revealed by Polder analysis Data obtained by Polder analysis reports the loss of chloride-associated electron density upon reduction by DTT. A similar trend is observed for the 2nd Cl^- anion ligating the farnesyl oxygen of heme a_3, where a more striking loss of 33% of the electron density was observed. In the oxidized conformation, this chloride anion sits near the binuclear centre at the end of the K-analogue proton-transport channel, essential for transport of both substrate and pumped protons. Displacement of this chloride induced changes in architecture of nearby water molecules, as well as the H-bonding to the aminoacids in the close proximity.

Interestingly, electron density arises for a water molecule near Tyr133A (Wat159) that is entirely absent in the oxidized structure [87, 113]. The H-bond network forming in the presence of this water could potentially increase the affinity of the active site to bind dioxygen. Comparison of the amplitude of the residual Polder electron density associated with this water molecule averaged over all DTT reduced structures, with that observed for the fully-reduced DTBA structure, suggests that DTT reduced approximately 65% of enzyme molecules in LCP microcrystals.

Finally, internal distance matrix analysis revealed global conformational changes based on the most significant backbone displacements upon DTT treatment, showing that all DTT-treated samples differ to a much larger extent from the untreated oxidized structure than they differ between themselves. Specifically, the largest motions are associated with the N-side of TM10 and are clearly visible in all $F_{obs} - F_{obs}$ difference Fourier electron density maps calculated for DTT-treated microcrystals versus the oxidized microcrystals.

Understanding of the reduction mechanism Observations upon reduction of microcrystals by DTBA indicates that fully reduced the $Cu_B(I)$ is not ligated by Cl^-. Still, in the system where less than 100% of population of the enzyme was reduced, i.e. upon DTT treatment, the loss of electron density might be an unreliable proxy for estimating the extent of reduction.

It is, therefore, argued, whether the reduction mechanism can be understood as the linear sum of the electron density for the oxidized and the reduced structures, or as a complex kinetic behaviour within crystals, where closely packed protein molecules exchange electrons in a constant redox dynamics within the crystal. In the latter case, the strong residual density at Cu_B in DTT reduced sample, corresponding to chloride, could be explained by assuming the rate needed for dissociated Cl^- to diffuse from the protein's active site, is slower than the rate at which C*c*O molecules exchange electrons between each other. Still, kinetic arguments would need to estimate the actual threshold of reduced C*c*O molecules required for the loss of electron density at Cu_B to be observed.

The geometry argument should as well be considered. Generally, the closed shell d10 Cu(I) ions have the most prevailing coordination of four with tetrahedral geometry [128], which could explain the fourth ligand in Cu(I) state. Still, Cu_B(I) co-ordination geometry across literature is well established by several studies using reducing agents that fully-reduce C*c*O crystals, for which Cu_B is observed to be co-ordinated by thee nitrogen atoms (one of each of the three surrounding histidines) [129].

Nevertheless, the model in which a chloride ligand remain bound to the active site for tens of minutes upon reduction, has not been experimentally obtained in previous studies. In contrast, it was observed the chloride is released immediately upon reduction of bovine aa_3-C*c*O [126].

3.2.7 Time-resolved structural changes upon photoinduced reaction of dioxygen

100 us and 1 ms timepoints As a result of low quantum efficiency yield of caged oxygen compound, its time-dependent decay, and slow rate of diffusion in the crystals, no significant changes above 3.5 σ cutoff were observed upon short laser exposure for 100 us and 1 ms timepoints.

Observations and interpretation of structural changes upon dioxygen reaction at 10 ms and 30 ms timepoints Difference electron density maps of diffraction data collected with longer laser exposure times of 10 ms and 30 ms, respectivelly, display significant negative difference electron density features on chloride ions ligating both Cu_B (4.6 σ for 10 ms, 4.7 σ for 30 ms) and farnesyl oxygen (7.4 σ for 10 ms, 5.8 σ for 30 ms), as a result of a successful release and diffusion of dioxygen through the LCP, followed by the displacement of the active site chloride due to a steric clash. In addition, Polder map analysis revealed that the loss of electron density associated with the active site Cl^- ligand upon DTT reduction, proceeds further as photocage is added to DTT reduced microcrystals, and is observed to an even larger extent upon UV illumination. As anticipated from the difference Fourier electron density maps, the strongest change in electron density associated with the Cu_B Cl^- ligand occurred for $\Delta(t)$ = 10 ms and corresponds to the loss of 60% of the original electron density at this site. Weaker difference electron density features observed at $\Delta(t)$ = 30 ms imply that the large fraction of displaced Cl^- has rebound to Cu_B. This observation, however, contrasts with results from mixing studies using microcrystals of reduced bovine C*c*O [112], and proposed events at this timescale.

A similar trend is observed for the 2nd Cl^- anion ligating the farnesyl oxygen of heme a_3, but larger changes in electron density arise at this site, with 33% loss of the electron density upon DTT reduction, intensifying with the addition of caged oxygen compound. Moreover, the strong chloride density is replaced by emerging new water molecule at the nearby position. Even though the timescale of this event is not elucidated, it can be argued that the rebinding of Cl^- to Cu_B is to occur more rapidly than its rebinding to the farnesyl oxygen.

Still, it is not possible to neglect the contribution of dioxygen released by spontaneous decay of sensitive photocage, which in turn yields a mixed population and a slow enzyme turnover prior to light illumination, as observed when comparing structures of DTT reduced enzyme before and after addition of caged oxygen compound. Therefore, a quasi-equilibrium is proposed, where the rate at which the enzyme is reduced by the reducing agent is balanced with the rate at which it is oxidized by residual oxygen, until all oxygen is consumed. We hypothesise that this enzymatic turnover within microcrystals leads to conformation changes that can be associated with transition from relaxed O-state to the activated O_H-state of the enzyme, which displays proton-pumping activity.

Changes in the Cu_B-Fe_{a_3} distance Structural refinement against 100 bootstrap resampled datasets revealed a statistically significant increased distance between Cu_B-Fe_{a_3} at $\Delta(t)$ = 10 ms, relative to the oxidized structure. Moreover, a metal-to-metal separation observed 10 ms upon photoinitiation, appears to be more statistically significant than the one induced by DTT reduction or DTBA reduction. It is proposed that O_2 displacement of the Cu_B Cl^- ligand lowers the Cu_B coordination number from four to three, leading to increasing distance between the metal centres due to the more negatively charged copper.

Functional interpretation of oxygen-induced changes The functional interpretation of farnesyl chloride displacement could be related to the regulation of the proton transport via K-pathway analogue, where a high proton affinity (deprotonated) state of Tyr244A is disfavoured in the presence of chloride anion. Chloride ion binding site, populated due to the high chloride population, highlights a possible blockage site, which becomes occupied as enzyme adopts the inactive, slow form. Chloride displacement upon enzyme turnover induces changes in H-bonding network and toggle of Tyr244A side chain, which might play an important role in proton transport to the active site.

Interestingly, water (Wat159) with the weak H-bond contact to Tyr133A and backbone carbonyl of Gly233A is emerging in reduced structures, but is absent in our and previously reported oxidized structures. Functional impact of Wat159 ordering upon enzyme reduction could be significant, as it would stabilize the deprotonated form of Tyr133A, allowing a proton to be relayed towards the protein's surface. A loss of density asocciated with Wat159 observed at $\Delta(t) = 10$ ms and 30 ms implies that oxidation of the enzyme perturbs the H-bond network that connects the binuclear center and the P-side of the membarne. Nevertheless, this water provides a connection to propionate 1 of heme a_3, which is, along with propionate 2 and Asp371A, suggested to be the proton loading site, playing role in proton release to periplasm. Even though no perturbation of either propionates or Asp371A can be observed in our SFX data, the statistical analysis of electron density peaks reveals a slight disorder of two waters in a highly-conserved water cluster upon light illumination at 10 and 30 ms, indicating a higher temporal resolution could give more structural insight to the role of this region in proton transport.

In addition, the placement of the water close to Tyr237A and farnesyl oxygen of heme a_3, is observed to drift depending on the chemical treatment, changing its relative distance to Tyr237A in the analyzed oxidized and reduced structures. The ordering of this water at $\Delta t = 10$ could potentially stabilize the deprotonated form of Tyr237A, allowing it to donate protons taken up through the K-pathway analogue channel into the active site, as dioxygen is reduced to two molecules of water.

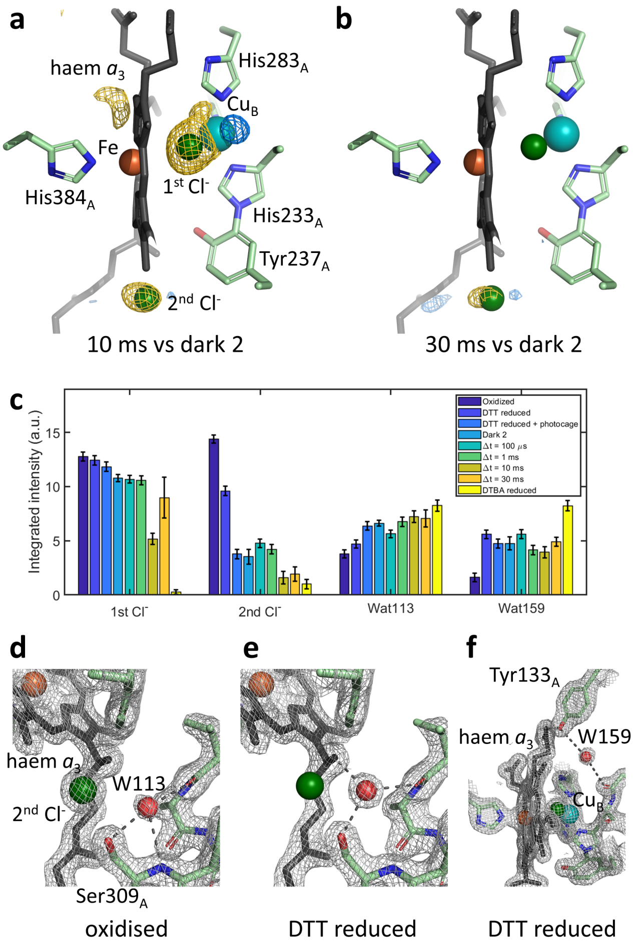

Figure 3.6: Conformational changes induced in *ba*$_3$-*Cc*O F_{obs}(light)$-F_{obs}$(dark) isomorphous difference Fourier electron density maps (a, b) illustrate electron density changes (blue - positive, yellow - negative) at the binuclear centre upon dioxygen release at $\Delta(t)$ = 10ms and 30 ms, respectively. 2$F_{obs}-F_{calc}$ electron density maps (d - f) highlight conformational changes at the N- (d, e) and P-side (f) of binuclear centre upon DTT treatment. Results of Polder electron density map quantification are displayed in (c). Bars show the mean of 100 maps calculated from 100 resampled datasets.

3.2.8 Conclusions and outlook

SFX diffraction data of resting oxidized *ba*$_3$-C*c*O collected at SwissFEL and resolved to 1.7 Å, supported by findings of the anomalous X-ray diffraction experiment at MAX IV, reveals the binding of chloride ion in the active site, as well as in the close proximity of the farnesyl chain of heme *a*$_3$, as a consequence of a 1.4 M NaCl in crystallization condition.

Two different reducing agents, DTT and DTBA, were employed to obtain reduced samples to be used in time-resolved studies. SFX structure of microcrystals treated with DTT displayed unexpected electron density ligating Cu$_B$ in the active site, while the structure obtained upon DTBA treatment was in agreement with previously proposed empty active site of the reduced C*c*O. Kinetic argument is needed to explain a potentially complex kinetic behavior of C*c*O molecules in microcrystals in the presence of the reducing agent.

TR-SFX data recorded 10 ms upon light-induced dioxygen release show displacement of the chloride ligand to Cu$_B$ as a result of dioxygen diffusion to the active site, while diffraction data at 30 ms timepoint demonstrates that the re-binding of Cl^- to Cu$_B$ occurs within a few tens of milliseconds. Transient ordering of water molecules and changes in H-bond network between observed structures allowed us to speculate the potential functional roles of a few water molecules and aminoacids. Moreover, the changes in Cl^- occupancy at the farnesyl oxygen site gave potential explanation of K-pathway analogue gating mechanism and prevention of the proton leakage.

Structural changes interpreted as a consequence of a dioxygen reaction upon laser illumination can be countered on a few points, mainly with regards to possible inconsistencies in sample preparations, and lack of experimental evidence. First, the efficiency in of DTT as a reducing agent in microcystals, mainly due to the observed inconsistencies in the time scale of reduction, has shown to be suboptimal. In addition, the incubation time of microcrystals with DTT varied between syringes due to the changing dynamics of the SFX experiment at SwissFEL, leading to unusually long incubation time of one larger sample syringe, which was then coincidentally used to collect 10 ms timepoint diffraction data. Lastly, difficulties in obtaining feasible UV-Vis spectra of DTT-reduced microcrystals on-site led to inability to fully validate the reduced state across samples.

Moving on to the interpretation of the redox state captured at 10 ms timepoint, it is proposed that on this timescale, given the ground (dark) state is reduced, the enzyme reaches the oxidized state upon reaction with oxygen liberated from the caged compound. However, the residual electron density found in the active site cannot be prescribed to any active site ligand, with the exception of residual chloride density, present in about 40 % of the population in the 10 ms data. The consensus interpretation of oxidized active site across literature assumes the presence of a ligand, therefore countering the proposed dynamics on a 10 ms timescale upon laser illumination. Moreover, the distance between heme a_3 Fe and the $\mathrm{Cu_B}$ observed in structure of 10 ms timepoint is approximate 5.17 Å, which corresponds to increased distance between reduced metal centers due to electrostatic repulsion, when compared with 4.98 Å in oxidized structure. Therefore, it cannot be excluded that the 10 ms structure represents a reduced for of the enzyme. However, that would require a very unlikely scenario where the crystals appear to be properly reduced in a single sample prep syringe, coincidentally used in 10 ms timepoint collection. Furthermore, it would have to assume that the oxygen does not reach the active site within 10 ms upon photo-induced cage decomposition, which would mean an error in calculations which in fact have accounted for the quantum yield of the cobalt cage compound, as well as the different diffusion rates of oxygen in LCP microcrystals compared to those in solution.

As a clear next step, optimization of the sample preparation is required, and some efforts have already been put in this direction.

As the DTBA reduced structure collected at LCLS meets the theoretically proposed model of empty active site, in addition to its better efficiency in reducing ba_3-C*c*O, DTBA is likely to be the preferred chemical reductant in experiments. Even though DTBA (as an upgrade to less efficient DTT) was chosen to prevent the premature disintegration of the cage compound, its efficiency at low pH crystal condition (pH = 5.3) is still very low. To overcome this problem, we started to develop and validate a new crystallization condition, where crystals are grown at pH = 8.0, which improves the efficiency of DTBA in reducing microcrystals. Moreover, this condition does not require sodium chloride, therefore chloride ion is no longer expected to co-ordinate the active site of resting oxidized C*c*O. Preliminary SFX data obtained at LCLS in May, 2023, shows no indication of chloride ions in either active site or the site associated with farnesyl oxygen.

Still, time-resolved X-ray diffraction studies of enzymes that are not naturally light-sensitive remain a major challenge for the field. A change of reaction initiation setup could be beneficial in studies of C*c*O activity. For example, the cobalt-based caged oxygen compound used in described TR-SFX experiment, has a sub-optimal, low quantum yield. Moreover, pre-mixing of oxygen cage along with the cocktail of chemicals, and long incubation times, compromise its reliability to sequestrate oxygen until the point of reaction initiation, which in this case resulted in premature oxygen liberation and slow turnover of the enzyme. The alternative approaches could involve new caged compounds, running a time-resolved mixing experiment, or abandoning the cage compound as an oxygen carrier in experimental design.

Building on observations of this study, future TR-SFX studies of C*c*O will explore new strategies to push the time-resolution to observe dioxygen reduction.

3.3 Paper III: A simple goniometer-compatible flow cell for serial synchrotron X-ray crystallography

Serial femtosecond crystallography was initially developed for room-temperature X-ray diffraction studies of macromolecules at X-ray free electron lasers. With the upgrades of synchrotron radiation sources, beamline aparatus, and sample delivery systems, serial crystallography successfully extends to synchrotron beamlines, and is termed serial synchrotron crystallography (SSX).

Over the last years, we have successfully utilized synchrotron radiation for serial crystallography experiments and contributed to implementation of serial synchrotron crystallography (SSX) at BioMAX beamline. In period from 2020 to 2021, the research progress was highly affected by COVID-19 pandemic, which forced X-ray facilities to restrict the access to its users. A majority of these user facilities entered the cold shutdown, temporarily suspending and postponing all of the appointed experiments. In contrast, MAX IV offered support to its users by allowing to ship samples and participate remotely, which required the shift in thought of how to design an experimental setup feasible for this type of operation.

This paper successfully demonstrates the use of custom designed and assembled flow-cell device setup for serial crystallography and spectroscopy applications at synchrotrons. Proof-of-principle experiments performed at Biomax beamline at MAX IV synchrotron validated the functionality of the flow-cell device in SSX data collection and obtaining a room-temperature SSX structure of *ba*$_3$-C*c*O.

3.3.1 Flow-cell setup

Mounted flow-cell setup for SSX data collection is illustrated in Figure 3.7.

A 100 µl Hamilton syringe containing crystals is installed on a CETONI Nemesys syringe pump and connected to the quartz tubing via syringe-needle coupler. The flow cell can support a variety of sample compositions, ranging from entirely liquid microcrystaline slurries up to viscous LCP crystals, provided the crystals remain homogenously distributed within the carrier medium throughout the experiment. Enclosed system allows for the reduced flow rates compared to GDVN and HVE injectors, preventing the aggregation and curling of the sample, thus eliminating the need for an outer gas stream. The long quartz tubing is provided to accommodate options for placement of the syringe pump, since validation studies showed that viscous samples can be transported over lines up to 50 cm in length. Still, shorter tubing is recommended to minimize the dead sample volume (~0.5 µl per cm of tubing) and prevent the accumulation of pressure along the line which can damage the setup.

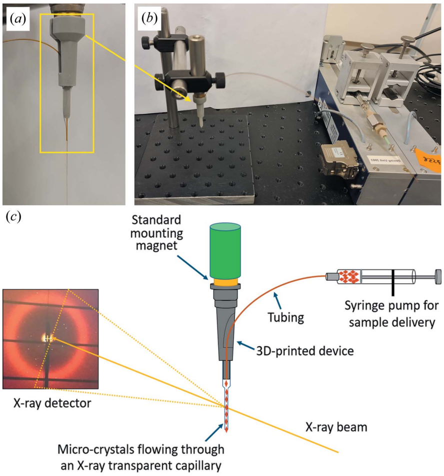

Figure 3.7: Flow-cell capillary setup for SSX data collection. A 100 µl Hamilton syringe containing crystals is installed on a CETONI Nemesys syringe pump and connected to the quartz tubing via syringe-needle coupler. 50 cm long, OD=250 µm quartz tubing transports the sample to glass capillary of preferred diameter (100 µm or 200 µm). Flow cell is compatible with the standard macromolecular crystallography goniometer, allowing for rapid mounting and alignment [87].

A flow cell was designed to be compatible with the standard macromolecular crystallography goniometer, allowing for the cell to be mounted via magnet, and aligned with the X-ray beam using the in-line visualization tools on the beamline, reducing the time for alignment to only a few minutes. Importantly, once aligned, the flow cell device can remain intact throughout the experiment, allowing for rapid re-initialization of data collection following the simple syringe exchange procedure. At low flow-rates, SSX data collection can proceed uninterruptedly for over an hour per sample syringe. A potential limitation comes from aggregation of the damaged crystals upon the interaction with X-rays, causing the blockage inside of a thin capillary. As expected, more frequent blockages were observed when 100 µm was used. Depending on the sample properties and capillary diameter, it is proposed that one to four flow cell devices can support a 24-hour beamtime.

3.3.2 Sample preparation and optimization

Protein was produced and purified via standard protocols described in 2.4. Crystallization in LCP was conducted in rounds, with screening for optimal protein concentration and v/v PEG400. Crystals of 20 - 25 µm average size were attained from 12 to 15 mg/µl *ba*$_3$-C*c*O solution mixed with monoolein in 2 : 3 ratio, extruded as 10 - 15 µl LCP threads into the precipitation solution containing 36.5 - 38.5 % PEG400. It was observed that lower protein concentration and higher PEG400 content result in formation of larger crystals (25 and larger µm), which has proven to be beneficial for performing a synchrotron experiment, where sample batches containing smaller crystals (<20 µm) show significantly weaker diffraction.

An important aspect of sample preparation was optimization of the sample for delivery through the syringe-needle coupler to quartz tubing and glass capillary, respectively. In particular, sample portions of thicker consistency can result in clogging and pressure build-up, leading to sample leakage between connection points of the setup (i.e. syringe-needle coupler, glass capillary and 3D-printed plastic element glued to the capillary, steel sleeves and the glass body of the

Hamilton syringe etc.). Clogging in downstream points can cause the incoming, more "liquid" portion to elastically reverse the flow, making the sample discontinuous inside of the long, thin tubing, with air between the columns of liquid. If the effects of these phenomena are interrupting the data collection, the change of capillary device might be required, resulting in sample loss.

For these reasons, in-house tests employing the bench-top setup were performed prior to SSX experiments. It was determined the optimal consistency for uninterrupted sample flow is achieved by "softening" the LCP sample by addition of stock PEG400 for v/v of 5 % in the final sample.

3.3.3 Data collection

Sample viewing, alignment and measurement were performed in the beamline control software MXCuBE3. Flow rates of 0.3 and 1.2 µl/min were applied for 100 µm and 200 µm capillary, respectively. LCP *ba*$_3$-*Cc*O microcrystal diffraction data were collected at room temperature using X-ray beam of 12.6 keV on an EIGER 16M hybrid pixel detector. Data was processed using standard tools for serial crystallography data analysis described in 2.2.5.

3.3.4 Comparison of diffraction data collected in 100 µm and 200 µm diameter capillaries

Results of data collection in 100 µm and 200 µm glass capillary differed significantly in several aspects. First, the indexing rate in 200 µm capillary (48.6 %) was approximately 3.5 times the indexing rate in 100 µm capillary (13.9 %), even though a two-fold difference was expected. The difference might be a result of an interrupted flow of the viscous sample at the low flow-rate and frequent clogging. Moreover, significant contribution of background scattering during the data collection in 100 µm capillary likely affected the ability to isolate crystal diffraction peaks.

As a result, the structure obtained from 100 µm capillary data collection was limited to 3.05 Å resolution, with anomalous trend in

$CC_{1/2}$ values observed near 3.0 Å resolution shell. Surprisingly, despite the thicker sample support, data collected in 200 µm retrieved a higher resolution structure supported by appropriate statistical values at 2.12 Å cutoff.

This observation was not in agreement with the preliminary experiments and anticipated performance of 100 µm capillary, which was expected to yield higher-quality X-ray diffraction data and exhibit lower background X-ray scattering.

3.3.5 Background X-ray scattering

Further examination of X-ray scattering decomposed contributions of borosilicate glass and LCP medium. Comparison of background signal from both 100 µm and 200 µm empty capillaries showed the scattering from 100 µm capillary to be two times stronger than the one of 200 µm capillary. A possible explanation to this phenomenon could be a manufacturing error, resulting in deviation from nominally defined 10 µm thickness of borosilicate glass. LCP component, however, yields a lower background signal when extruded from 100 µl. Still, the cumulative contribution of these two effects rules out in favor of 200 µm capillary, which is therefore recommended to use, unless slower flow-rate and lower sample consumption is required.

3.3.6 Comparison of 200 µm SSX structure with SFX structure

SSX structure obtained from 200 µm capillary, and resolved to 2.12 Å, displays high similarity with previously published 2.3 Å SFX structure ([113], PDB: 5NDC), such as comparable resolution, similar features of $2F_{obs}-F_{calc}$ electron density maps, and plausible figures of merits, with slight difference in the shape of the density peak of the active site ligand (Figure 3.8).

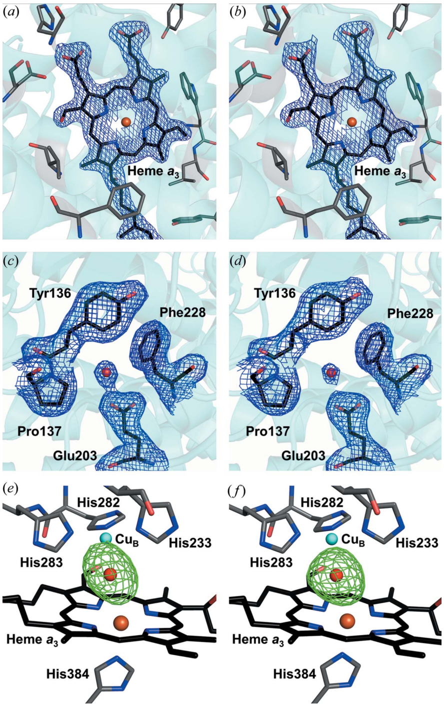

Figure 3.8: Comparison of SSX structure obtained using a flow cell and SFX structure. $F_{obs}-F_{calc}$ electron density (green) maps calculated by omitting the active site ligand between the heme a_3 iron and the Cu_B copper atom display comparable electron density peaks in the active site, with slight a difference in shape of a density peak in SSX (elliptical) and SFX (spherical) structure, and no observable changes of the radiation-sensitive residues (Glu203) [87].

3.3.7 Radiation damage

The calculated average room-temperature X-ray dose per microcrystal is 40 kGy, which is nominally the lower dose limit for sensitivity of metals, such as iron, to display X-ray induced damage at low temperature. Therefore, the modest elongation of the active site electron density peak in the $F_{obs}-F_{calc}$ omit electron density map could theoretically be prescribed to radiation damage of the metal centers. However, no observable changes of the radiation-sensitive residues (such as glutamic acid) indicate no local site-specific damage. Still, to ensure the damage-free data collection, it is advised to properly access and optimize X-ray beam focus or degree of attenuation, as well as the sample flow-rate.

3.3.8 Conclusions and outlook

Proof-of-princple experiments conducted at Biomax, MAX IV, validated the use of glass capillary flow-cell device for SSX and retrieved a high-resolution room-temperature structure of *ba*$_3$-C*c*O. A 2.1 Å structure of the resting, oxidized enzyme in LCP was collected in 200 µm glass capillary with minimized effect of the glass background scattering. The comparison of SSX structure (PDB ID: 8HUA) with previously published 2.3 Å SFX structure of *ba*$_3$-C*c*O [113] reveals nearly identical structural features of the active site, demonstrated by $2F_o-F_c$ maps. In addition, the comparison of side-chain aminoacids, such as glutamates, accessed by composite omit maps, shows no clear signs of disintegration in response to X-ray induced radiation damage.

The capillary flow device was used in experiments at BioMAX to collect SSX data on other redox states, such as chemically reduced states obtained by treatment with sodium dithionite (described in following section 3.4 as a part of Paper IV) and DTT, as well as in mixing experiments to obtain reaction intermediates of *ba*$_3$-C*c*O, such as Pm intermediate and mixed-valence CO-bound state (MVCO). The device has as well been employed to collect data at other synchrotron facilities, such as ESRF, where it was recently used in combination with laser diode optical fiber setup. This type of experiment proves the potential of flow-cell device to be used in reaction dynamics and time-resolved studies, and represents a milestone in gradual translation of time-resolved serial crystallography to synchrotron light sources.

Given the number of synchrotron light sources, and hence available beamlines, there is large capacity for growth in the use of SSX.

Still, the entry barriers for inexperienced users, such as the need to grow large volumes of micrometre-sized crystals and grasp knowledge of data processing pipelines, are still the bottleneck of maximizing the potential of SSX. Nevertheless, demonstrated method of SSX data collection, as well as the use of capillary device for UV-Vis spectroscopy or X-ray scattering, has a potential to significantly reduce the time and cost of the experiment, and facilitate the execution of the experiment, thus allowing for the broader research community to utilize the power of synchrotron radiation. In that regard, this subproject turned into a startup venture with the help of GU Ventures, providing devices synchrotron beamlines and academic users.

3.4 Paper IV: X-ray absorption spectroscopy of *ba*$_3$-type cytochrome *c* oxidase

Given its biological importance for the life of aerobic organisms on Earth, as well as well-conserved structural elements of heme-copper oxidases, cytochrome *c* oxidase has been an "obvious" target for XAS studies. Even though a few spectroscopic techniques allow monitoring of all the metal sites in C*c*O, the existence of multiple atoms in different redox and spin states, as well as the electronic coupling in the binuclear active site, have made the spectroscopical characterization very challenging.

For example, both heme *a*/*b* and heme *a*$_3$ are easily followed in the visible (UV/Vis) spectrum, but the coppers absorb only very weakly in the near infrared, with Cu(I) absorbing weakly near 830 nm, and Cu(II) lacking any well-defined absorption peaks. Moreover, the antiferromagnetic coupling between high-spin heme *a*$_3$ Fe(III) and Cu$_B$(II) results in a rapid spin transition and produces a so called "S2 ground sate". Such coupling [130] explains the lack of EPR signals typical of high-spin (HS) Fe(III) heme and Cu(II) across the family of heme-copper oxidases.

XAS, on the other hand, overcomes these limitations through its ability to probe "silent" redox states. It is also element selective, allowing for the iron sites to be studied independently of the copper sites.

We use X-ray absorption spectroscopy (XAS) to investigate the detailed atomic structures of the metal co-factors in different redox states of C*c*O. Nevertheless, this project pioneers the use of XAS for cytochrome *c* oxidase study at Balder beamline. This research contributes towards our long-term goal to use time-resolved XAS in combination with time-resolved serial femtosecond crystallography at XFELs for a comprehensive structural study of C*c*O activity.

3.4.1 Sample preparation and validation of C*c*O redox states

A recommbinant *ba*$_3$-C*c*O protein was produced in its native host *T. thermophilus* and purified as described previously [113].

Chemical reduction of the protein, validation of redox states, as well as the final sample preparation and sample loading, were carried out on-site at MAX IV Biolab prior to the experiment. Steps requiring oxygen-free conditions were performed inside of the COY vinyl anaerobic glovebox. In addition, all the solutions and powders were incubated in the stream of nitrogen gas prior to handling, to exchange gases and eliminate the residual oxygen.

To access the difference in electronic configuration and coordination of the heme a_3 in the binuclear active site of C*c*O, two different reduction protocols were employed and two distinct samples were obtained, denoted as "*red* " and "*red-air*", where the first is carried out in controlled anaerobic conditions, and the latter in the presence of oxygen. Both states were characterized by UV-Vis spectroscopy (Figure 3.9). Spectral features of "red-air" spectrum indicate a ligation to the iron of the heme a_3, likely by a strong field ligand, accompanied by heme a_3 spin-state change from high to low.

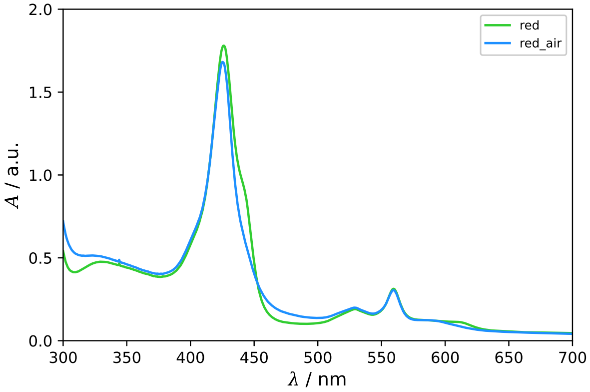

Figure 3.9: UV-Vis spectroscopy validation of samples for XAS analysis. "red" exhibits characteristic C*c*O Soret peak At 426 nm with the characteristic "shoulder" at 445 as a contribution of the reduced heme a_3 in un-ligated state. Absorption peak at 560 nm indicates the reduced heme b_3. Characteristic 560 nm peak confirmed the reduced state of heme b_3 in "red-air". Additional weak peak observed at 610 nm is assigned to ligated heme a_3, as well as disappearing of the "shoulder" at 445 nm.

3.4.2 Cryo-XAS at Balder beamline at MAX IV synchrotron

XAS measurements were performed at Balder, a high-flux wiggler beamline for X-ray absorption and emission spectroscopy at MAX IV synchrotron light facility.

Approximately 50 µl of each sample containing v/v 20% cryoprotectant were loaded into multi- sample holders with round “windows” fitting 13 mm-diameter pellets sealed with Kapton foil using a blunt-end 100 µl Hamilton syringe. All samples were flash-frozen in liquid nitrogen prior to mounting.

XANES and EXAFS at iron K-edge and copper K-edge were measured at 10 K in a liquid-helium cooled cryostat. The excitation energy for both edges was selected by a Si-111 double-crystal monochromator, and the energy axis was calibrated with repeated spectra of iron and copper foil, with the first inflection point assigned as 7112 eV and 8979 eV, respectively. Data was collected in fluorescence "fly scan" mode using 7-element SDD detector, continuous scanning down to 30 sec/EXAFS. EXAFS scans were collected up to k-14 Å^{-1}.

3.4.3 Data processing

XAS data treatment was performed using *Demeter* software package [131].

Data averaging and normalization Summed data from all 7 detector fluorescent channels were inspected to isolate and remove low-quality scans that contain glitches as a result of ice formation in the sample. High-quality raw data was included in the final average and further processed in *Athena*. The EXAFS oscillations were extracted using standard procedures for pre-edge and post-edge background subtraction, and data normalization.

EXAFS data fitting EXAFS data fitting was performed in *Artemis*.

The $k3$-weighted EXAFS oscillations were analysed using a non-linear least-squares fitting procedure in k-space and plotted as amplitudes $|\chi(R)|$ as a function of radial distance (R) in Å.

Theoretical phase and amplitude functions were calculated *ab initio* using built-in computer code *FEFF7* [95]. Structure data input for *FEFF7* calculations was obtained from previously published serial crystallography room-temperature *T. thermophilus ba*$_3$-C*c*O structure [113] (PDB: 5NDC) as five different cofactor-specific coordinate files, containing the neighboring atoms within 5Å radius from the central absorber atom.

Fitting parameters used to generate model fits of Cu and Fe EXAFS of three analyzed samples are reported in the fitting tables along with the statistical evaluation factors.

Co-ordination number N for each shell were chosen in agreement with crystallographic values, and fixed as integer per three copper atoms, or per two iron atoms, respectively. Restraints were placed on the amplitude factor values in agreement with the standards (typically > 0.7 and < or = 1). In contrast, factors such as distances from the absorbing atom, Debye-Waller factor, and E_0 were allowed to float, with some constraints so as to produce Debye-Waller factors within reasonable limits ($0.001 > \sigma > 0.01$). The quality of the fits was determined using a reduced χ^2 (2.10) and R-factor (2.12).

3.4.4 SSX of NaDt-reduced *ba*$_3$-C*c*O microcrystals

Microcrystals of *ba*$_3$-C*c*O were produced according to previously published crystallization protocols [113,117], and as described in 3.2 and 3.3. Serial crystallography data collection was performed at BioMAX beamline at MAX IV, where crystals were treated with sodium dithionite (NaDt) prior to experiment, and injected using a flow-cell setup [87], described in 3.3. The structure was solved to a resolution of 2.4 Å (Table S3 in Paper IV).

3.4.5 Qualitative analysis of XANES

XANES data of both Cu and Fe K-edge was accessed by qualitative analysis of the features of the rising edge and the pre-edge.

Cu- and Fe- K-edge XANES as a fingerprint of redox state Merged and averaged spectra of Cu and Fe K-edge XANES of analyzed redox states of C*c*O shown in Figure 3.11.

The absorption edge shift to lower energies observed in reduced samples is consistent in both Cu and Fe XANES, and confirms the difference in redox state between "ox", "red", and "red-air" sample. In particular, the binding energy of a core electron is lower for an element in the reduced state, as the effective nucleus charge (Z_{eff}) is lower due to the increased number of electrons compared to the oxidized state. Interestingly, "red" is shifted further to the left compared to "red-air", implying the overall contribution of reduced character to be higher in "red".

Still, it is important to acknowledge that position and the shape of the edge can be affected by several factors, and the shifts can vary from element to element. For instance, Ni complexes do not demonstrate particularly large rising-edge shifts with change in oxidation state and in some cases there is no observable edge-shift [94].

Radiation damage sensitivity of C*c*O The radiation sensitivity of oxidized ba_3-C*c*O sample was observed in the preceding, preparatory experiment, where EXAFS data was collected up to k-12 Å^{-1} at 9000 eV using protocol which employed focused beam and 2 scans per spot. 10 repeats of a single scan per spot were performed, with sample holder being translated by 0.3 mm along the y-axis after each repeat. With the flux of $1.24 \cdot 10^{12}$ photons/s, the radiation dose was calculated to be 119 kGy per second.

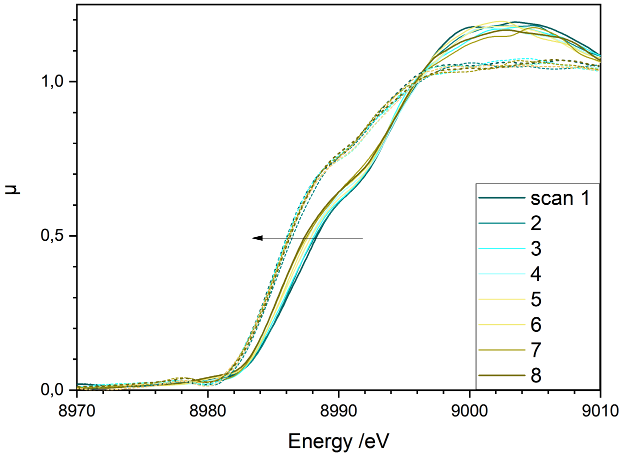

Figure 3.10: Cu K-edge XANES study of radiation damage sensitivity 8 single scans (each 4 min) were collected on the same position of the sample holder, resulting in an accumulate radiation dose of 224 MGy after the eights scan (32 min). In the oxidized sample, the shift of the spectra to lower energy values with each scan indicates reduction of the copper atoms. The onset of the radiation damage is observed after scan 2 and a dose of 56 MGy.

Oxidized sample was tested for radiation damage due to sensitivity of absorber metals to ionizing X-ray radiation, as well as the secondary effects upon X-ray induced water radiolysis. The effect of the radiation damage was accessed by comparing Cu K-edge XANES of 8 scans (Figure 3.10). It was observed that with each new scan, the spectra were shifted more towards lower E values, which is an indication of the reduction of Cu and considered a radiation damage.

The output of this study was valuable in modifying the setup in the following experiment, where the effects of X-ray-induced damage were surpassed by lowering the flux down to $5.4 \cdot 10^{11}$ photons/s, resulting in radiation dose of 64 kGy per second for Cu, and 77 kGy per second for Fe K-edge.

Pre-edge analysis Theoretically, the analysis of the pre-edge region, dominated by 1s→3d transitions, could give an insight to the electronic configuration and the geometry of the environment surrounding the absorber atoms. In particular, copper in its oxidized state (Cu(II)) has an unfilled 3d orbital (a "3d hole"), and therefore can experience 1s→3d transition, unlike Cu(I).

In Cu XANES of three analyzed states (Fig. 3.11, A) the pre-edge region can be identified a bit higher and closer to the rising edge, than the one of Fe XANES (Fig. 3.11, B). As observed for a number of complexes, Cu(I) compounds exhibit a low energy peak maximum at ∼ 8982 eV, as observed clearly in "red", while Cu(II) compounds exhibit a characteristic 8985 eV peak, visible in "ox".

In Fe systems, the energy position and splitting, and intensity distribution, of the pre-edge feature can vary systematically with spin state, oxidation state, geometry, and bridging ligation [132], such as one in heme a_3-Cu$_\mathrm{B}$ binuclear center. The allowable many-electron excited states for high- and low-spin complexes are determined using ligand field theory. Upon ligation, the mixing of 4p character into the 3d orbitals results in a 1s → 4p electric dipole contribution to the pre-edge, therefore increasing its intensity. A difference in peak observed at ∼7115 eV for "red-air" when compared with "red" could mean a stronger pre-edge feature and 3d-4p mixing upon ligation.

However, the resolution of the pre-edge region in collected data is not sufficient to make this assessment. Experimentally, this could be improved by employing finer, smaller energy steps scanning the pre-edge region, and generally increasing the amount of collected data.

Rising edge analysis In Cu systems, the intensity of 1s→4p transitions visible in the rising edge region is a direct consequence of the degeneracy of 4p orbitals [133] co-ordination geometry. In systems with a low-lying 4p orbital, such as Cu(I), the features of the rising edge can be used to determine co-ordination number and geometry. Two reduced samples analyzed by Cu XANES (Figure 3.11, A) differ in this region, which could indicate presence of the ligand in "red-air", and a change of co-ordination number (geometry). "ox" sample appears very different to reduced samples, displaying spectral features similar to those of Cu(II) standards. The resolution of this region is not good enough to make a strong qualitative assessment.

In Fe XANES of analyzed samples (Fig. 3.11, B), the shape and height of the peak occurring at $\sim$ 7130 and $\sim$ 7140 eV in oxidized and reduced samples correspond to those observes in Fe K-edge XANES of Fe(III) and Fe(II) complexes, respectively. Interestingly, analyzed samples as well differ in region from 7130 to 7160 eV, dominated by multiple scattering. In theory, the shape and energy position of this region can be correlated with the ligand-type and metal–ligand bond distance in transition metal complexes. The relation proposed by Natoli, and further developed by Mahto and Chetal, considers systems that can exist different redox and spin states [94]. Typically, there is an $\sim$ 2 eV shift between high-spin Fe(II) to a high-spin Fe(III) complex, which can as well be observed between analyzed "red" and "red-air" samples. Moreover, low-spin Fe(II) and high-spin Fe(III) species with similar ligand systems can have similar bond distances [134] and often their rising-edges occur very close in energy.

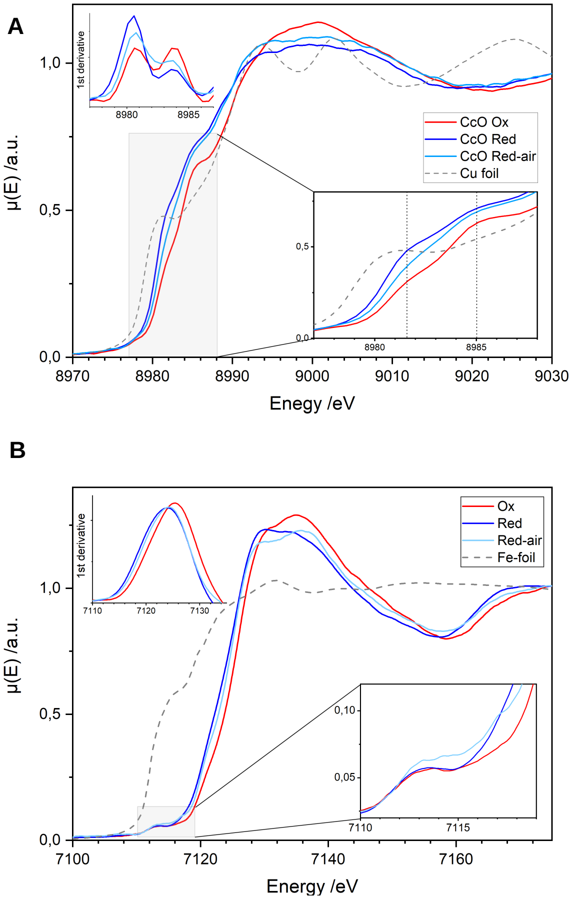

Figure 3.11: Copper (A) and iron (B) K edge XANES of *ba*$_3$–type C*c*O. Shift of the absorbtion edge towards lower energies is observed for reduced samples. The edge energy position is determined from the first inflexion point of the first derivative of the rising edge (top left). Zoom of the pre-edge region (bottom right) reveals subtle peaks originating from valence state-specific 1s→3d transitions.

3.4.6 Accessing the co-ordination environment of *ba*$_3$-C*c*O

Cu EXAFS C*c*O contains well-defined binuclear Cu$_A$ site, which is co-ordinated by 2 histidines, 2 cysteines, 1 methionine and 1 glutamine. Cu$_B$ in heme *a*$_3$ Cu$_B$ active site is co-ordinated by three nitrogen atoms of histidines in its reduced state (Cu(I)), and is expected to ligate a fourth co-ordination atom when oxidized (Cu(II)). Sulphur contribution to the spectrum originate from cysteines and methionine, and is therefore characteristic of the Cu$_A$ site. Nitrogens originating from histidines at both Cu$_A$ and Cu$_B$ are found at the similar distances, and therefore contribute to the same shell. Moreover, due to the limitation of the method to successfully distinguish between N and O, oxygen atoms can as well be fit in the nitrogen shell, which was explored when fitting "red-air" data. One oxygen atom present in all three datasets originates from the carbonyl group coordinating Cu$_A$. In structure of resting oxidized enzyme [113], oxygen atom originating from the water in the active site is placed at $\sim$ 2.3 Å from Cu$_B$, therefore a 2.3 Å oxygen shell was included in the fits. Oxygen atoms from side chains surrounding Cu$_B$ are on the border of what can be covered by EXAFS ($R > 4.5$ Å) and therefore are not used to fit Cu EXAFS.

In cases where XAS spectrum is dominated by the presence of histidine ligands, the information has often been restricted to the first- and sometimes second-shell coordination spheres [135]. Due to the limited number of parameters we can extract from the data ($N_{\mathrm{idp}} \approx \frac{\Delta k \Delta R}{\pi} \approx 13$), and feasible fits (Table S2 in Paper IV) obtained by single atom scattering shells, multiple scattering was hereby not considered in Cu EXAFS fitting.

Experimentaly obtained EXAFS data of all three analyzed states differ between each other with more similarity observed between "red" and "red-air". Interestingly, a striking difference between the oxidized and reduced samples can be observed when comparing FT-EXAFS spectra, where the relative amplitude of the peak at 1.5 Å in the "red" sample is significantly lower compared to the oxidized spectrum, while it is almost completely vanished in "red-air". Moreover, the major peak at ∼2 Å, dominant in all samples, has a significant shoulder at ∼2.3 Å that is less prominent in the "red" spectrum. This could be attributed to an active site oxygen ligand coordinating Cu_B as has been previously observed.

3.4.7 In the light of the new crystallographic evidence

Updated model of a resting oxidized state of *ba*$_3$-C*c*O It is important to note that 2.3 Å oxygen shell proposed in Cu EXAFS model is in the agreement with the distances derived from room-temperature serial crystallography structure of *ba*$_3$-C*c*O in the oxidized state previously reported by our group [113], where the active site ligand is interpreted as a water or a hydroxide ion. Recent data (described in 3.2) suggest the ligand bound in the active site, at the given crystallization condition, is a chloride ion, originating from precipitation solution of a very high chloride concentration. Even though the sample for the XAS experiment was prepared in a buffer of a low chloride concentration and is not expected to bind a chloride in the active site, the relative placement of the oxygen atom as modeled corresponds to the placement of chloride and closer to the Cu_B, while it is expected to be co-ordinating the heme *a*$_3$ Fe.

SSX structure of NaDt-treated *ba*$_3$-C*c*O SSX diffraction data (Figure 3.12) obtained upon treatment with sodium dithionite as a reducing agent, in the presence of oxygen, revealed strong electron density in the active site of *ba*$_3$-C*c*O, indicating a bound ligand.

This observation is in the agreement with the UV-Vis spectrum of the crystalline sample, where a feature at 590 nm indicates a ligand bound to heme *a*$_3$ in the active site. Nominally, 590 nm peak in the spectrum is a signature of the A-intermediate of the cytochrome *c* oxidase reaction cycle, where oxygen molecule is bound to reduced Fe(II) active site. Throughout sample preparations, it was observed that this enzymatic species forms upon reduction of C*c*O with dithionite when there is residual oxygen present during the chemical treatment.

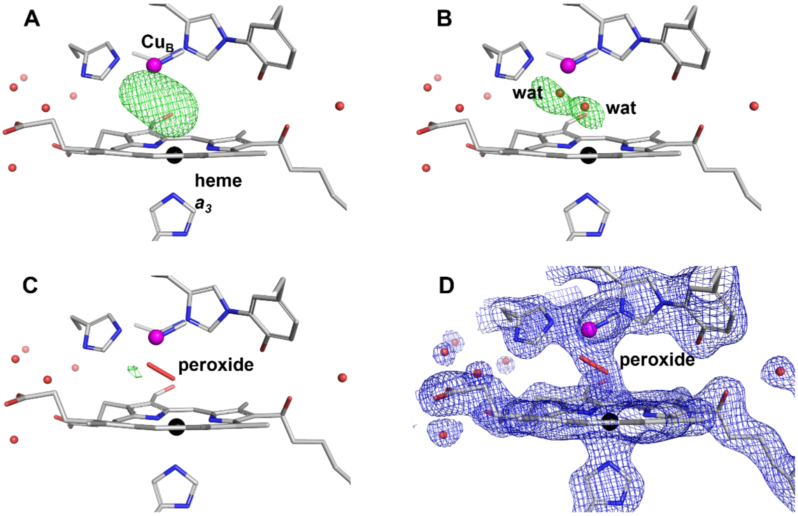

Figure 3.12: Active site of the C*c*O enzyme reduced in the presence of residual oxygen. Based on the $F_{obs}-F_{calc}$ omit-map density (A), fitting of two hydroxide (water) ligands of partial occupancy (B) and peroxide ligand (C) were explored. The $2F_{obs}-F_{calc}$ electron density map of the structure with a peroxide molecule modelled in the active site (D) supports the choice of peroxide ligand.

Crystallographic modeling revealed plausible structures when a peroxide, or two hydroxide (water) ligands with partial occupancy (0.5) were fit, respectively, while fitting a single full-occupancy water (hydroxide) molecule resulted in strong residual electron density. In the peroxide-bound structure, the O–O bond length of the peroxide refines to 1.5 Å, which is considered a reasonable bond distance of a peroxide dianion (O_2^{2-}) [136]. Structures of the oxidized as-isolated state of C*c*O have frequently been modelled with a peroxide active site ligand [137] even though the chemical rational for a peroxide ligand in the active site of the oxidized form of the enzyme is not clear. In the scope of this study, there is no obvious explanation for the formation of a peroxide ligand during preparation of dithionite reduced crystals used in the current experiment.

Fe EXAFS Two Fe atoms of C*c*O are embedded in porphyrine ring of heme a_3 and heme b, containing a number of symmetrically arranged carbon and nitrogen atoms, and are as well co-ordinated by one or two axial imidazole groups, respectively. In such a symmetrical system, multiple scattering is considered to significantly contribute to EXAFS. Generally, strong multiple-scattering contributions are present in the EXAFS over an extended range above the absorption edge. By including multiple scattering in the EXAFS analysis, it is possible to extend the low-energy fitting range to include regions of the low k (for example, below $k = 3$). Therefore, multiple scattering paths obtained by *FEFF7* calculations were used in fitting Fe EXAFS of all three analyzed datasets. Contribution of the $\mathrm{Cu_B}$ in Fe EXAFS is expected to be minor, due to the relatively big distance from heme a_3 Fe ($\sim$ 4.8 Å), and therefore was not explored in fits.

Fe EXAFS data was fit in the shorter k-range up to $k = 12.5$ to emphasise oscillations in the lower k region. The shift in experimentally obtained EXAFS of all three analyzed samples can be observed in the region from 4 to 7 Å^{-1}. EXAFS as well appears different between samples when plotted as a function of $|\chi(R)|$.

Single scattering shells were defined according to nitrogen and carbon shells of the well-ordered porphyrin structure. Three multiple scattering shells were included in the fits. Oxygen shell was not added to these fits, therefore the identity of the potential ligand in the "red-air" sample cannot be accessed. Including multiple scattering shells gives produced successful fits of low k region, revealing an interesting shortening of the Fe–N distance in "red-air" compared to "red". In particular, shorter Fe–N distances within the porphyrine group are observed in oxidized sample, as a consequence of ligand binding to the high-spin heme. Therefore, this finding could indicate the ligation at the heme a_3 Fe site.

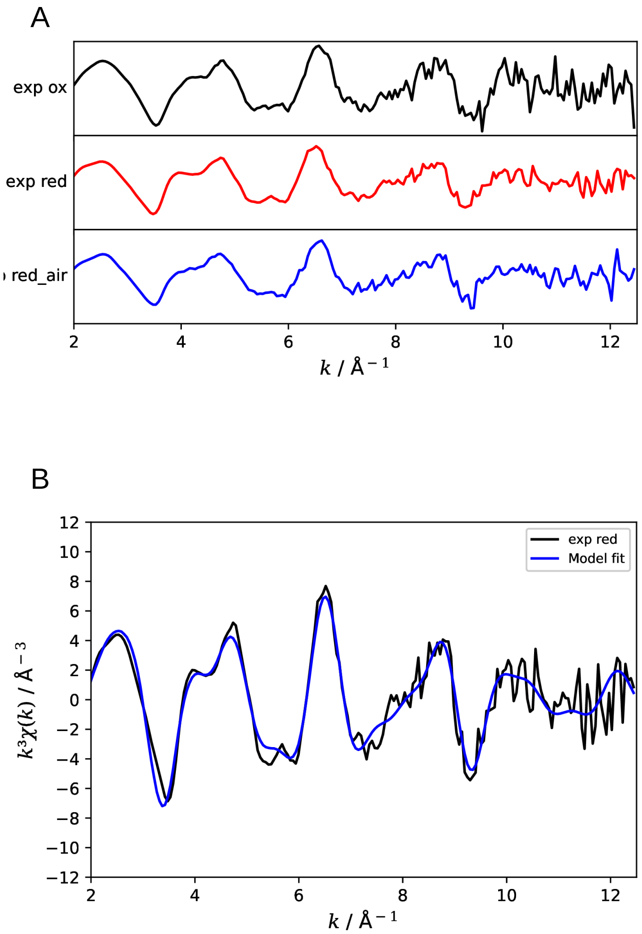

Figure 3.13: Interpretation of the Fe EXAFS. The differences between experimentally obtained EXAFS (A) "ox", "red", and "red-air" is observed in the low k region (4-7 Å^{-1}). Fitting of the multiple scattering (MS) functions (B) was performed to describe the contributions of well-ordered porphyrin and imidazole groups in this region, revealing shortening of Fe–N distances in reduced samples.

3.4.8 Conclusions and outlook

This study demonstrates that XAS can be used to analyze metal co-factors of C*c*O. Both XANES and EXAFS collected at Cu and Fe K-edge display differences between three analyzed redox states of C*c*O. However, due to the multiple number of the spatially separated absorbers of the same element (3 Cu, 2 Fe) in the protein, the bulk nature of XAS method does not allow to differentiate between the contributions from different co-factors. Moreover, obtaining an EXAFS model of high fidelity has proven to be difficult.

Before studying a complex, multiple co-factor system, a good approach would be to study the co-factors of *ba*$_3$-C*c*O individually. For example, Cu$_A$-depleted quinol oxidases [138], as well as isolated Cu$_A$ domains [139], could be used to gain the understanding of the Cu$_B$ site.

Nevertheless, XANES can be successfully used as a fingerprint of the redox state. The shift of the absorption edge towards lower energies upon reduction is traditionally used as the most immediate proof of redox change. However, position and the shape of the edge can be affected by several factors, and the shifts are element-specific, so it is good to extend the assessment of the redox state to other qualitative or quantitative approaches.

In transition metal co-factors, the redox state can be further accessed by analyzing the pre-edge. The intensity of the 1s→3d transition featured in pre-edge can give information on electronic configuration and the co-ordination geometry of the absorber. Therefore, a higher resolution of the pre-edge region would be valuable in the assessment of metal co-factors of C*c*O. This can be experimentally obtained by fine-tuning the energy steps for pre-edge region scanning.

In addition, using computational methods, such as *Orca*, in quantitative interpretation and modeling of XANES spectra, would be one of the next steps in understanding XANES of *ba*$_3$-C*c*O. TD-DFT calculations have been initiated but are not featured in the scope of Paper IV or this thesis.

In the scope of this study, it was also observed that oxidized cofactor sites, especially copper, were prone to radiation damage during XAS data collection at low temperatures. Radiation damage study on copper helped in establishing a better experimental setup, which ultimately resulted in lowered radiation dose in the following experiment and obtaining damage-free datasets.

Still, in addition to trapping the radiation damage intermediates, cryo-XAS data collection carries the problem of ice formation inside of the solution samples, which is shown as as glitches in the XAS spectra, and can result in discarding a large amount of data. For low concentrated biological samples, where the concentration of the absorber often does not exceed 5 mM, the amount of collected data is critical. This issue could be countered by running a room temperature collection using the flow cell, allowing for the sample to be constantly replenished. Due to the heavy requirements on the sample consumption, this alternative was not explored in the scope of the thesis. The future plans involve the use of AdaptoCell, a flow cell provided at Balder, MAX IV.

Touching on the topic of sample requirements, absorber concentrations, and the intensity of the signal, using protein crystals instead of the protein in solution could as well be explored, as the highly-ordered solid containing a large number of packed protein molecules would give a stronger absorption signal. Moreover, using C*c*O crystals for XAS data collection would open the possibility to consider polarized XAS [140], which allows us to selectively enhance specific transitions with respect to the incident X-ray polarization vector, thereby giving rise to the selected transitions.

In the future, one could envision a setup in which X-rays are used for simultaneous X-ray diffraction (XRD) and spectroscopic characterization of C*c*O crystals, where the redox and spin state of metal co-factors is directly probed to ensure that the atomic structure revealed by XRD displays the correct catalytic state [141]. Recently reported [142] approach which combines XRD and X-ray emission spectroscopy (XES) was used to characterize microcrystals of photosystem II (PSII) at room temperature using intense femtosecond

X-ray pulses produced at LCLS. XES probes occupied electron levels, where the K$\beta_{1,3}$- line can be used as a probe of the number of unpaired 3d electrons, hence providing information about the oxidation and/or spin state of the metal co-factor. Optimization of sample delivery conditions to support both methods simultaneously would be one of the main bottlenecks in designing this approach.

3.5 Summary of the results and final concluding remarks

In paper I, TR-SFX study of CO-bound *ba*$_3$-C*c*O explores structural changes in response to photoinduced dissociation of CO from the active site, where the observations at the millisecond timescale highlight the difference between *ba*$_3$- and *aa*$_3$-type of C*c*O, and can be used as a proxy in understanding of oxygen-binding affinity and dynamics.

Building on knowledge of sample preparation and experimental setup for time-resolved studies of C*c*O, in paper II, we employed TR-SFX to study structural changes in *ba*$_3$-C*c*O upon reaction with dioxygen, released from the photosensitive cage upon time-controlled laser illumination. High resolution diffraction data collected at SwissFEL and LCLS XFEL facilities reveals interesting phenomena relative to crystallization conditions, chemical reduction treatment of the crystals, and ultimately, following the reaction with dioxygen, tracked at 10 ms and 30 ms upon laser illumination. Based on the observations from the SFX data, UV-Vis spectroscopy studies, and consensus literature, we hypothesised on possible model of C*c*O reduction dynamics, and functional interpretation of dioxygen-induced changes. Future studies will explore different sample preparation protocols, and possibly different takes on time-resolved pump-probe setup.

To establish a feasible serial crystallography pipeline to study

C*c*O using synchrotron radiation, we designed a cost-efficient, user-friendly syringe-coupled flow cell device, which allows for uninterrupted viscous sample flow and SX data collection at room temperature. Proof-of-principle experiments using LCP microcrystals of resting oxidized *ba*$_3$-C*c*O validated the use of flow cell in serial synchrotron crystallography (SSX), yielding a high-resolution structure resembling room-temperature SFX structure previously obtained by our group [113]. Application of the flow-cell device is extended on other states of C*c*O, as well as on other protein systems and sample media, and is currently offered at several synchrotron facilities.

Finally, to overcome the limitations of crystallography and other spectroscopy methods (UV-Vis, EPR) in studying silent redox states of transition metal co-factors of enzymes, we explore X-ray absorption spectroscopy to study different redox states of copper and iron atoms in co-factors of *ba*$_3$-C*c*O. Interpretation of spectral features, resulting from core electron transitions and photoelectron scattering of neighboring atoms, was accessed by qualitative analysis of X-ray absorption near-edge structure (XANES) and theory-based model calculation for extended X-ray absorption fine structure (EXAFS) fitting. Despite C*c*O being a complex system to study with XAS, experimental data and mathematical model successfully highlighted differences between three analyzed redox states of C*c*O. Nevertheless, further improvements to the model are needed to explain the possible ligation environment in the active site, while computational approaches might elucidate information contained in low-resolution XANES features for a detailed electronic configuration fingerprint.

In conclusion, the synthesis of information obtained by SX and XAS, supported by UV-ViS, highlight the importance of multiplexing crystallography-based with spectroscopy-based approaches in obtaining a more extensive knowledge of complex biochemical systems.

Bibliography

[1] K. Zahnle, L. Schaefer, and B. Fegley, "Earth's Earliest Atmospheres," *Cold Spring Harbor Perspectives in Biology*, vol. 2, pp. a004895–a004895, 10 2010.

[2] M. T. Rosing, "^{13}C-Depleted Carbon Microparticles in >3700-Ma Sea-Floor Sedimentary Rocks from West Greenland," *Science*, vol. 283, pp. 674–676, 1 1999.

[3] J. B. Jackson, "Natural pH Gradients in Hydrothermal Alkali Vents Were Unlikely to Have Played a Role in the Origin of Life," *Journal of Molecular Evolution*, vol. 83, pp. 1–11, 8 2016.

[4] A. Bekker, H. D. Holland, P.-L. Wang, D. Rumble, H. J. Stein, J. L. Hannah, L. L. Coetzee, and N. J. Beukes, "Dating the rise of atmospheric oxygen," *Nature*, vol. 427, pp. 117–120, 1 2004.

[5] J. J. Brocks, G. A. Logan, R. Buick, and R. E. Summons, "Archean Molecular Fossils and the Early Rise of Eukaryotes," *Science*, vol. 285, pp. 1033–1036, 8 1999.

[6] J. Olejarz, Y. Iwasa, A. H. Knoll, and M. A. Nowak, "The great oxygenation event as a consequence of ecological dynamics modulated by planetary change," *Nature Communications*, vol. 12, p. 3985, 6 2021.

[7] V. J. Thannickal, "Oxygen in the Evolution of Complex Life and the Price We Pay," *American Journal of Respiratory Cell and Molecular Biology*, vol. 40, pp. 507–510, 5 2009.

[8] P. MITCHELL, "Coupling of Phosphorylation to Electron and Hydrogen Transfer by a Chemi-Osmotic type of Mechanism," *Nature*, vol. 191, pp. 144–148, 7 1961.

[9] R. R. Ramsay, "Electron carriers and energy conservation in mitochondrial respiration," *ChemTexts*, vol. 5, p. 9, 6 2019.

[10] E. Racker and W. Stoeckenius, "Reconstitution of purple membrane vesicles catalyzing light-driven proton uptake and adenosine triphosphate formation.," *The Journal of biological chemistry*, vol. 249, pp. 662–3, 1 1974.

[11] J. A. García-Horsman, B. Barquera, J. Rumbley, J. Ma, and R. B. Gennis, "The superfamily of heme-copper respiratory oxidases," *Journal of Bacteriology*, vol. 176, pp. 5587–5600, 9 1994.

[12] M. M. Pereira, M. Santana, and M. Teixeira, "A novel scenario for the evolution of haem-copper oxygen reductases," *Biochimica et Biophysica Acta - Bioenergetics*, vol. 1505, pp. 185–208, 6 2001.

[13] S. Iwata, C. Ostermeier, B. Ludwig, and H. Michel, "Structure at 2.8 Å resolution of cytochrome *c* oxidase from *Paracoccus denitrificans*," *Nature*, vol. 376, pp. 660–669, 8 1995.

[14] T. Tsukihara, H. Aoyama, E. Yamashita, T. Tomizaki, H. Yamaguchi, K. Shinzawa-Itoh, R. Nakashima, R. Yaono, and S. Yoshikawa, "The Whole Structure of the 13-Subunit Oxidized Cytochrome *c* Oxidase at 2.8 Å," *Science*, vol. 272, pp. 1136–1144, 5 1996.

[15] M. Svensson-Ek, J. Abramson, G. Larsson, S. Törnroth, P. Brzezinski, and S. Iwata, "The X-ray Crystal Structures of Wild-type and EQ(I-286) Mutant Cytochrome *c* Oxidases from *Rhodobacter sphaeroides*," *Journal of Molecular Biology*, vol. 321, pp. 329–339, 8 2002.

[16] J. E. Morgan, M. I. Verkhovsky, and M. Wikstrm, "The histidine cycle: A new model for proton translocation in the respiratory heme-copper oxidases," *Journal of Bioenergetics and Biomembranes*, vol. 26, pp. 599–608, 12 1994.

[17] T. Soulimane, G. Buse, M. Dewor, M. E. Than, and R. Huber, "Primary structure of a novel subunit in ba_3 -cytochrome oxidase from *Thermus thermophilus*," *Protein Science*, vol. 9, pp. 2068–2073, 2000.

[18] M. A. Sharpe, M. D. Krzyaniak, S. Xu, J. McCracken, and S. Ferguson-Miller, "EPR Evidence of Cyanide Binding to the Mn(Mg) Center of Cytochrome *c* Oxidase: Support for $\mathrm{Cu_A}$-Mg Involvement in Proton Pumping," *Biochemistry*, vol. 48, pp. 328–335, 1 2009.

[19] E. Nyvltova, A. Barrientos, and J. Hosler, "Assembly of Heme a_3-CuB and CuA in Cytochrome *c* Oxidase," *Encyclopedia of Inorganic and Bioinorganic Chemistry*, pp. 1–27, 9 2017.

[20] J. A. Keightley, B. H. Zimmermann, M. W. Mather, P. Springer, A. Pastuszyn, D. M. Lawrence, and J. A. Fee, "Molecular genetic and protein chemical characterization of the cytochrome ba_3 from *Thermus thermophilus* HB8," *J. Biol. Chem.*, vol. 270, pp. 20345–20358, 1995.

[21] M. R. Noor and T. Soulimane, "Bioenergetics at extreme temperature: *Thermus thermophilus* ba_3- and caa_3-type cytochrome *c* oxidases," *Biochimica et Biophysica Acta - Bioenergetics*, vol. 1817, pp. 638–649, 4 2012.

[22] A. Razvi and J. M. Scholtz, "Lessons in stability from thermophilic proteins," *Protein Science*, vol. 15, pp. 1569–1578, 7 2006.

[23] M. J. Thompson and D. Eisenberg, "Transproteomic evidence of a loop-deletion mechanism for enhancing protein thermostability," *Journal of Molecular Biology*, vol. 290, pp. 595–604, 7 1999.

[24] M. Lübben and K. Morand, "Novel prenylated hemes as cofactors of cytochrome oxidases. Archaea have modified hemes A and O.," *The Journal of biological chemistry*, vol. 269, pp. 21473–9, 8 1994.

[25] G. Schafer, M. Engelhard, and V. Muller, "Bioenergetics of the Archaea," *Microbiology and Molecular Biology Reviews*, vol. 63, pp. 570–620, 9 1999.

[26] O. Maneg, B. Ludwig, and F. Malatesta, "Different Interaction Modes of Two Cytochrome-c Oxidase Soluble CU A Fragments with Their Substrates," *Journal of Biological Chemistry*, vol. 278, pp. 46734–46740, 11 2003.

[27] Y. Chen, L. Hunsicker-Wang, R. L. Pacoma, E. Luna, and J. A. Fee, "A homologous expression system for obtaining engineered cytochrome ba_3 from *Thermus thermophilus* HB8," *Protein Expression and Purification*, vol. 40, pp. 299–318, 2005.

[28] A. A. Stuchebrukhov, "Long-distance electron tunneling in proteins: A new challenge for time-resolved spectroscopy," *Laser Physics*, vol. 20, pp. 125–138, 1 2010.

[29] M. Wikström, K. Krab, and V. Sharma, "Oxygen Activation and Energy Conservation by Cytochrome *c* Oxidase," *Chemical Reviews*, vol. 118, pp. 2469–2490, 3 2018.

[30] G. Brändén, M. Brändén, B. Schmidt, D. A. Mills, S. Ferguson-Miller, and P. Brzezinski, "The protonation state of a heme propionate controls electron transfer in cytochrome *c* oxidase," *Biochemistry*, vol. 44, pp. 10466–10474, 8 2005.

[31] M. Wikström, R. B. Gennis, and P. R. Rich, "Structures of the intermediates in the catalytic cycle of mitochondrial cytochrome c oxidase," *Biochimica et Biophysica Acta (BBA) - Bioenergetics*, vol. 1864, p. 148933, 4 2023.

[32] O. M. H. Richter and B. Ludwig, "Electron transfer and energy transduction in the terminal part of the respiratory chain - Lessons from bacterial model systems," *Biochimica et Biophysica Acta - Bioenergetics*, vol. 1787, pp. 626–634, 6 2009.

[33] S. Yoshikawa and A. Shimada, "Reaction Mechanism of Cytochrome *c* Oxidase," *Chemical Reviews*, vol. 115, pp. 1936–1989, 2 2015.

[34] J. E. Morgan, M. I. Verkhovsky, and M. Wikström, "Observation and Assignment of Peroxy and Ferryl Intermediates in the Reduction of Dioxygen to Water by Cytochrome *c* Oxidase," *Biochemistry*, vol. 35, pp. 12235–12240, 1 1996.

[35] A. Sucheta, K. E. Georgiadis, and Ólöf Einarsdóttir, "Mechanism of cytochrome *c* oxidase-catalyzed reduction of dioxygen to water: Evidence for peroxy and ferryl intermediates at room temperature," *Biochemistry*, vol. 36, pp. 554–565, 1 1997.

[36] M. Fabian, D. Jancura, and G. Palmer, "Two Sites of Interaction of Anions with Cytochrome *a* in Oxidized Bovine Cytochrome *c* Oxidase," *Journal of Biological Chemistry*, vol. 279, pp. 16170–16177, 4 2004.

[37] T. Ogura and T. Kitagawa, "Resonance Raman characterization of the P intermediate in the reaction of bovine cytochrome *c* oxidase," *Biochimica et Biophysica Acta (BBA) - Bioenergetics*, vol. 1655, pp. 290–297, 4 2004.

[38] G. Brändén, R. B. Gennis, and P. Brzezinski, "Transmembrane proton translocation by cytochrome *c* oxidase," *Biochimica et Biophysica Acta (BBA) - Bioenergetics*, vol. 1757, pp. 1052–1063, 8 2006.

[39] R. B. Gennis, "How does cytochrome oxidase pump protons?," *Proceedings of the National Academy of Sciences*, vol. 95, pp. 12747–12749, 10 1998.

[40] F. MacMillan, A. Kannt, J. Behr, T. Prisner, and H. Michel, "Direct Evidence for a Tyrosine Radical in the Reaction of Cytochrome *c* Oxidase with Hydrogen Peroxide," *Biochemistry*, vol. 38, pp. 9179–9184, 7 1999.

[41] G. T. Babcock, "How oxygen is activated and reduced in respiration," *Proceedings of the National Academy of Sciences*, vol. 96, pp. 12971–12973, 11 1999.

[42] M. Brunori, A. Colosimo, M. T. Wilson, P. Sarti, and E. Antonini, "Interconversion between states in cytochrome oxidase: Interpretation of kinetic data on mixed-valence oxidase," *FEBS Letters*, vol. 152, pp. 75–78, 2 1983.

[43] D. Bloch, I. Belevich, A. Jasaitis, C. Ribacka, A. Puustinen, M. I. Verkhovsky, and M. Wikström, "The catalytic cycle of cytochrome *c* oxidase is not the sum of its two halves," *Proceedings of the National Academy of Sciences*, vol. 101, pp. 529–533, 1 2004.

[44] P. Brzezinski, "Redox-driven membrane-bound proton pumps," *Trends in Biochemical Sciences*, vol. 29, pp. 380–387, 7 2004.

[45] D. A. Mills and S. Ferguson-Miller, "Understanding the mechanism of proton movement linked to oxygen reduction in cytochrome *c* oxidase: lessons from other proteins," *FEBS Letters*, vol. 545, pp. 47–51, 6 2003.

[46] U. Pfitzner, A. Odenwald, T. Ostermann, L. Weingard, B. Ludwig, and O.-M. H. Richter, "Cytochrome *c* oxidase (heme aa_3) from *Paracoccus denitrificans*: analysis of mutations in putative proton channels of subunit i," *Journal of Bioenergetics and Biomembranes*, vol. 30, pp. 89–97, 1998.

[47] A. Kannt, T. Soulimane, G. Buse, A. Becker, E. Bamberg, and H. Michel, "Electrical current generation and proton pumping catalyzed by the ba_3-type cytochrome *c* oxidase from *Thermus thermophilus*," *FEBS Letters*, vol. 434, pp. 17–22, 8 1998.

[48] M. Wikström, K. Krab, and V. Sharma, "Oxygen activation and energy conservation by cytochrome *c* oxidase," *Chemical Reviews*, vol. 118, pp. 2469–2490, 3 2018.

[49] E. Antonini, M. Brunori, C. Greenwood, and B. G. Malmström, "Catalytic Mechanism of Cytochrome Oxidase," *Nature*, vol. 228, pp. 936–937, 12 1970.

[50] G. M. Baker, M. Noguchi, and G. Palmer, "The reaction of cytochrome oxidase with cyanide. Preparation of the rapidly reacting form and its conversion to the slowly reacting form.," *Journal of Biological Chemistry*, vol. 262, pp. 595–604, 1 1987.

[51] M. T. Wilson, C. Greenwood, M. Brunori, and E. Antonini, "Kinetic studies on the reaction between cytochrome *c* oxidase and ferrocytochrome c," *Biochemical Journal*, vol. 147, pp. 145–153, 4 1975.

[52] A. S. F. Oliveira, J. M. Damas, A. M. Baptista, and C. M. Soares, "Exploring O_2 Diffusion in A-Type Cytochrome *c* Oxidases: Molecular Dynamics Simulations Uncover Two Alternative Channels towards the Binuclear Site," *PLoS Computational Biology*, vol. 10, p. e1004010, 12 2014.

[53] S. A. Seibold, D. A. Mills, S. Ferguson-Miller, and R. I. Cukier, "Water Chain Formation and Possible Proton Pumping Routes in *Rhodobacter sphaeroides* Cytochrome *c* Oxidase: A Molecular Dynamics Comparison of the Wild Type and R481K Mutant," *Biochemistry*, vol. 44, pp. 10475–10485, 8 2005.

[54] V. M. Luna, Y. Chen, J. A. Fee, and C. D. Stout, "Crystallographic studies of Xe and Kr binding within the large internal cavity of cytochrome *ba*$_3$ from *Thermus thermophilus*: Structural analysis and role of oxygen transport channels in the heme-Cu oxidases," *Biochemistry*, vol. 47, pp. 4657–4665, 4 2008.

[55] W. McDonald, C. Funatogawa, Y. Li, I. Szundi, Y. Chen, J. A. Fee, C. D. Stout, and Ólöf Einarsdóttir, "Ligand Access to the Active Site in *Thermus thermophilus ba*$_3$ and Bovine Heart *aa*$_3$ Cytochrome Oxidases," *Biochemistry*, vol. 52, pp. 640–652, 1 2013.

[56] C. Funatogawa, Y. Li, Y. Chen, W. McDonald, I. Szundi, J. A. Fee, C. D. Stout, and Ólöf Einarsdóttir, "Role of the Conserved Valine 236 in Access of Ligands to the Active Site of *Thermus thermophilus ba*$_3$ Cytochrome Oxidase," *Biochemistry*, vol. 56, pp. 107–119, 1 2017.

[57] D. Sutton, "A textbook of radiology and imaging," 1987.

[58] H. N. Chapman, P. Fromme, A. Barty, T. A. White, R. A. Kirian, A. Aquila, M. S. Hunter, J. Schulz, D. P. DePonte, U. Weierstall, *et al.*, "Femtosecond X-ray protein nanocrystallography," *Nature*, vol. 470, no. 7332, pp. 73–77, 2011.

[59] J. Agirre, M. Atanasova, H. Bagdonas, C. B. Ballard, A. Baslé, J. Beilsten-Edmands, R. J. Borges, D. G. Brown, J. J. Burgos-Mármol, J. M. Berrisford, P. S. Bond, I. Caballero, L. Catapano, G. Chojnowski, A. G. Cook, K. D. Cowtan, T. I. Croll, J. Debreczeni, N. E. Devenish, E. J. Dodson, T. R. Drevon, P. Emsley, G. Evans, P. R. Evans, M. Fando, J. Foadi, L. Fuentes-Montero, E. F. Garman, M. Gerstel, R. J. Gildea, K. Hatti, M. L. Hekkelman, P. Heuser, S. W. Hoh, M. A. Hough, H. T. Jenkins, E. Jiménez, R. P. Joosten, R. M. Keegan, N. Keep, E. B. Krissinel, P. Kolenko, O. Kovalevskiy, V. S. Lamzin, D. M. Lawson, A. A. Lebedev, A. G. W. Leslie, B. Lohkamp, F. Long, M. Malý, A. J. McCoy, S. J. McNicholas, A. Medina, C. Millán, J. W. Murray, G. N. Murshudov, R. A. Nicholls, M. E. M. Noble, R. Oeffner, N. S. Pannu, J. M. Parkhurst, N. Pearce, J. Pereira, A. Perrakis, H. R. Powell, R. J. Read, D. J. Rigden, W. Rochira, M. Sammito, F. S. Rodríguez, G. M. Sheldrick, K. L. Shelley, F. Simkovic, A. J. Simpkin, P. Skubak, E. Sobolev, R. A. Steiner, K. Stevenson, I. Tews, J. M. H. Thomas, A. Thorn, J. T. Valls, V. Uski, I. Usón, A. Vagin, S. Velankar, M. Vollmar, H. Walden, D. Waterman, K. S. Wilson, M. D. Winn, G. Winter, M. Wojdyr, and K. Yamashita, "The CCP 4 suite: integrative software for macromolecular crystallography," *Acta Crystallographica Section D Structural Biology*, vol. 79, pp. 449–461, 6 2023.

[60] S. M. Adam, G. B. Wijeratne, P. J. Rogler, D. E. Diaz, D. A. Quist, J. J. Liu, and K. D. Karlin, "Synthetic Fe/Cu Complexes: Toward Understanding Heme-Copper Oxidase Structure and Function," *Chemical Reviews*, vol. 118, pp. 10840–11022, 11 2018.

[61] D. DePonte, U. Weierstall, K. Schmidt, J. Warner, D. Starodub, J. Spence, and R. Doak, "Gas dynamic virtual nozzle for generation of microscopic droplet streams," *Journal of Physics D: Applied Physics*, vol. 41, no. 19, p. 195505, 2008.

[62] S. Botha, K. Nass, T. R. Barends, W. Kabsch, B. Latz, F. Dworkowski, L. Foucar, E. Panepucci, M. Wang, R. L. Shoeman, *et al.*, "Room-temperature serial crystallography at synchrotron X-ray sources using slowly flowing free-standing high-viscosity microstreams," *Acta Crystallographica Section D: Biological Crystallography*, vol. 71, no. 2, pp. 387–397, 2015.

[63] U. Weierstall, D. James, C. Wang, T. A. White, D. Wang, W. Liu, J. C. H. Spence, R. B. Doak, G. Nelson, P. Fromme, R. Fromme, I. Grotjohann, C. Kupitz, N. A. Zatsepin, H. Liu, S. Basu, D. Wacker, G. W. Han, V. Katritch, S. Boutet, M. Messerschmidt, G. J. Williams, J. E. Koglin, M. M. Seibert, M. Klinker, C. Gati, R. L. Shoeman, A. Barty, H. N. Chapman, R. A. Kirian, K. R. Beyerlein, R. C. Stevens, D. Li, S. T. A. Shah, N. Howe, M. Caffrey, and V. Cherezov, "Lipidic cubic phase injector facilitates membrane protein serial femtosecond crystallography," *Nature Communications*, vol. 5, p. 3309, 2 2014.

[64] A. Barty, R. A. Kirian, F. R. N. C. Maia, M. Hantke, C. H. Yoon, T. A. White, and H. Chapman, "*Cheetah*: software for high-throughput reduction and analysis of serial femtosecond X-ray diffraction data," *Journal of Applied Crystallography*, vol. 47, pp. 1118–1131, Jun 2014.

[65] T. A. White, "Processing serial crystallography data with *CrystFEL*: a step-by-step guide," *Acta Crystallographica Section D*, vol. 75, pp. 219–233, Feb 2019.

[66] A. G. W. Leslie and H. R. Powell, "Processing diffraction data with *mosflm*," in *Evolving Methods for Macromolecular Crystallography* (R. J. Read and J. L. Sussman, eds.), (Dordrecht), pp. 41–51, Springer Netherlands, 2007.

[67] A. J. M. Duisenberg, "Indexing in single-crystal diffractometry with an obstinate list of reflections," *Journal of Applied Crystallography*, vol. 25, pp. 92–96, Apr 1992.

[68] W. Kabsch, "*XDS*," *Acta Crystallographica Section D Biological Crystallography*, vol. 66, pp. 125–132, 2 2010.

[69] Y. Gevorkov, O. Yefanov, A. Barty, T. A. White, V. Mariani, W. Brehm, A. Tolstikova, R.-R. Grigat, and H. N. Chapman, "*XGANDALF* – extended gradient descent algorithm for lattice finding," *Acta Crystallographica Section A Foundations and Advances*, vol. 75, pp. 694–704, 9 2019.

[70] G. Brändén and R. Neutze, "Advances and challenges in time-resolved macromolecular crystallography," *Science*, vol. 373, 8 2021.

[71] K. Moffat, D. Szebenyi, and D. Bilderback, "X-ray Laue Diffraction from Protein Crystals," *Science*, vol. 223, pp. 1423–1425, 3 1984.

[72] A. Aquila, M. S. Hunter, R. B. Doak, R. A. Kirian, P. Fromme, T. A. White, J. Andreasson, D. Arnlund, S. Bajt, T. R. M. Barends, M. Barthelmess, M. J. Bogan, C. Bostedt, H. Bottin, J. D. Bozek, C. Caleman, N. Coppola, J. Davidsson, D. P. DePonte, V. Elser, S. W. Epp, B. Erk, H. Fleckenstein, L. Foucar, M. Frank, R. Fromme, H. Graafsma, I. Grotjohann, L. Gumprecht, J. Hajdu, C. Y. Hampton, A. Hartmann, R. Hartmann, S. Hau-Riege, G. Hauser, H. Hirsemann, P. Holl, J. M. Holton, A. Hömke, L. Johansson, N. Kimmel, S. Kassemeyer, F. Krasniqi, K.-U. Kühnel, M. Liang, L. Lomb, E. Malmerberg, S. Marchesini, A. V. Martin, F. R. Maia, M. Messerschmidt, K. Nass, C. Reich, R. Neutze, D. Rolles, B. Rudek, A. Rudenko, I. Schlichting, C. Schmidt, K. E. Schmidt, J. Schulz, M. M. Seibert, R. L. Shoeman, R. Sierra, H. Soltau, D. Starodub, F. Stellato, S. Stern, L. Strüder, N. Timneanu, J. Ullrich, X. Wang, G. J. Williams, G. Weidenspointner, U. Weierstall, C. Wunderer, A. Barty, J. C. H. Spence, and H. N. Chapman, "Time-resolved protein nanocrystallography using an X-ray free-electron laser," *Optics Express*, vol. 20, p. 2706, 1 2012.

[73] J. Tenboer, S. Basu, N. Zatsepin, K. Pande, D. Milathianaki, M. Frank, M. Hunter, S. Boutet, G. J. Williams, J. E. Koglin, D. Oberthuer, M. Heymann, C. Kupitz, C. Conrad, J. Coe, S. Roy-Chowdhury, U. Weierstall, D. James, D. Wang, T. Grant, A. Barty, O. Yefanov, J. Scales, C. Gati, C. Seuring, V. Srajer, R. Henning, P. Schwander, R. Fromme, A. Ourmazd, K. Moffat, J. J. V. Thor, J. C. H. Spence, P. Fromme, H. N. Chapman, and M. Schmidt, "Time-resolved serial crystallography captures high-resolution intermediates of photoactive yellow protein," *Science*, vol. 346, pp. 1242–1246, 12 2014.

[74] J. Woodhouse, G. N. Kovacs, N. Coquelle, L. M. Uriarte, V. Adam, T. R. M. Barends, M. Byrdin, E. de la Mora, R. B. Doak, M. Feliks, M. Field, F. Fieschi, V. Guillon, S. Jakobs, Y. Joti, P. Macheboeuf, K. Motomura, K. Nass, S. Owada, C. M. Roome, C. Ruckebusch, G. Schirò, R. L. Shoeman, M. Thepaut, T. Togashi, K. Tono, M. Yabashi, M. Cammarata, L. Foucar, D. Bourgeois, M. Sliwa, J.-P. Colletier, I. Schlichting, and M. Weik, "Photoswitching mechanism of a fluorescent protein revealed by time-resolved crystallography and transient absorption spectroscopy," *Nature Communications*, vol. 11, p. 741, 2 2020.

[75] E. Claesson, W. Y. Wahlgren, H. Takala, S. Pandey, L. Castillon, V. Kuznetsova, L. Henry, M. Panman, M. Carrillo, J. Kübel, R. Nanekar, L. Isaksson, A. Nimmrich, A. Cellini, D. Morozov, M. Maj, M. Kurttila, R. Bosman, E. Nango, R. Tanaka, T. Tanaka, L. Fangjia, S. Iwata, S. Owada, K. Moffat, G. Groenhof, E. A. Stojković, J. A. Ihalainen, M. Schmidt, and S. Westenhoff, "The primary structural photoresponse of phytochrome proteins captured by a femtosecond X-ray laser," *eLife*, vol. 9, p. e53514, mar 2020.

[76] T. Alber, G. A. Petsko, and D. Tsernoglou, "Crystal structure of elastase–substrate complex at 55 °C," *Nature*, vol. 263, pp. 297–300, 9 1976.

[77] J. Hajdu, K. Acharya, D. Stuart, P. McLaughlin, D. Barford, N. Oikonomakos, H. Klein, and L. Johnson, "Catalysis in the crystal: synchrotron radiation studies with glycogen phosphorylase b.," *The EMBO Journal*, vol. 6, pp. 539–546, 2 1987.

[78] M. M. Lerch, M. J. Hansen, G. M. vanDam, W. Szymanski, and B. L. Feringa, "Emerging Targets in Photopharmacology," *Angewandte Chemie International Edition*, vol. 55, no. 37, pp. 10978–10999, 2016.

[79] D. A. Keedy, L. R. Kenner, M. Warkentin, R. A. Woldeyes, J. B. Hopkins, M. C. Thompson, A. S. Brewster, A. H. Van Benschoten, E. L. Baxter, M. Uervirojnangkoorn, *et al.*, "Mapping the conformational landscape of a dynamic enzyme by multitemperature and XFEL crystallography," *Elife*, vol. 4, p. e07574, 2015.

[80] D. R. Hekstra, K. I. White, M. A. Socolich, R. W. Henning, V. Šrajer, and R. Ranganathan, "Electric-field-stimulated protein mechanics," *Nature*, vol. 540, no. 7633, pp. 400–405, 2016.

[81] D. Liebschner, P. V. Afonine, M. L. Baker, G. Bunkóczi, V. B. Chen, T. I. Croll, B. Hintze, L.-W. Hung, S. Jain, A. J. McCoy, N. W. Moriarty, R. D. Oeffner, B. K. Poon, M. G. Prisant, R. J. Read, J. S. Richardson, D. C. Richardson, M. D. Sammito, O. V. Sobolev, D. H. Stockwell, T. C. Terwilliger, A. G. Urzhumtsev, L. L. Videau, C. J. Williams, and P. D. Adams, "Macromolecular structure determination using X-rays, neutrons and electrons: recent developments in *Phenix*," *Acta Crystallographica Section D*, vol. 75, pp. 861–877, Oct 2019.

[82] E. D. Zitter, N. Coquelle, P. Oeser, T. R. Barends, and J. P. Colletier, "Xtrapol8 enables automatic elucidation of low-occupancy intermediate-states in crystallographic studies," *Communications Biology*, vol. 5, 12 2022.

[83] A. R. Pearson and P. Mehrabi, "Serial synchrotron crystallography for time-resolved structural biology," *Current Opinion in Structural Biology*, vol. 65, pp. 168–174, 12 2020.

[84] V. Šrajer, T. yi Teng, T. Ursby, C. Pradervand, Z. Ren, S. ichi Adachi, W. Schildkamp, D. Bourgeois, M. Wulff, and K. Moffat, "Photolysis of the Carbon Monoxide Complex of Myoglobin: Nanosecond Time-Resolved Crystallography," *Science*, vol. 274, pp. 1726–1729, 12 1996.

[85] T. Weinert, N. Olieric, R. Cheng, S. Brünle, D. James, D. Ozerov, D. Gashi, L. Vera, M. Marsh, K. Jaeger, F. Dworkowski, E. Panepucci, S. Basu, P. Skopintsev, A. S. Doré, T. Geng, R. M. Cooke, M. Liang, A. E. Prota, V. Panneels, P. Nogly, U. Ermler, G. Schertler, M. Hennig, M. O. Steinmetz, M. Wang, and J. Standfuss, "Serial millisecond crystallography for routine room-temperature structure determination at synchrotrons," *Nature Communications*, vol. 8, p. 542, 9 2017.

[86] F. Stellato, D. Oberthür, M. Liang, R. Bean, C. Gati, O. Yefanov, A. Barty, A. Burkhardt, P. Fischer, L. Galli, R. A. Kirian, J. Meyer, S. Panneerselvam, C. H. Yoon, F. Chervinskii, E. Speller, T. A. White, C. Betzel, A. Meents, and H. N. Chapman, "Room-temperature macromolecular serial crystallography using synchrotron radiation," *IUCrJ*, vol. 1, pp. 204–212, 7 2014.

[87] S. Ghosh, D. Zorić, P. Dahl, M. Bjelčić, J. Johannesson, E. Sandelin, P. Borjesson, A. Björling, A. Banacore, P. Edlund, O. Aurelius, M. Milas, J. Nan, A. Shilova, A. Gonzalez, U. Mueller, G. Brändén, and R. Neutze, "A simple goniometer-compatible flow cell for serial synchrotron X-ray crystallography," *Journal of Applied Crystallography*, vol. 56, pp. 449–460, 4 2023.

[88] K. A. Zielinski, A. Prester, H. Andaleeb, S. Bui, O. Yefanov, L. Catapano, A. Henkel, M. O. Wiedorn, O. Lorbeer, E. Crosas, J. Meyer, V. Mariani, M. Domaracky, T. A. White, H. Fleckenstein, I. Sarrou, N. Werner, C. Betzel, H. Rohde, M. Aepfelbacher, H. N. Chapman, M. Perbandt, R. A. Steiner, and D. Oberthuer, "Rapid and efficient room-temperature serial synchrotron crystallography using the CFEL TapeDrive," *IUCrJ*, vol. 9, pp. 778–791, 11 2022.

[89] A. Henkel, M. Galchenkova, J. Maracke, O. Yefanov, B. Klopprogge, J. Hakanpää, J. R. Mesters, H. N. Chapman, and D. Oberthuer, "JINXED: just in time crystallization for easy structure determination of biological macromolecules," *IUCrJ*, vol. 10, pp. 253–260, May 2023.

[90] E. de la Mora, N. Coquelle, C. S. Bury, M. Rosenthal, J. M. Holton, I. Carmichael, E. F. Garman, M. Burghammer, J.-P. Colletier, and M. Weik, "Radiation damage and dose limits in serial synchrotron crystallography at cryo- and room temperatures," *Proceedings of the National Academy of Sciences*, vol. 117, pp. 4142–4151, 2 2020.

[91] J. Yano, J. Kern, K. Irrgang, M. Latimer, U. Bergmann, P. Glatzel, Y. Pushkar, J. Biesiadka, B. Loll, K. Sauer, *et al.*, "X-ray damage to the Mn 4 Ca complex in photosystem II crystals: a case study for metallo-protein X-ray crystallography," *Proc. Natl Acad. Sci. USA*, vol. 102, no. 12, pp. 047–12, 2005.

[92] M. C. Corbett, M. J. Latimer, T. L. Poulos, I. F. Sevrioukova, K. O. Hodgson, and B. Hedman, "Photoreduction of the active site of the metalloprotein putidaredoxin by synchrotron radiation," *Acta Crystallographica Section D: Biological Crystallography*, vol. 63, no. 9, pp. 951–960, 2007.

[93] J. Jaklevic, J. Kirby, M. Klein, A. Robertson, G. Brown, and P. Eisenberger, "Fluorescence detection of EXAFS: Sensitivity enhancement for dilute species and thin films," *Solid State Communications*, vol. 23, no. 9, pp. 679–682, 1977.

[94] R. Sarangi, "X-ray absorption near-edge spectroscopy in bioinorganic chemistry: Application to M–O_2 systems," *Coordination Chemistry Reviews*, vol. 257, pp. 459–472, 1 2013.

[95] J. J. Rehr, J. J. Kas, M. P. Prange, A. P. Sorini, Y. Takimoto, and F. Vila, "Ab initio theory and calculations of X-ray spectra," *Comptes Rendus Physique*, vol. 10, pp. 548–559, 7 2009.

[96] M. Benfatto, S. D. Longa, E. Pace, G. Chillemi, C. Padrin, C. R. Natoli, and N. Sanna, "MXAN: A new program for ab-initio structural quantitative analysis of XANES experiments," *Computer Physics Communications*, vol. 265, p. 107992, 8 2021.

[97] F. Neese, "The ORCA program system," *WIREs Computational Molecular Science*, vol. 2, pp. 73–78, 1 2012.

[98] W. Lambrecht and O. Andersen, "Tight-binding muffin-tin orbital Green's function method for surface and interface electronic structure calculations," *Surface Science*, vol. 178, pp. 256–263, 12 1986.

[99] S. J. Gurman, N. Binsted, and I. Ross, "A rapid, exact, curved-wave theory for EXAFS calculations. II. The multiple-scattering contributions," *Journal of Physics C: Solid State Physics*, vol. 19, pp. 1845–1861, 4 1986.

[100] A. Filipponi, A. D. Cicco, and C. R. Natoli, "X-ray-absorption spectroscopy and n -body distribution functions in condensed matter. I. Theory," *Physical Review B*, vol. 52, pp. 15122–15134, 12 1995.

[101] I. R. Krauss, A. Merlino, A. Vergara, and F. Sica, "An Overview of Biological Macromolecule Crystallization," *International Journal of Molecular Sciences*, vol. 14, pp. 11643–11691, 5 2013.

[102] M. Caffrey and V. Cherezov, "Crystallizing membrane proteins using lipidic mesophases.," *Nat Protoc*, vol. 4, 2009.

[103] E. Landau and J. Rosenbusch, "Lipidic cubic phases: a novel concept for the crystallization of membrane proteins.," *Proc Natl Acad Sci U S A*, vol. 93, 1996.

[104] S. G. F. Rasmussen, H.-J. Choi, J. J. Fung, E. Pardon, P. Casarosa, P. S. Chae, B. T. DeVree, D. M. Rosenbaum, F. S. Thian, T. S. Kobilka, A. Schnapp, I. Konetzki, R. K. Sunahara, S. H. Gellman, A. Pautsch, J. Steyaert, W. I. Weis, and B. K. Kobilka, "Structure of a nanobody-stabilized active state of the $\beta 2$ adrenoceptor," *Nature*, vol. 469, pp. 175–180, 1 2011.

[105] H. E. Kato, F. Zhang, O. Yizhar, C. Ramakrishnan, T. Nishizawa, K. Hirata, J. Ito, Y. Aita, T. Tsukazaki, S. Hayashi, P. Hegemann, A. D. Maturana, R. Ishitani, K. Deisseroth, and O. Nureki, "Crystal structure of the channelrhodopsin light-gated cation channel," *Nature*, vol. 482, pp. 369–374, 2 2012.

[106] A. Cheng, B. Hummel, H. Qiu, and M. Caffrey, "A simple mechanical mixer for small viscous lipid-containing samples.," *Chem Phys Lipids*, vol. 95, 1998.

[107] H. Qiu and M. Caffrey, "The phase diagram of the monoolein/water system: metastability and equilibrium aspects," *Biomaterials*, vol. 21, pp. 223–234, 2 2000.

[108] Y. Misquitta and M. Caffrey, "Detergents Destabilize the Cubic Phase of Monoolein: Implications for Membrane Protein Crystallization," *Biophysical Journal*, vol. 85, pp. 3084–3096, 11 2003.

[109] A. B. Wöhri, L. C. Johansson, P. Wadsten-Hindrichsen, W. Y. Wahlgren, G. Fischer, R. Horsefield, G. Katona, M. Nyblom, F. Öberg, G. Young, R. J. Cogdell, N. J. Fraser, S. Engström, and R. Neutze, "A Lipidic-Sponge Phase Screen for Membrane Protein Crystallization," *Structure*, vol. 16, pp. 1003–1009, 7 2008.

[110] I. Ishigami, N. A. Zatsepin, M. Hikita, C. E. Conrad, G. Nelson, J. D. Coe, S. Basu, T. D. Grant, M. H. Seaberg, R. G. Sierra, M. S. Hunter, P. Fromme, R. Fromme, S.-R. Yeh, and D. L. Rousseau, "Crystal structure of CO-bound cytochrome *c* oxidase determined by serial femtosecond X-ray crystallography at room temperature," *Proceedings of the National Academy of Sciences*, vol. 114, pp. 8011–8016, 7 2017.

[111] M. Kubo, E. Nango, K. Tono, T. Kimura, S. Owada, C. Song, F. Mafuné, K. Miyajima, Y. Takeda, J.-y. Kohno, N. Miyauchi, T. Nakane, T. Tanaka, T. Nomura, J. Davidsson, R. Tanaka, M. Murata, T. Kameshima, T. Hatsui, Y. Joti, R. Neutze, M. Yabashi, and S. Iwata, "Nanosecond pump–probe device for time-resolved serial femtosecond crystallography developed at SACLA," *Journal of Synchrotron Radiation*, vol. 24, pp. 1086–1091, Sep 2017.

[112] I. Ishigami, A. Lewis-Ballester, A. Echelmeier, G. Brehm, N. A. Zatsepin, T. D. Grant, J. D. Coe, S. Lisova, G. Nelson, S. Zhang, Z. F. Dobson, S. Boutet, R. G. Sierra, A. Batyuk, P. Fromme, R. Fromme, J. C. H. Spence, A. Ros, S.-R. Yeh, and D. L. Rousseau, "Snapshot of an oxygen intermediate in the catalytic reaction of cytochrome *c* oxidase," *Proceedings of the National Academy of Sciences*, vol. 116, pp. 3572–3577, 2 2019.

[113] R. Andersson, C. Safari, R. Dods, E. Nango, R. Tanaka, A. Yamashita, T. Nakane, K. Tono, Y. Joti, P. Båth, E. Dunevall, R. Bosman, O. Nureki, S. Iwata, R. Neutze, and G. Brändén, "Serial femtosecond crystallography structure of cytochrome *c* oxidase at room temperature," *Scientific Reports*, vol. 7, 12 2017.

[114] J. L. Dickerson, P. T. N. McCubbin, and E. F. Garman, "RADDOSE-XFEL : femtosecond time-resolved dose estimates for macromolecular X-ray free-electron laser experiments," *Journal of Applied Crystallography*, vol. 53, pp. 549–560, 4 2020.

[115] E. Nango, A. Royant, M. Kubo, T. Nakane, C. Wickstrand, T. Kimura, T. Tanaka, K. Tono, C. Song, R. Tanaka, T. Arima, A. Yamashita, J. Kobayashi, T. Hosaka, E. Mizohata, P. Nogly, M. Sugahara, D. Nam, T. Nomura, T. Shimamura, D. Im, T. Fujiwara, Y. Yamanaka, B. Jeon, T. Nishizawa, K. Oda, M. Fukuda, R. Andersson, P. Båth, R. Dods, J. Davidsson,

S. Matsuoka, S. Kawatake, M. Murata, O. Nureki, S. Owada, T. Kameshima, T. Hatsui, Y. Joti, G. Schertler, M. Yabashi, A.-N. Bondar, J. Standfuss, R. Neutze, and S. Iwata, "A three-dimensional movie of structural changes in bacteriorhodopsin," *Science*, vol. 354, pp. 1552–1557, 12 2016.

[116] A. Shimada, M. Kubo, S. Baba, K. Yamashita, K. Hirata, G. Ueno, T. Nomura, T. Kimura, K. Shinzawa-Itoh, J. Baba, K. Hatano, Y. Eto, A. Miyamoto, H. Murakami, T. Kumasaka, S. Owada, K. Tono, M. Yabashi, Y. Yamaguchi, S. Yanagisawa, M. Sakaguchi, T. Ogura, R. Komiya, J. Yan, E. Yamashita, M. Yamamoto, H. Ago, S. Yoshikawa, and T. Tsukihara, "A nanosecond time-resolved XFEL analysis of structural changes associated with CO release from cytochrome *c* oxidase," *Science Advances*, vol. 3, 7 2017.

[117] R. Andersson, C. Safari, P. Båth, R. Bosman, A. Shilova, P. Dahl, S. Ghosh, A. Dunge, R. Kjeldsen-Jensen, J. Nan, R. L. Shoeman, M. Kloos, R. B. Doak, U. Mueller, R. Neutze, and G. Brändén, "Well-based crystallization of lipidic cubic phase microcrystals for serial X-ray crystallography experiments," *Acta Crystallographica Section D Structural Biology*, vol. 75, pp. 937–946, 10 2019.

[118] A. Urzhumtsev, P. V. Afonine, and P. D. Adams, "TLS from fundamentals to practice," *Crystallography Reviews*, vol. 19, pp. 230–270, 10 2013.

[119] P. Emsley and K. Cowtan, "Coot : model-building tools for molecular graphics," *Acta Crystallographica Section D Biological Crystallography*, vol. 60, pp. 2126–2132, 12 2004.

[120] P. D. Adams, P. V. Afonine, G. Bunkóczi, V. B. Chen, I. W. Davis, N. Echols, J. J. Headd, L.-W. Hung, G. J. Kapral, R. W. Grosse-Kunstleve, A. J. McCoy, N. W. Moriarty, R. Oeffner, R. J. Read, D. C. Richardson, J. S. Richardson, T. C. Terwilliger, and P. H. Zwart, "PHENIX : a comprehensive Python-based system for macromolecular structure solution," *Acta Crystallographica Section D Biological Crystallography*, vol. 66, pp. 213–221, 2 2010.

[121] R. Dods, P. Båth, D. Morozov, V. A. Gagnér, D. Arnlund, H. L. Luk, J. Kübel, M. Maj, A. Vallejos, C. Wickstrand, R. Bosman, K. R. Beyerlein, G. Nelson, M. Liang, D. Milathianaki, J. Robinson, R. Harimoorthy, P. Berntsen, E. Malmerberg, L. Johansson, R. Andersson, S. Carbajo, E. Claesson, C. E. Conrad, P. Dahl, G. Hammarin, M. S. Hunter, C. Li, S. Lisova, A. Royant, C. Safari, A. Sharma, G. J. Williams, O. Yefanov, S. Westenhoff, J. Davidsson, D. P. DePonte, S. Boutet, A. Barty, G. Katona, G. Groenhof, G. Brändén, and R. Neutze, "Ultrafast structural changes within a photosynthetic reaction centre," *Nature*, vol. 589, pp. 310–314, 1 2021.

[122] M. L. Grünbein, A. Gorel, L. Foucar, S. Carbajo, W. Colocho, S. Gilevich, E. Hartmann, M. Hilpert, M. Hunter, M. Kloos, J. E. Koglin, T. J. Lane, J. Lewandowski, A. Lutman, K. Nass, G. N. Kovacs, C. M. Roome, J. Sheppard, R. L. Shoeman, M. Stricker, T. van Driel, S. Vetter, R. B. Doak, S. Boutet, A. Aquila, F. J. Decker, T. R. M. Barends, C. A. Stan, and I. Schlichting, "Effect of X-ray free-electron laser-induced shockwaves on haemoglobin microcrystals delivered in a liquid jet," *Nature Communications*, vol. 12, p. 1672, 3 2021.

[123] C. Wickstrand, R. Dods, A. Royant, and R. Neutze, "Bacteriorhodopsin: Would the real structural intermediates please stand up?," *Biochimica et Biophysica Acta (BBA) - General Subjects*, vol. 1850, pp. 536–553, 3 2015.

[124] A. Giuffrè, E. Forte, G. Antonini, E. D'Itri, M. Brunori, T. Soulimane, and G. Buse, "Kinetic Properties of ba_3 Oxidase from *Thermus thermophilus*: Effect of Temperature," *Biochemistry*, vol. 38, pp. 1057–1065, 1 1998.

[125] J. P. Osborne, N. J. Cosper, C. M. Stälhandske, R. A. Scott, J. O. Alben, and R. B. Gennis, "Cu XAS shows a change in the ligation of Cu(B) upon reduction of cytochrome bo_3 *from Escherichia coli*, volume = 38, year = 1999,," *Biochemistry*.

[126] E. Forte, M. C. Barone, M. Brunori, P. Sarti, and A. Giuffrè, "Redox-Linked Protonation of Cytochrome *c* Oxidase: The Effect of Chloride Bound to Cu B," *Biochemistry*, vol. 41, pp. 13046–13052, 10 2002.

[127] G. N. George, S. P. Cramer, T. G. Frey, and R. C. Prince, "X-ray absorption spectroscopy of oriented cytochrome oxidase," *Biochimica et Biophysica Acta (BBA) - Bioenergetics*, vol. 1142, pp. 240–252, 5 1993.

[128] I. Benesperi, R. Singh, and M. Freitag, "Copper Coordination Complexes for Energy-Relevant Applications," *Energies*, vol. 13, no. 9, 2020.

[129] N. J. Blackburn, R. W. Strange, J. Reedijk, A. Volbeda, A. Farooq, K. D. Karlin, and J. Zubieta, "X-ray absorption edge spectroscopy of copper(I) complexes. Coordination geometry of copper(I) in the reduced forms of copper proteins and their derivatives with carbon monoxide," *Inorganic Chemistry*, vol. 28, pp. 1349–1357, 4 1989.

[130] B. F. V. Gelder, W. H. Orme-Johnson, R. E. Hansen, and H. Beinert, "Electron paramagnetic resonance of heme at intermediate oxidation states of cytochrome *c* oxidase.," *Proceedings of the National Academy of Sciences*, vol. 58, pp. 1073–1079, 9 1967.

[131] B. Ravel and M. Newville, "*ATHENA*, *ARTEMIS*, *HEPHAESTUS*: data analysis for X-ray absorption spectroscopy using *IFEFFIT*," *Journal of Synchrotron Radiation*, vol. 12, pp. 537–541, Jul 2005.

[132] T. E. Westre, P. Kennepohl, J. G. DeWitt, B. Hedman, K. O. Hodgson, and E. I. Solomon, "A Multiplet Analysis of Fe K-Edge 1s → 3d Pre-Edge Features of Iron Complexes," *Journal of the American Chemical Society*, vol. 119, no. 27, pp. 6297–6314, 1997.

[133] L. S. Kau, D. J. Spira-Solomon, J. E. Penner-Hahn, K. O. Hodgson, and E. I. Solomon, "X-ray absorption edge determination of the oxidation state and coordination number of copper. Application to the type 3 site in *Rhus vernicifera* laccase and its reaction with oxygen," *Journal of the American Chemical Society*, vol. 109, no. 21, pp. 6433–6442, 1987.

[134] G. Kuppuraj, M. Dudev, and C. Lim, "Factors governing metal-ligand distances and coordination geometries of metal complexes," *The journal of physical chemistry B*, vol. 113, no. 9, pp. 2952–2960, 2009.

[135] R. W. Strange, N. J. Blackburn, P. F. Knowles, and S. S. Hasnain, "X-ray absorption spectroscopy of metal-histidine coordination in metalloproteins. Exact simulation of the EXAFS of tetrabis(imidazole)copper(II) nitrate and other copper-imidazole complexes by the use of a multiple-scattering treatment," *Journal of the American Chemical Society*, vol. 109, pp. 7157–7162, 11 1987.

[136] L. Noodleman, W.-G. H. Du, D. McRee, Y. Chen, T. Goh, and A. W. Götz, "Coupled transport of electrons and protons in a bacterial cytochrome *c* oxidase—dft calculated properties compared to structures and spectroscopies," *Physical Chemistry Chemical Physics*, vol. 22, pp. 26652–26668, 2020.

[137] G. Ueno, A. Shimada, E. Yamashita, K. Hasegawa, T. Kumasaka, K. Shinzawa-Itoh, S. Yoshikawa, T. Tsukihara, and M. Yamamoto, "Low-dose X-ray structure analysis of cytochrome *c* oxidase utilizing high-energy X-rays," *Journal of Synchrotron Radiation*, vol. 26, pp. 912–921, 7 2019.

[138] Y. C. Fann, I. Ahmed, N. J. Blackburn, J. S. Boswell, M. L. Verkhovskaya, B. M. Hoffman, and M. Wikstrom, "Structure of CuB in the Binuclear Heme-Copper Center of the Cytochrome aa_3-Type Quinol Oxidase from *Bacillus subtilis*: An ENDOR and EXAFS Study," *Biochemistry*, vol. 34, pp. 10245–10255, 8 1995.

[139] N. J. Blackburn, S. D. Vries, M. E. Barr, R. P. Houser, W. B. Tolman, D. Sanders, and J. A. Fee, "X-ray absorption studies on the mixed-valence and fully reduced forms of the soluble Cu(A) domains of cytochrome *c* oxidase," *J. Am. Chem. Soc.*, vol. 119, pp. 6135–6143, 1997.

[140] J. Yano, J. Robblee, Y. Pushkar, M. A. Marcus, J. Bendix, J. M. Workman, T. J. Collins, E. I. Solomon, S. D. George, and V. K. Yachandra, "Polarized X-ray Absorption Spectroscopy of Single-Crystal Mn(V) Complexes Relevant to the Oxygen-Evolving Complex of Photosystem II," *Journal of the American Chemical Society*, vol. 129, pp. 12989–13000, 10 2007.

[141] F. D. Fuller, S. Gul, R. Chatterjee, E. S. Burgie, I. D. Young, H. Lebrette, V. Srinivas, A. S. Brewster, T. Michels-Clark, J. A. Clinger, B. Andi, M. Ibrahim, E. Pastor, C. de Lichtenberg, R. Hussein, C. J. Pollock, M. Zhang, C. A. Stan, T. Kroll, T. Fransson, C. Weninger, M. Kubin, P. Aller, L. Lassalle, P. Bräuer, M. D. Miller, M. Amin, S. Koroidov, C. G. Roessler, M. Allaire, R. G. Sierra, P. T. Docker, J. M. Glownia, S. Nelson, J. E. Koglin, D. Zhu, M. Chollet, S. Song, H. Lemke, M. Liang, D. Sokaras, R. Alonso-Mori, A. Zouni, J. Messinger, U. Bergmann, A. K. Boal, J. M. Bollinger, C. Krebs, M. Högbom, G. N. Phillips, R. D. Vierstra, N. K. Sauter, A. M. Orville, J. Kern, V. K. Yachandra, and J. Yano, "Drop-on-demand sample delivery for studying biocatalysts in action at X-ray free-electron lasers," *Nature Methods*, vol. 14, pp. 443–449, 4 2017.

[142] J. Kern, R. Alonso-Mori, R. Tran, J. Hattne, R. J. Gildea, N. Echols, C. Glöckner, J. Hellmich, H. Laksmono, R. G. Sierra, B. Lassalle-Kaiser, S. Koroidov, A. Lampe, G. Han, S. Gul, D. DiFiore, D. Milathianaki, A. R. Fry, A. Miahnahri, D. W. Schafer, M. Messerschmidt, M. M. Seibert, J. E. Koglin, D. Sokaras, T.-C. Weng, J. Sellberg, M. J. Latimer, R. W. Grosse-Kunstleve, P. H. Zwart, W. E. White, P. Glatzel, P. D. Adams, M. J. Bogan, G. J. Williams, S. Boutet, J. Messinger, A. Zouni, N. K. Sauter, V. K. Yachandra, U. Bergmann, and J. Yano, "Simultaneous Femtosecond X-ray Spectroscopy and Diffraction of Photosystem II at Room Temperature," *Science*, vol. 340, pp. 491–495, 4 2013.